

Thèse de doctorat
Université d'Aix-Marseille

École doctorale: *Physique et Sciences de la Matière*
Spécialité : **Energie, Rayonnement et Plasma**

Modélisation des disruptions déclenchées par injection massive de gaz dans les plasmas de tokamaks

Presentée par:
Alexandre Fil

Thèse soutenue publiquement le 25 septembre 2015 devant le jury composé de :

Pr. Piero Martin	Rapporteur – Professeur à l'Université de Padoue
Dr. Hinrich Lutjens	Rapporteur – Chargé de recherche au CNRS, CPhT
Dr. Michael Lehnen	Examineur – Coordinateur Scientifique à ITER
Dr. Alain Becoulet	Examineur – Directeur de recherche à l'IRFM, CEA
Dr. Eric Nardon	Superviseur CEA – Ingénieur de recherche à l'IRFM, CEA
Pr. Peter Beyer	Directeur de thèse – Professeur à Aix-Marseille

Laboratoire d'accueil :

Institut de **R**echerche sur la **F**usion par confinement **M**agnétique
CEA – Cadarache
13108 Saint-Paul-lez-Durance, France

Sep 2012 – Sep 2015

PhD thesis
Aix-Marseille University

Graduate School: *Physics and Matter Sciences*

Speciality : **Energy, Radiation and Plasma**

**Modeling of massive gas
injection triggered disruptions
in tokamak plasmas**

Presented by:
Alexandre Fil

PhD defended on the 25th of september 2015 in front of the following committee:

Pr. Piero Martin	Reporter – Professor at Padova University
Dr. Hinrich Lutjens	Reporter – Research fellow at CNRS, CPhT
Dr. Michael Lehnen	Examiner – Scientific coordinator at ITER
Dr. Alain Becoulet	Examiner – Research director at IRFM, CEA
Dr. Eric Nardon	CEA supervisor – Research engineer at IRFM, CEA
Pr. Peter Beyer	PhD director – Professor at Aix-Marseille

Laboratory :
Institut de **R**echerche sur la **F**usion par confinement **M**agnétique
CEA – Cadarache
13108 Saint-Paul-lez-Durance, France

Sep 2012 – Sep 2015



Cette oeuvre est mise à disposition selon les termes de la [Licence Creative Commons Attribution - Pas d'Utilisation Commerciale - Pas de Modification 3.0 France](https://creativecommons.org/licenses/by-nc-nd/3.0/fr/).

Résumé

Les disruptions du plasma sont des phénomènes se produisant dans les tokamaks et qui entraînent une perte totale du confinement du plasma et la fin de la décharge. Ces disruptions sont des phénomènes rapides et violents et peuvent endommager les murs du tokamak ainsi que sa structure si elles ne sont pas contrôlées. Un système de mitigation des disruptions est donc indispensable pour ITER afin de réduire les forces électromagnétiques, mitiger les charges thermiques et éviter les électrons runaways générés par les disruptions du plasma. Remplir tous ces objectifs fait du design de ce système une tâche difficile, pour laquelle un apport conséquent de l'expérience et de la modélisation est nécessaire. Nous présentons dans cette thèse des résultats de modélisation sur l'amortissement des disruptions par injection massive de gaz, qui est une des méthodes principales envisagées sur ITER pour le système de mitigation. Premièrement, un modèle issu des premiers principes pour décrire le transport des neutres dans un plasma est donné et est appliqué à l'étude de l'interaction entre l'injection massive de gaz et le plasma. Les principaux mécanismes en jeu sont décrits et étudiés. L'échange de charge entre les neutres et les ions du plasma est isolée comme jouant un rôle majeur dans cette dynamique. Ensuite, le code 3D de Magnétohydrodynamique non linéaire JOREK est appliqué à l'étude des disruptions déclenchées par injection massive de gaz. Un intérêt particulier est porté sur la phase de quench thermique et les phénomènes MHD qui le déclenchent. Les résultats obtenus avec ce code sont comparés avec les expériences effectuées sur le tokamak JET. A étoffer (10 pages pour l'ED)

Mots clés : tokamak, fusion, disruption, injection massive de gaz, dynamique des fluides magnétisés

Abstract

Plasma disruptions are events occurring in tokamaks which result in the total loss of the plasma confinement and the end of the discharge. These disruptions are rapid and violent events and they can damage the tokamak walls and its structure if they are not controlled. A Disruption Mitigation System (DMS) is thus mandatory in ITER in order to reduce electromagnetic forces, mitigate heat loads and avoid Runaway Electrons (RE) generated by plasma disruptions. These combined objectives make the design of the DMS a complex and challenging task, for which substantial input from both experiments and modeling is needed. We present here modeling results on disruption mitigation by Massive Gas Injection (MGI), which is one of the main methods considered for the DMS of ITER. First, a model which stems from first principles is given for the transport of neutrals in a plasma and applied to the study of the interaction of the MGI with the plasma. Main mechanisms responsible for the penetration of the neutral gas are described and studied. Charge-exchange processes between the neutrals and the ions of the plasma is found to play a major role.

Then, the 3D non linear MHD code JOREK is applied to the study of MGI-triggered disruptions with a particular focus on the thermal quench phase and the MHD events which are responsible for it. The simulation results are compared to experiments done on the JET tokamak.

Keywords : tokamak, fusion, disruption, massive gas injection, magnetohydrodynamic

Acknowledgements

We thank G. Pautasso and E. Fable for useful suggestions. This work has been carried out within the framework of the EUROfusion Consortium. This work was granted access to the HPC resources of Aix-Marseille University financed by the project Equip@Meso (ANR-10-EQPX-29-01). A part of this work was carried out using the HELIOS supercomputer system (IFERC-CSC), Aomori, Japan, under the Broader Approach collaboration, implemented by Fusion for Energy and JAEA, and using the CURIE supercomputer, operated into the TGCC by CEA, France, in the framework of GENCI and PRACE projects. The views and opinions expressed herein do not necessarily reflect those of the European Commission or the ITER Organization.

Personal acknowledgements soon...

Contents

Résumé	5
Résumé	5
Abstract	7
Abstract	7
Acknowledgements	9
Acknowledgements	9
1 Introduction	1
1.1 The challenge of controlling nuclear fusion	1
1.1.1 The stakes	2
1.1.2 The principle	2
Fusion reactions	2
The most favorable fuel: Deuterium-Tritium	3
The Lawson criterion	4
1.2 Magnetic confinement with the tokamak concept	5
1.2.1 Magnetic configuration	6
1.2.2 Coordinate systems	6
1.2.3 Plasma Facing Components, the divertor configuration and vertical stability	8
1.2.4 JET and ITER	8
JET	8
ITER	12
1.3 Outline of the thesis	13
2 Introduction to disruptions and their mitigation	15
2.1 Disruptions and their consequences	16
2.1.1 Disruption phases	16
Thermal quench	16
Current quench	16
2.1.2 Consequences of disruptions	17

	Heat loads	17
	Runaway electrons	18
	Electromagnetic forces	20
2.2	Causes of disruptions	23
2.3	Disruption control strategies	26
2.3.1	Disruption avoidance	27
	Operational domain and scenarios	27
	Event handling	27
2.3.2	Disruption prediction and mitigation	27
	Disruption prediction	28
	Objectives of mitigation for ITER	28
	Pellets	29
	Massive Gas Injection	30
3	Review of knowledge on massive gas injection	33
3.1	Thermal loads mitigation	33
3.2	Mitigation of runaway electron beams	35
3.3	Current quench duration control	39
4	MGI triggered disruptions modeling: fundamentals and simulation tools	41
4.1	Magnetohydrodynamics	41
4.1.1	From kinetic to fluid description ^a	42
4.1.2	MHD equations	43
4.2	Gas-plasma interaction	44
4.2.1	Atomic processes	44
4.2.2	Transport of neutrals	46
4.3	The 1D first principle code IMAGINE	47
4.3.1	Equations and assumptions	47
4.3.2	Simulation domain and numerical scheme	48
4.3.3	Limits of the model	51
4.4	The 3D non-linear MHD code JOREK	51
4.4.1	Equilibrium: Grad-Shafranov equation	52
4.4.2	JOREK equations	52
	The reduced MHD model	52
	Impurities in JOREK	54
	Boundary conditions	55
4.4.3	Initialization, numerics and computational resources	56
5	First principle modeling of neutral gas penetration during massive gas injection	59
5.1	JET shot 86887	60
5.2	Simulation settings	60
5.3	Gas propagation in vacuum	61

^aHazeltine and Meiss 2013.

Contents	13
5.4 Cold front penetration	64
5.5 Energy conservation equations	67
6 3D MHD non-linear MHD modeling of the thermal quench	71
6.1 Proof-of-principle simulation of a thermal quench in JET	71
6.1.1 Set-up of neutral injection	72
6.1.2 MHD triggered by the MGI	72
6.2 Toward code validation and quantitative comparison with experiment	78
6.2.1 Experimental set-up : JET shot 86887	78
6.2.2 Simulation set-up	80
6.2.3 Overdensity created by the MGI	80
6.2.4 MHD instabilities triggered by MGI	87
6.2.5 Radiation aspects	96
6.2.6 Influence of input parameters on the simulations results	102
Hyperresistivity	102
Background impurities	107
Perpendicular ion diffusivity and parallel heat conductivity	111
Summary and outlook	114
Bibliography	115
Symbols, variables and acronyms	123
APPENDIX	128
C Normalization of energy equation for model555	128
D Normalization of ion density equation	131
E Weak form and JOEKEK added terms in model555	131
F Density source term	132

*When Fusion will be ready ? Fusion will be ready
when society needs it.*

Lev Artsimovitch

1

Introduction

1.1 The challenge of controlling nuclear fusion

Since the middle of the 20th century, nuclear power has been increasingly used as an energy source. In spite of having the same "nuclear" word in it, nuclear fission and nuclear fusion are very different, quite the opposite in a sense. Fission releases energy by breaking heavy atoms into lighter ones. It still has a top-level research and broad commercial use in spite of being regularly criticized by politicians and public opinion because of its wastes and potential catastrophes. Flaws that nuclear fusion intrinsically does not have. In fusion, light atoms are joined together to form heavier ones and the fusion reactions quickly stop when the atoms are not heated, which prevents the reaction from getting out of control. Moreover, fusion reactions does not produce long-lived radioactive wastes. Being very efficient but also carbon-emission-free, it could be one solution to the emerging energy crisis.

However, nuclear fusion has the flaw of being incredibly difficult to master. Research and continuous progresses have been made during the last decades and the so-called "fusion power" (meaning the power generated by controlled fusion reactions) increased from a few Watts to tens of MegaWatts in 40 years. Despite the undeniable progress of fusion over the past decades a fusion reactor might still be decades away. The ITER project (for International Thermonuclear Experimental Reactor) is a big step forward towards this goal. In the following introduction, we will briefly review some aspects of the remaining challenges that fusion community and ITER have to face. In sections [1.1.1](#) and [1.1.2](#) we will present the stakes of the fusion research program and its basic principles. Among the diversity of fusion device concepts, the tokamak is undoubtedly the closest one to energy production proof-of-principle with the ITER project. This concept will be presented in

section 1.2. Large instabilities can occur in tokamak plasmas and among them, disruptions trigger a total loss of the plasma confinement and stop completely the fusion reactions, potentially damaging the tokamak in the process. This thesis is motivated by the need for an improved understanding of the physics underlying disruptions and their mitigation.

1.1.1 The stakes

The 21st century is already marked by the issue of energy production. Most of the world nations tend to adopt a lifestyle inspired by the western countries, which is very energy-consuming. Some efforts to decrease global energy consumption are made, but are not sufficient in light of the increase of world population, global warming and the progressive scarcity of resources. These are challenges to humanity which our generation will have to face. "Clean" energy abundance might help solving these challenges and this is why fusion energy must be controlled as soon as possible. Energy production with nuclear fusion is intrinsically safe and almost inexhaustible. It also does not produce heavy radioactive elements like nuclear fission does. We will see in the following sections why this is the case and how we try to achieve fusion. The ITER project (see section 1.2.4) is a big step forward towards this goal, but tremendous efforts still need to be done, first, to finish building it, then to operate it. After ITER, the next step would be DEMO, a prototype of fusion reactor. Because of fusion complexity and the current funding of fundamental research in general, fusion energy will probably not be ready soon enough to tackle today's world issues related to energy. Achieving fusion is still a long-term goal (around 2050) and energy sources like solar, wind or geothermal energy must also be developed and supported.

If the fusion community is able to deliver the plans for a stable, steady-state and competitive fusion reactor, and if society and investors decide to finance its industrial development then a new era of safe and abundant energy could start in the second part of this century.

1.1.2 The principle

What we call nuclear fusion is the union of two light nuclei to form a heavier and stable nucleus. It is difficult to achieve because of the positive charge of nuclei. They repel each other with the Coulomb force, a force proportional to the inverse squared distance between the two nuclei. However, when they are close enough the attractive strong interaction takes over the Coulomb interaction. Usually a temperature around 10 keV, i.e. around 100 millions of degrees Celsius, is enough to get fusion reactions. At this temperature, matter is in the plasma state which means that atoms are completely stripped and that electrons and nuclei are separated.

Fusion reactions The main principle of fusion can be understood looking at the Aston curve (Figure 1.1) which represents the average binding energy per nucleon as a function of the atomic mass. The fusion of two light nuclei will lead to the release of energy because the binding energy of the newly heavier atom is greater than the sum of the

binding energies of the two original nuclei. For heavy nuclei (Uranium for example), the breaking of a nucleus into two lighter ones also releases energy and this is the basis of nuclear fission reactors.

In stars, fusion is the dominant mechanism producing energy. It begins with hydrogen and stars progressively fuse their elements into heavier ones until reaching the top of the Aston curve by creating Iron. Heavier elements are only created by neutron capture processes. On Earth, we obviously want to start with the easiest reaction.

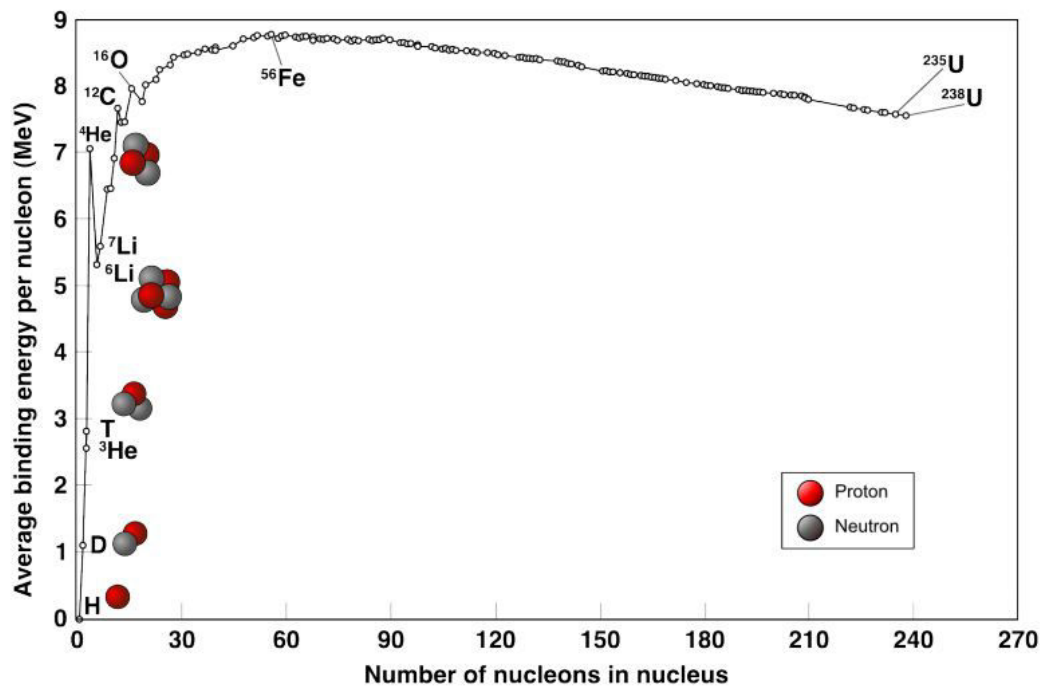


Figure 1.1: *Aston curve - average binding energy per nucleon as a function of the number of nucleons in nucleus*

The most favorable fuel: Deuterium-Tritium For this reason, the most studied fusion reaction is currently the reaction between Deuterium (D) and Tritium (T). They are both isotopes of Hydrogen (H) and their fusion produces an energetic neutron and an α particle (or Helium/He), each product carrying part of the liberated energy (see Figure 1.2). This reaction has indeed the highest cross-section at low energy, i.e. the highest probability for the reaction to occur (see Figure 1.3). The cross-section is maximum for energies of approximately 70 keV, and decreases sharply below 10 keV, which is thus considered as a minimum energy for a nuclear fusion reactor to be viable. To have a significant amount of particles at such energies, the D-T fuel must be heated up to temperatures above several keV, i.e. around hundreds of millions of Kelvin degrees, where the matter is in the plasma state. Regarding fuel resources, Deuterium represents 0.016% of the Hydrogen atoms on Earth which is enough to power mankind for millions of years. Tritium does not exist naturally on Earth but can be produced from Lithium. It is planned to produce it directly in fusion reactors thanks to Lithium blankets positioned around the

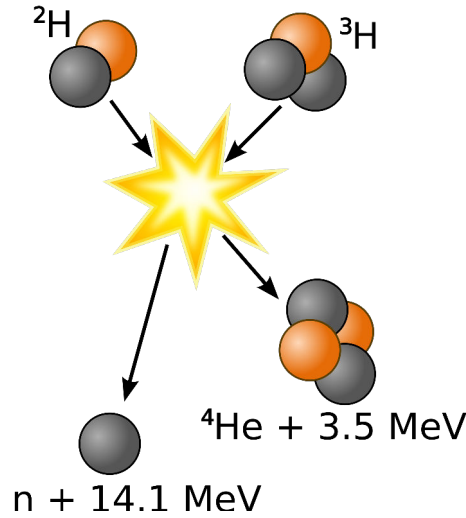


Figure 1.2: *Deuterium - Tritium fusion reaction*

vacuum vessel. The Lithium being also abundant on Earth we would have enough fuel for tens of thousands of years, assuming that fusion energy would be the only energy source.

The Lawson criterion To produce energy with a plasma, the losses must be compensated by the heating power P_{heat} . This heating power is the sum of the fusion power carried by the α particles and the auxiliary power, i.e. the external power needed to confine and heat the plasma ($P_{heat} = P_{\alpha} + P_{aux}$). The neutrons produced by the fusion reactions does not interact with the plasma because of their neutrality and only the α particles can heat the plasma (with $P_{\alpha} = P_{fus}/5$). In the fusion community, we define the quality factor Q as the ratio of the fusion power over the auxiliary power $Q = P_{fus}/P_{aux}$. We want it to be as high as possible and one of ITER's main goal is to achieve $Q = 10$ during a few hundreds of seconds.

The energy confinement time τ_E , which characterizes the decay time of the energy of the plasma is defined by the energy content W_{th} divided by the losses P_{loss} : $\tau_E = W_{th}/P_{loss}$. Assuming that $T_i = T_e = T$, the thermal energy content is divided in half between the electrons and ions and we have $n_D = n_T = n_e/2$, thus $W_{th} = 3n_e kT$ where n_D and n_T are respectively the ion densities for deuterium and tritium and n_e is the electron density. Then, the condition that the injected power compensates the losses gives an approximate relation between $n_e \tau_E$, called the Lawson criterion, the quality factor Q and the plasma temperature T . The condition to achieve sustainable fusion (meaning Q tends to infinity) is usually expressed with the "triple product" $n_e T \tau_E$ being above a certain value:

$$n_e T \tau_E > 3 \times 10^{21} \text{ keV} \cdot \text{s} \cdot \text{m}^{-3} \quad (1.1)$$

Two ways of triggering fusion reactions in a plasma are currently explored. The first operates at high density and low confinement time and the second at low density and high confinement time. The former is investigated for example at the NIF^a (National Ignition

^aHurricane, Callahan, et al. 2014.

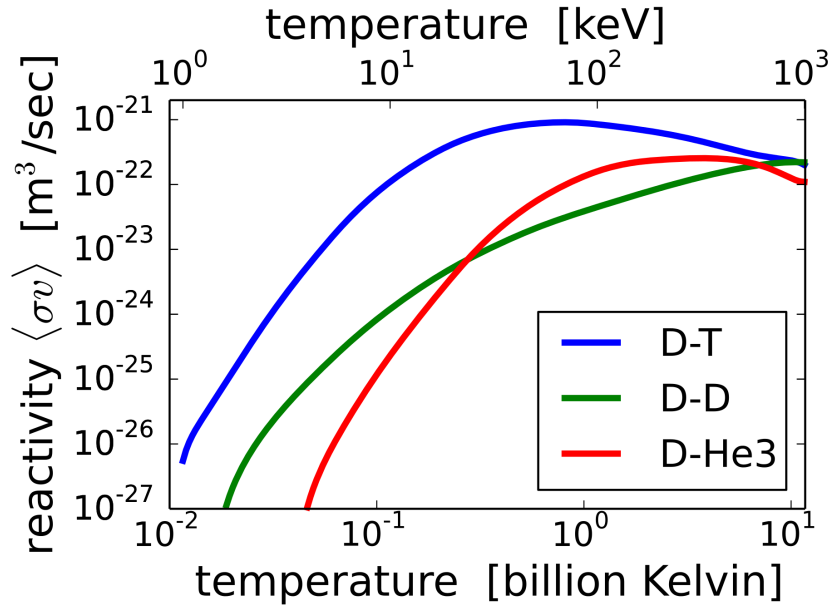


Figure 1.3: *Cross-section of the D-T reaction in m^3s^{-1}*

Facility) in the US and the Laser Megajoule in France and is called "inertial confinement fusion". It consists in firing highly powerful and collimated lasers on a millimeter-size D-T solid target. The other way, for which one particular concept will be detailed in the following section, implies to reach steady state plasma conditions. It means that the plasma should be confined for a very long time. This is the case in the stars, where the gravity naturally retains the plasma. On Earth, we do not have access to such a large gravitational force. Instead, magnetic fields are used to balance the thermal pressure of the plasma. This is called "magnetic confinement fusion". The plasma is usually confined in a torus-shaped vacuum vessel and we will now detail the concept which has been the most successful so far, the tokamak.

1.2 Magnetic confinement with the tokamak concept

A plasma is an ionized gas where electrons and ions are separated and sensitive to magnetic and electric fields. At temperatures needed to achieve fusion, these particles have a mean-speed \gg km/s. If these particles are not confined they will be lost into the walls almost instantaneously. They must be confined to stay in the vessel long enough to fuse. Most laboratories are working with a magnetic confinement of these particles. The movement equation of a charged particle in a magnetic field is indeed:

$$m \frac{d\mathbf{v}}{dt} = q\mathbf{v} \times \mathbf{B} \quad (1.2)$$

The particles have a helical motion around the magnetic field lines as represented on Figure 1.4. This gyration around the magnetic field is characterised by the cyclotron pulsation $\omega_s = q_s B / m_s$ and the gyration, or Larmor, radius $\rho_s = v_{th,s} / \omega_s$, where q_s , m_s and $v_{th,s}$ are respectively the charge, the mass and the thermal velocity ($v_{th,s} = \sqrt{2k_B T / m_s}$) of the species (ions or electrons). Particles also have a drift movement due to the centrifugal force and the gradient of the magnetic field. By closing the magnetic field lines around a torus shape we can confine the particles.

Several types of confinement concepts have been studied recently but the concept which

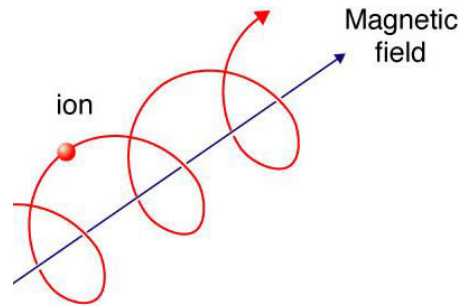


Figure 1.4: *Particle motion around magnetic field lines*

is the most promising is the tokamak.

1.2.1 Magnetic configuration

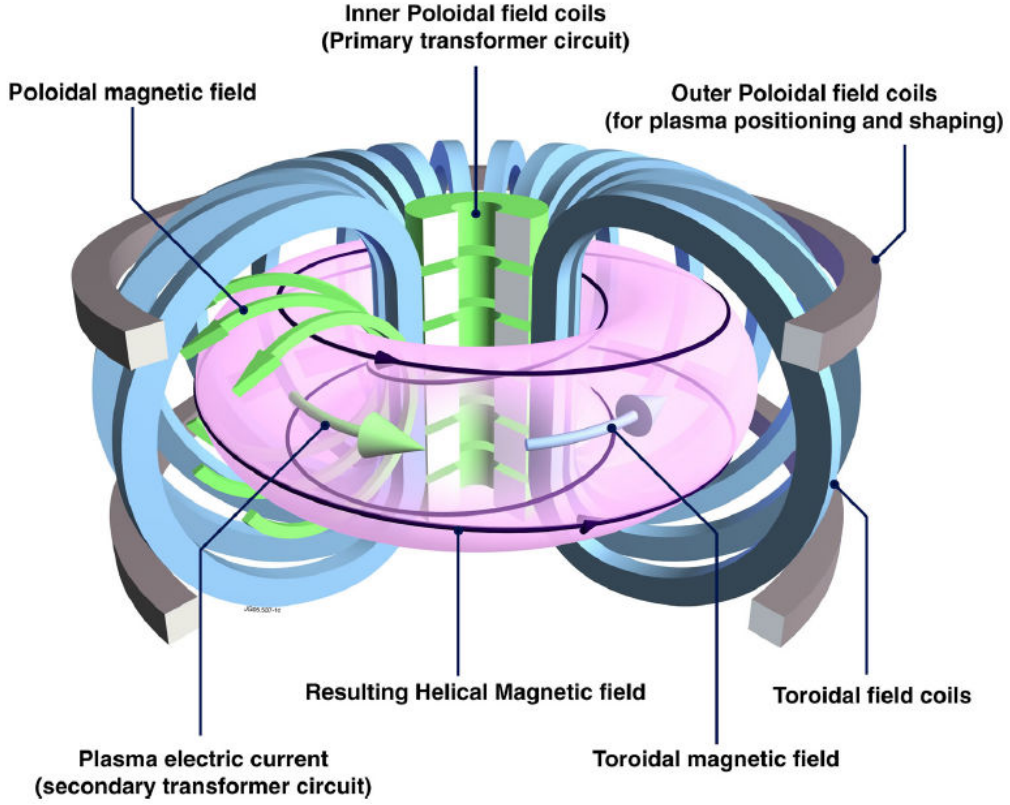
In a tokamak, the plasma is confined in a toroidal chamber by a helical magnetic field, as can be seen in Figure 1.5, which shows a schematic view of a tokamak. The toroidal field coils are responsible for the generation of the toroidal magnetic field when the central solenoid (or inner poloidal field coils) generates the plasma current. In a tokamak, it is the plasma current which generates most of the poloidal magnetic field. The outer poloidal field coils are used for plasma positioning and shaping. This plasma current is obtained by varying the magnetic flux in the central solenoid, while the plasma acts as the secondary winding of a transformer. This configuration provides a very good confinement of the plasma.

Other concepts are also studied, like stellarators where the poloidal component of the magnetic field is not generated by the plasma current but with twisted and complex coils. However, none of these concepts has achieved tokamak performance yet.

1.2.2 Coordinate systems

Toroidal coordinates are mostly used in the study of tokamaks, as defined in Figure 1.6. In Figure 1.6, magnetic surfaces are also represented. They are surfaces defined by the magnetic field lines. A general form for B , in an axisymmetric tokamak, is

$$\mathbf{B} = F(\psi) \nabla \varphi + \nabla \psi \times \nabla \varphi \quad (1.3)$$

Figure 1.5: *Schematic view of a tokamak*

where ψ is the poloidal magnetic flux, which is a label of magnetic flux surfaces, φ is the geometric angle in the toroidal direction and F is a flux function.

We define the safety factor q of the magnetic configuration as the pitch of the magnetic field lines. q is equal to the number of turns made in the toroidal direction for each turn in the poloidal direction. The formal definition of q is:

$$q = \frac{1}{2\pi} \int \frac{\mathbf{B} \cdot \nabla \varphi}{\mathbf{B} \cdot \nabla \theta} d\theta \quad (1.4)$$

In the assumption of a large aspect ratio ($a/R_0 \simeq \varepsilon$), we can define the safety factor q as

$$q \simeq \frac{r B_T}{R_0 B_p} \simeq \frac{m}{n} \quad (1.5)$$

where B_T and B_p are respectively the toroidal and poloidal component of the magnetic field. Note that an adequate system of toroidal coordinates in tokamak geometry can then be defined by (ψ, θ, φ) , where θ is such that the safety factor is only a function of ψ . Magnetic surfaces in which q is a low order rational will be of particular importance in the study of MagnetoHydroDynamic (MHD) instabilities and disruptions (see section 4.1). On these magnetic surfaces, field lines close back on themselves after one or more toroidal turns. Such surfaces are called rational surfaces or resonant surfaces.

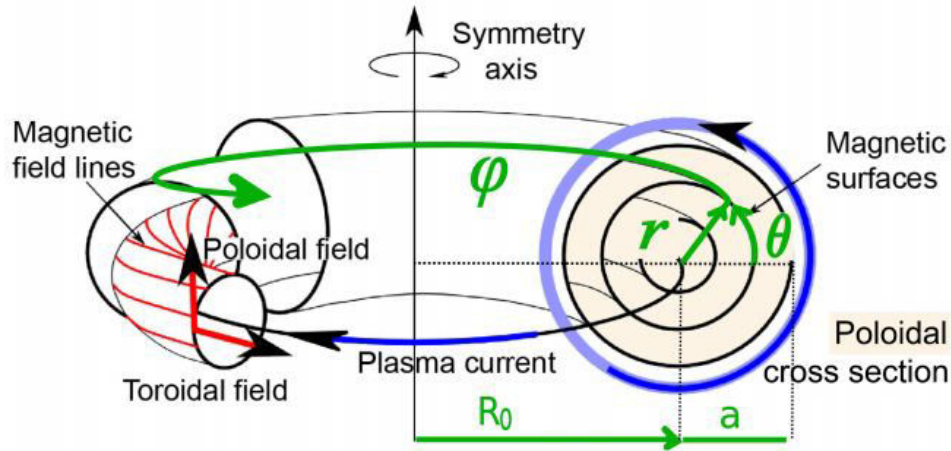


Figure 1.6: *The tokamak magnetic configuration and the toroidal coordinate system (r, θ, φ) . The geometry of the torus can be described by its minor radius a and major radius R_0 (at the magnetic axis)*

1.2.3 Plasma Facing Components, the divertor configuration and vertical stability

Another important part of the tokamak are the plasma facing components (PFCs) which are directly heated by the plasma, particularly during disruptions. Since the discovery of the so-called H-mode^b (for High confinement mode), most tokamaks operate in divertor configuration. Figure 1.7 shows this type of magnetic configuration. The aim of the divertor configuration is to separate the core of the plasma (Region I) and the walls by an area called the Scrape-off layer (Region III) where the field lines are open and goes to the divertor chamber. This chamber then receives most of the heat loads. To do that, a separatrix must be formed to separate these two regions. This separatrix presents a so-called X-point where the poloidal magnetic field is zero. The divertor configuration is intrinsically unstable vertically and a feedback system is used to control the vertical position of the plasma. Tokamaks of different sizes and specifications have been constructed since the 80's, from middle-size machine such as DIII-D, ASDEX Upgrade or Tore Supra to large machines such as TFTR, JT60-SA or JET.

1.2.4 JET and ITER

JET At the moment, the largest tokamak in the world is the Joint European Torus (JET), which has reached an amplification factor of $Q \simeq 0.7$. It is located in the Culham Science Centre for Fusion Energy (CCFE) near Oxford, UK. It has achieved the world record of Fusion power produced (16 MW) and is now equipped with "ITER-like" walls made of Tungsten and Beryllium. In the next few years, new experimental campaigns will attempt at breaking this record and testing relevant D-T plasma scenarios for ITER in a Tungsten environment. JET specificities are given in Table 1.1 and an inside view of JET

^bWagner, Becker, et al. 1982.

is shown in Figure 1.8.

Major radius R	2.96 m
Toroidal magnetic field B_T	3.85 T
Plasma current I_p	Maximum 4.8 MA
Plasma volume	100m ³
Typical duration of a plasma shot	10 – 20s
Plasma thermal energy	$\simeq 10$ MJ
Plasma magnetic energy	$\simeq 10$ MJ

Table 1.1: JET specificities

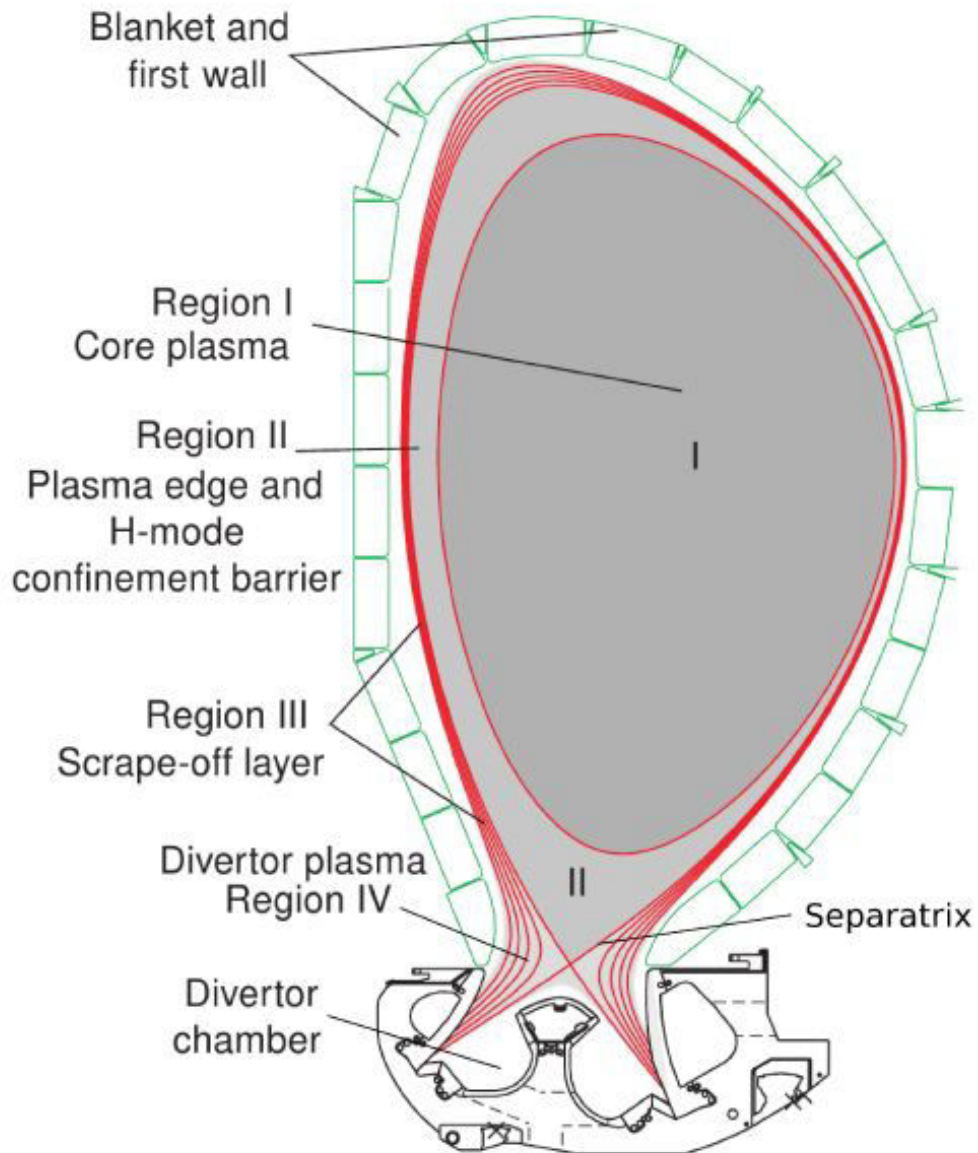


Figure 1.7: *Magnetic topology in the poloidal plane. Lines are flux surfaces.*

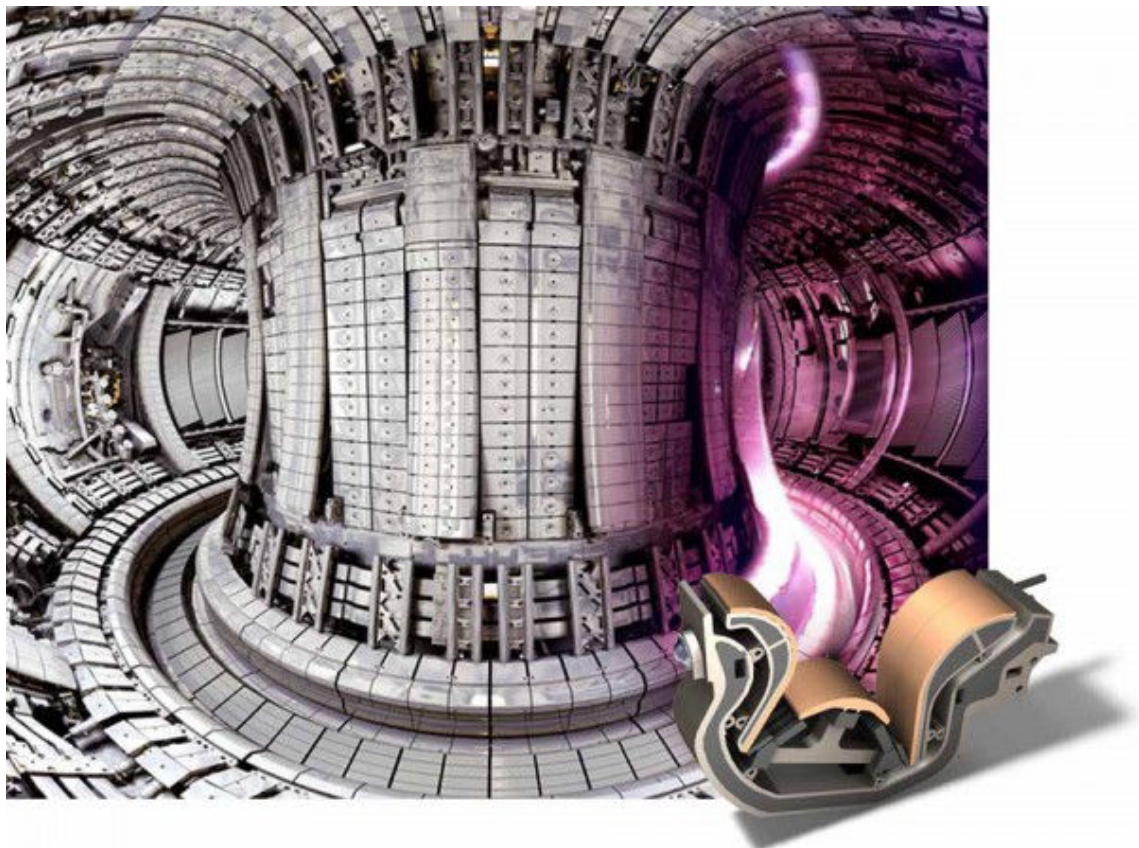


Figure 1.8: *JET inside view*

ITER The main objective of ITER is to prove the feasibility of energy production by nuclear fusion. ITER will not be a test reactor but the largest experimental bench to study and control plasma instabilities and transport phenomena which currently limits the performance of tokamak devices. ITER's first objective is to confine a D-T plasma at a temperature above $10keV$ for a few hundreds of seconds and thus trigger nuclear fusion reactions with a thermal fusion power output of several hundreds of MW, i.e. achieve $Q = 10$ during 400s. The second objective is to operate in steady-state, i.e. to operate at a lower Q for thousands of seconds. In future reactors, a plasma discharge should last for days, weeks, months or even years.

One of the most difficult present issues to solve in order to achieve these objectives is the occurrence of tokamak disruptions, which are the focus of this thesis. Main ITER specificities are summarized in table 1.2 and Figure 1.9.

Major radius R	6.20 m
Toroidal magnetic field B_T	5.3 T
Plasma current I_p	Maximum 15 MA
Plasma volume	830m ³
Duration of a plasma shot	up to 1000s
Plasma thermal energy	$\simeq 350$ MJ
Plasma magnetic energy	$\simeq 400$ MJ

Table 1.2: ITER specificities

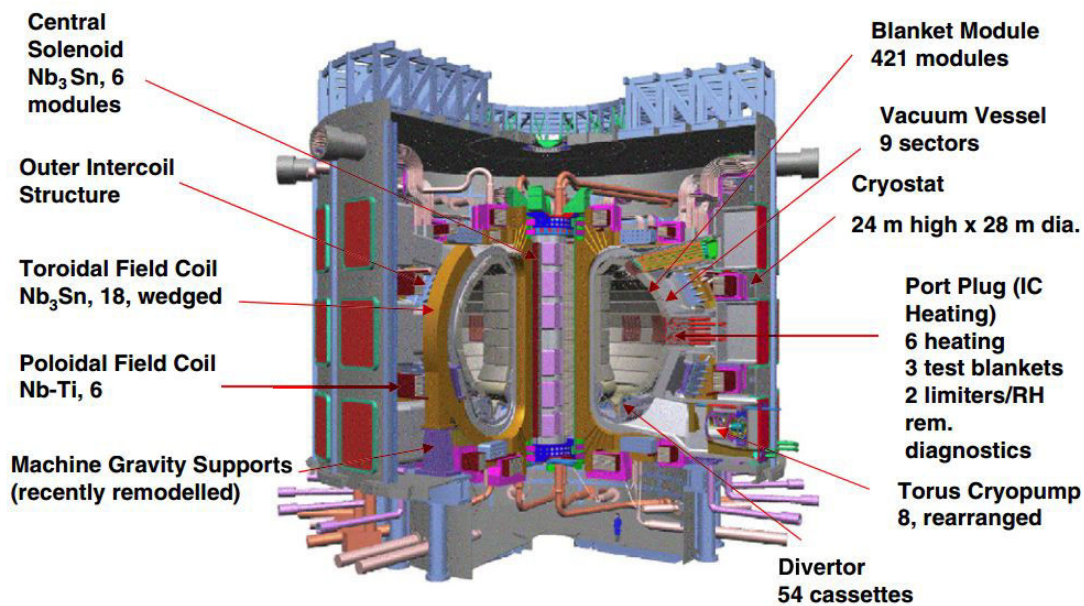


Figure 1.9: *The ITER tokamak*

1.3 Outline of the thesis

This manuscript is constructed as follows: chapter 2 will introduce tokamak disruptions and their mitigation, chapter 3 will review the current status of research on disruption mitigation by massive gas injection (MGI) focusing on current knowledge from experiments and modeling. Chapter 4 will present the theoretical framework used for disruptions modeling and the simulation tools developed and used in this thesis. Next chapters will focus on a specific JET shot with a MGI of pure D_2 . Chapter 5 will focus on numerical and theoretical study of the dynamic of the MGI neutral gas cloud and its interaction with the plasma. Chapter 6 will present numerical and theoretical work aiming at a better understanding of the dynamic of MGI-triggered disruptions. Chapter 6.2.6 will summarize the results obtained and give perspectives for future work.

2

Introduction to disruptions and their mitigation

A tokamak disruption^a is a violent loss of plasma confinement due to the development of a global instability. Usually, a disruption is triggered by the crossing of a stability limit or the occurrence of an unexpected event like the failure of a heating system. This loss of plasma confinement results in the fast decrease of the plasma temperature and the plasma current. This violent loss has potentially deleterious effects on the tokamak. These effects on the tokamak increase with machine size and will thus be more problematic in ITER than in present devices. In fact, they already lead to problems in present large tokamaks and have led to the routine use of Disruption Mitigation Systems (DMS) for example on JET and ASDEX Upgrade. The ITER DMS design is currently underway and overviews on this topic are given in recent articles^b. This manuscript is focused on disruption physics and on one of the most promising mitigation method for ITER, Massive Gas Injection (MGI). An overview on disruptions, their consequences and control strategies will be given in this chapter. The current status of research on disruption mitigation by MGI will be discussed in more detail in chapter 3.

^aHender, Wesley, et al. 2007; Boozer 2012; Schuller 1995.

^bLehnen, Aleynikova, et al. 2014; E. M. Hollmann, Aleynikov, et al. 2015.

2.1 Disruptions and their consequences

2.1.1 Disruption phases

A disruption comprises 2 consecutive phases: the Thermal Quench (TQ) where the thermal energy is lost and the Current Quench (CQ) where the plasma current is lost due to the very large resistivity of the cold post-TQ plasma. The evolution of characteristic quantities during a typical disruption is shown in Figure 2.1.

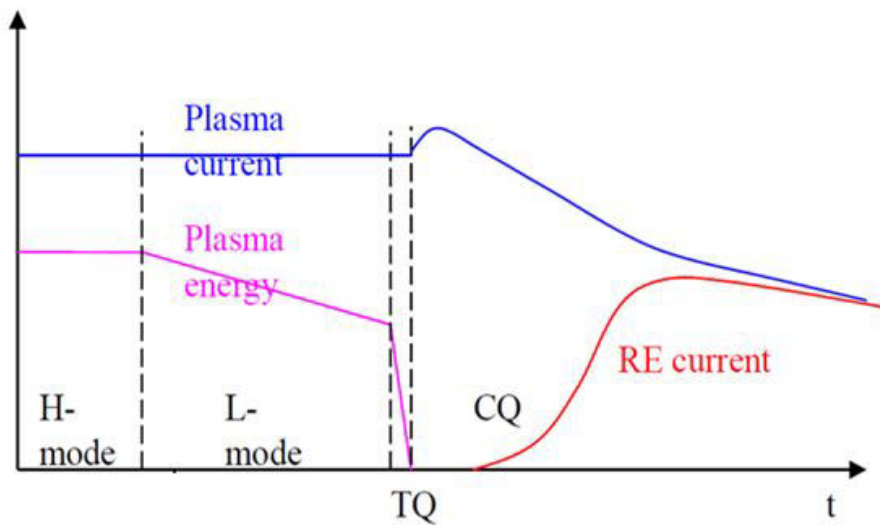


Figure 2.1: *Disruption phases: The Thermal Quench (TQ) and The Current Quench (CQ)*

Thermal quench The TQ is the first phase of a plasma disruption. During this phase almost all the thermal energy of the plasma is lost on a duration several orders of magnitude lower than the pre-disruption energy confinement time. It is characterized by a violent loss of the plasma confinement and an important MHD activity. Most of the plasma thermal energy is conducted or convected onto the PFC or lost by radiation, which can damage the PFCs. The typical duration of this phase is between a few tens of microseconds and a few milliseconds. It is always associated to an important increase of magnetic fluctuations measured by the Mirnov coils. An increase ("bump") of the total plasma current is also observed experimentally in all disruptions (5 to 20 % of the pre-disruption plasma current). The precise dynamics of the TQ is however quite complicated and depends on plasma parameters and disruption causes. One aim of this thesis is to investigate and simulate TQs triggered by MGI (Chapter 6).

Current quench At the end of the thermal quench, the plasma temperature has fallen to $\simeq 10$ eV as most of the thermal energy has been dissipated. As the plasma electrical resistivity given by the Spitzer^c formula is proportional to the plasma temperature to the

^cJ. Wesson 2004.

power $-3/2$,

$$\eta \propto T^{-3/2} \quad (2.1)$$

the post-TQ plasma is very resistive and the plasma current cannot be sustained anymore. The duration of the current decrease is typically between a few milliseconds and a few hundreds of milliseconds, depending on the machine size, the configuration of conducting structures or the PFCs material. During this phase, all the magnetic energy is lost. Part of its energy is converted to thermal energy and dissipated by radiation or conducted to the PFCs. The rest is dissipated by Joule effect in the tokamak coils and the passive structures. Indeed, the violent decrease of the plasma current induces currents in the tokamak structure. Halo currents are also created when the feedback system is not able to control the plasma anymore. Finally, the fast decrease of the plasma current gives rise to a large toroidal electric field which accelerates electrons of the post-TQ plasma. Under certain conditions, relativistic electrons, or "Runaway" Electron (RE) beams, can be generated and damage the tokamak walls when they are lost. All these consequences of disruptions will now be discussed.

2.1.2 Consequences of disruptions

Disruptions have three types of potentially deleterious effects: heat loads on the Plasma Facing Components (PFCs), the formation of Runaway Electron (RE) beams and electromagnetic forces on the tokamak structure.

Heat loads During the TQ and CQ phases, conducted heat loads to the PFCs can result in local melting or sublimation. They are usually strongest to divertor strike points but can also heat the PFCs of the main chamber. An example of IR images during a VDE and a density limit disruption on JET are shown on Figure 2.2. These images show the PFCs temperature which is directly related to heat loads on the tokamak components. To evaluate them, we use the ablation parameter ϕ_d which is linked to the energy E deposited on the walls and the deposition time τ :

$$\phi_d = \frac{E}{\sqrt{\tau}} \text{ MJ} \cdot \text{m}^{-2} \cdot \text{s}^{-1/2} \quad (2.2)$$

Most of tokamak walls and divertor plates can support an ablation parameter up to $50 \text{ MJ} \cdot \text{m}^{-2} \cdot \text{s}^{-1/2}$ (for Tungsten PFCs, ϕ_d is lower for a Be first wall). The thermal energy of the plasma (maximum of 10 MJ in JET) is not large enough in current tokamaks to damage the walls with only one disruption. However, walls can be damaged if repetitive uncontrolled disruptions occur and progressively melt or ablate the components (see Figure 2.3 in JET). For example, the most pessimistic estimation for ITER^d is an ablation parameter around $450 \text{ MJ} \cdot \text{m}^{-2} \cdot \text{s}^{-1/2}$ for a disruption with a 1 ms thermal quench and 100% of the energy conducted to the walls. One such disruption could melt

^dHender, Wesley, et al. 2007.

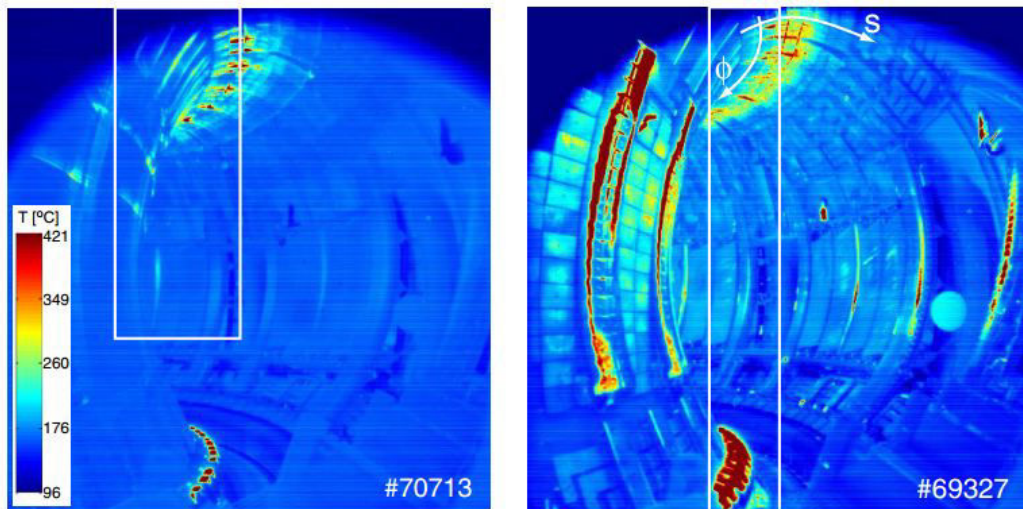


Figure 2.2: Images from the wide angle IR camera during a VDE (left) and a density limit disruption (right) in JET. Figure from [G. Arnoux, Loarte, et al. 2009]

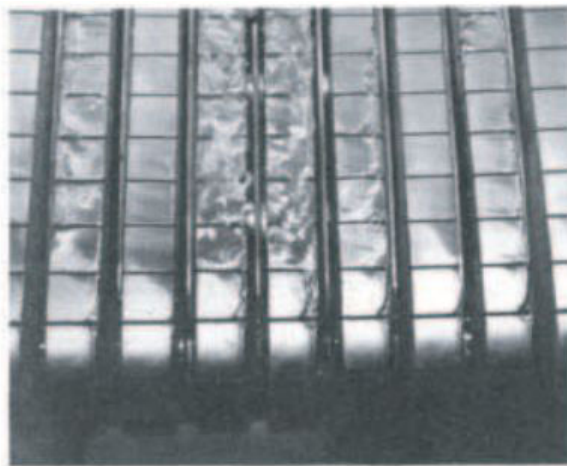


Figure 2.3: Partial melting of a Beryllium divertor in JET [Loarte, Saibene, et al. 2005]

kilograms of wall materials^e, which would limit the tokamak performance and its lifetime. It is thus mandatory to mitigate these heat loads on ITER. It should be noted that recent experiments show that only a fraction of the thermal energy is conducted to the divertor^f and that a mechanism called "radiative shielding"^g seems to occur after the beginning of the Tungsten wall ablation. But even taking these into account, the heat loads would still be too high in ITER.

Runaway electrons During the CQ, a large electric field is induced by the fast decay of I_p and accelerates electrons. A critical field can be defined above which the acceleration

^eHassanein, V. Sizyuk, et al. 2013; Lehnen, Aleynikova, et al. 2014.

^fG. Arnoux, Loarte, et al. 2009.

^gLoarte, Lipschultz, et al. 2007; T. Sizyuk and Hassanein 2014.

due to electric field is higher than the electron braking due to collisions and radiative losses. If the collisional drag only is taken into account, a formula for the critical field is

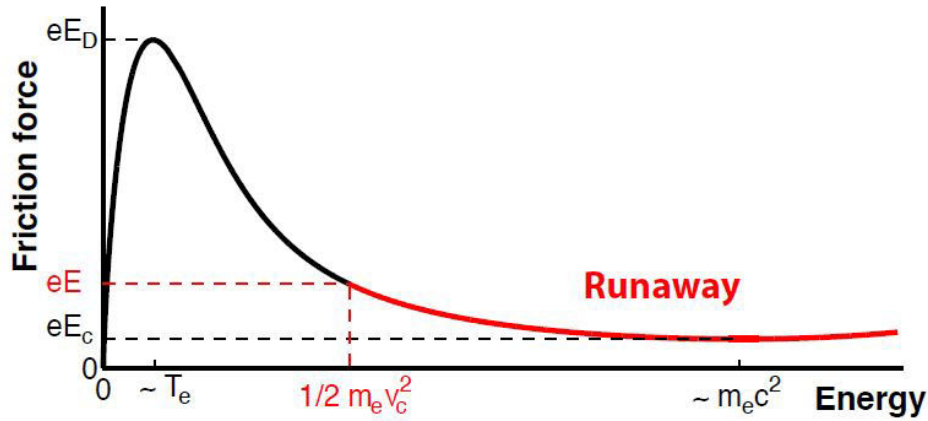


Figure 2.4: *Friction force as a function of the energy of electrons. If the electric field is above the critical electric field E_c , i.e. eE is higher than the friction due to collisions, electrons of energy above $1/2m_e v_c^2$ are accelerated to relativistic velocities.*

given by:

$$E_c = n_e e^3 \ln \Lambda / 4\pi \epsilon_0^2 m_e c^2 \quad (2.3)$$

If the electric field created during the CQ is higher than the critical electric field, part of the electron population of the plasma is accelerated to relativistic velocities, as sketched on Figure 2.4. Note that the value of the critical electric field directly depends of the plasma density n_e . A high enough density theoretically prevents this primary generation of runaway electrons. Moreover, recent experiments and modeling show that the effective critical electric field is significantly higher than given by 2.3, presumably due to the strong dependence of the primary generation on temperature and to synchrotron radiation losses^h. When this seed of relativistic electrons is created, runaway electron population can increase due to avalanches processes such as knock-on collisionsⁱ. Runaway electron beams are created and very localized damage can result when they strike PFCs. An example of runaway electron damage can be seen in Figure 2.5. Depending on the timescale of the runaway loss, a significant fraction of the remaining magnetic energy of the plasma can be converted into kinetic energy. The wetted area and the deposition duration then depend strongly on the mechanisms inducing the RE loss. A vertical or a radial displacement of the RE beam can lead to a "scraping-off" of REs, but fast losses of the entire beam are also observed. Although not experimentally confirmed yet, it is thought that its fast loss is related to $q = 2$ MHD instabilities of the beam. Important research is currently devoted to the study of runaway electron generation, both experimentally and by modeling. Section 3.2 will present recent experiments aiming at mitigating a RE beam on JET.

^hPaz-Soldan, Eidietis, et al. 2014; Stahl, Hirvijoki, et al. 2015; Granetz, Esposito, et al. 2014.

ⁱNilsson, Decker, et al. 2015.

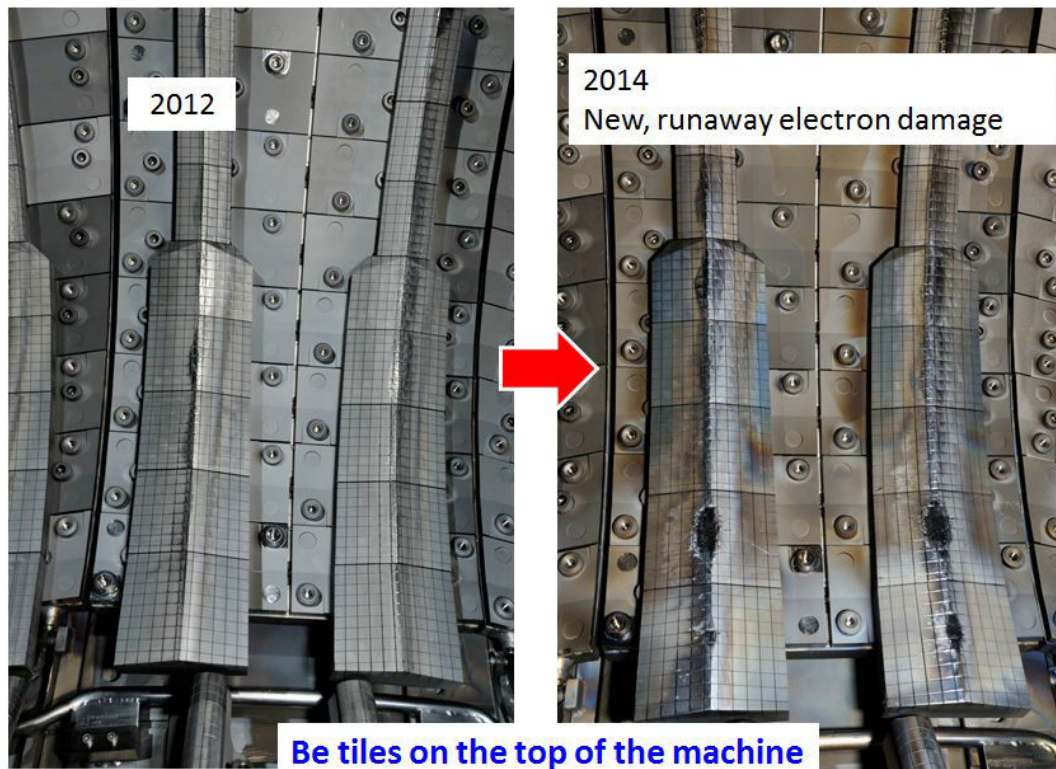


Figure 2.5: *Runaway electron damage on JET Be tiles.*

Electromagnetic forces During the CQ, large currents can be induced in the conducting vessel walls or driven by direct contact with the plasma current channel. The former are called eddy current and the latter halo currents. These currents flowing in the tokamak structure can result in $j \times B$ forces which can damage vessel components^j (see Figure 2.6). The halo current flows in an outer shell around the plasma and enters the tokamak structure around the plasma contact point, as sketched on Figure 2.7. Short CQs result in large eddy currents whereas long CQs result in large halo currents. An optimal CQ duration must be found in order to reduce both eddy and halo currents.

^jHumphreys and A. G. Kellman 1999.

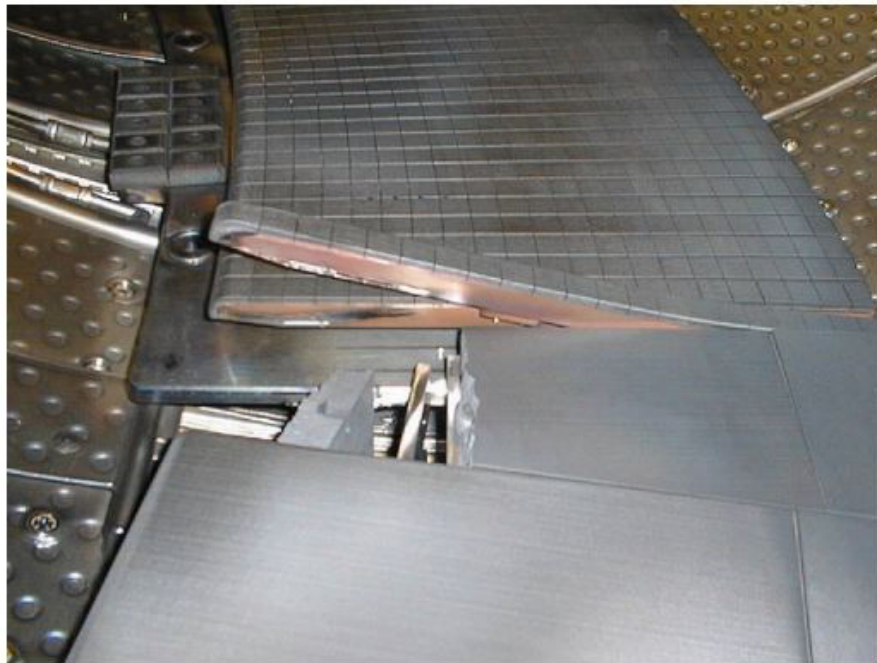


Figure 2.6: *Bending of a PFC due to eddy currents created by a disruption in the tokamak Tore Supra*

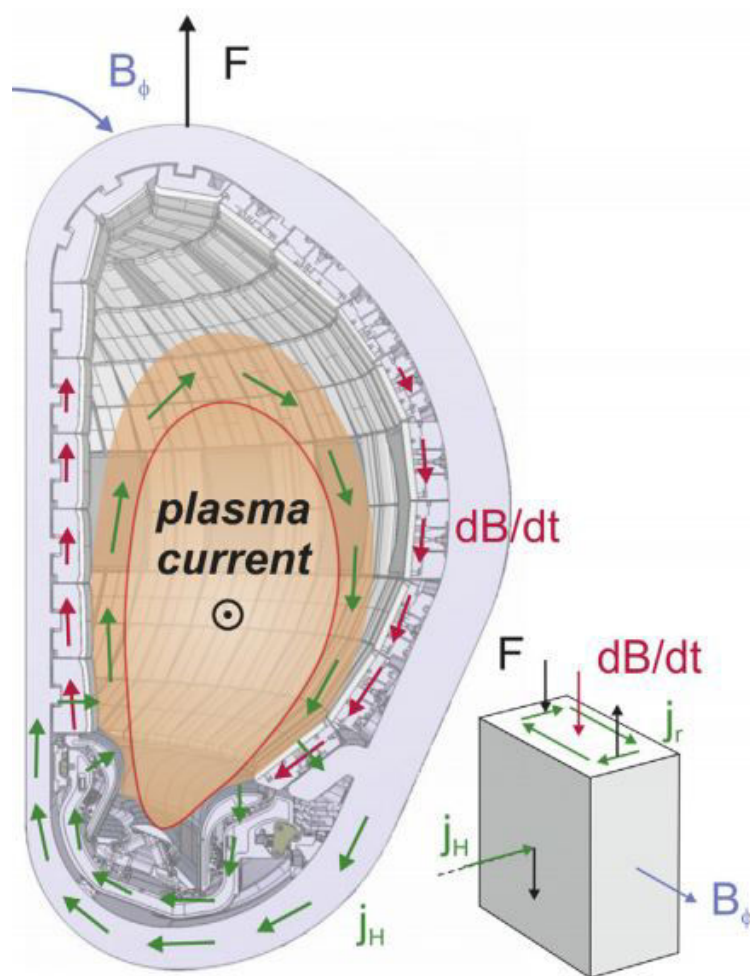


Figure 2.7: Schematic of a downward VDE and associated currents, field and forces in the vacuum vessel and the blanket modules in ITER. Green arrows represent the halo current when red arrows represent the eddy current. Figure from [Lehnen, H R Koslowski, et al. 2014]

2.2 Causes of disruptions

The TQ is always associated to an important MHD activity, even in the case of a radiative collapse. The experimental burst of magnetic fluctuations characteristic of the TQ is associated to the destabilization of MHD modes and the subsequent loss of magnetic surfaces. The type of MHD mode depends on the resonant surface in which they are created, thus they are labelled by the value of the safety factor in these surfaces, $q = m/n$. Main modes responsible for the TQ are the internal kink mode 1/1 and the tearing modes 2/1 and 3/2 (see an example Figure 2.8). Their growth triggers the breaking of magnetic surfaces and a loss of confinement.

In MHD theory, the magnetic surfaces are sensitive to the parallel current and to the

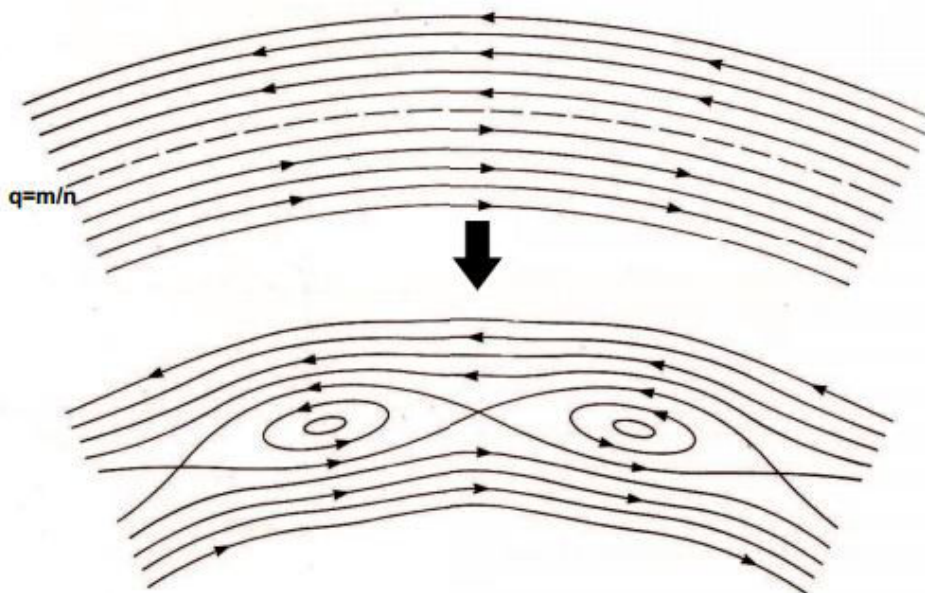


Figure 2.8: *Example of a MHD mode creating magnetic islands on a resonant (or rational) magnetic surface*

pressure profile. A plasma density that exceeds the Greenwald limit^k, a rapid plasma edge cooling or a strong internal transport barrier (ITB) strongly modify the pressure profile and can destabilize MHD modes such as Tearing modes. Ballooning modes and their stability limit also constrain the shape of the pressure profile.

Moreover, external kinks and Resistive Wall Modes (RWM) limit the edge value of the safety factor and thus the maximum plasma current achievable in the device. To avoid RWMs, q_{edge} should indeed be above 2, and the plasma current is thus reduced to increase it. Finally, there is also a low-density limit below which REs are generated.

All these limits are operational limits for tokamaks and a convenient representation is the Hugill diagram (see Figure 2.9). The robustness of the magnetic surfaces confining the plasma thus determine the plasma tendency to disrupt.

^kGreenwald 2002.

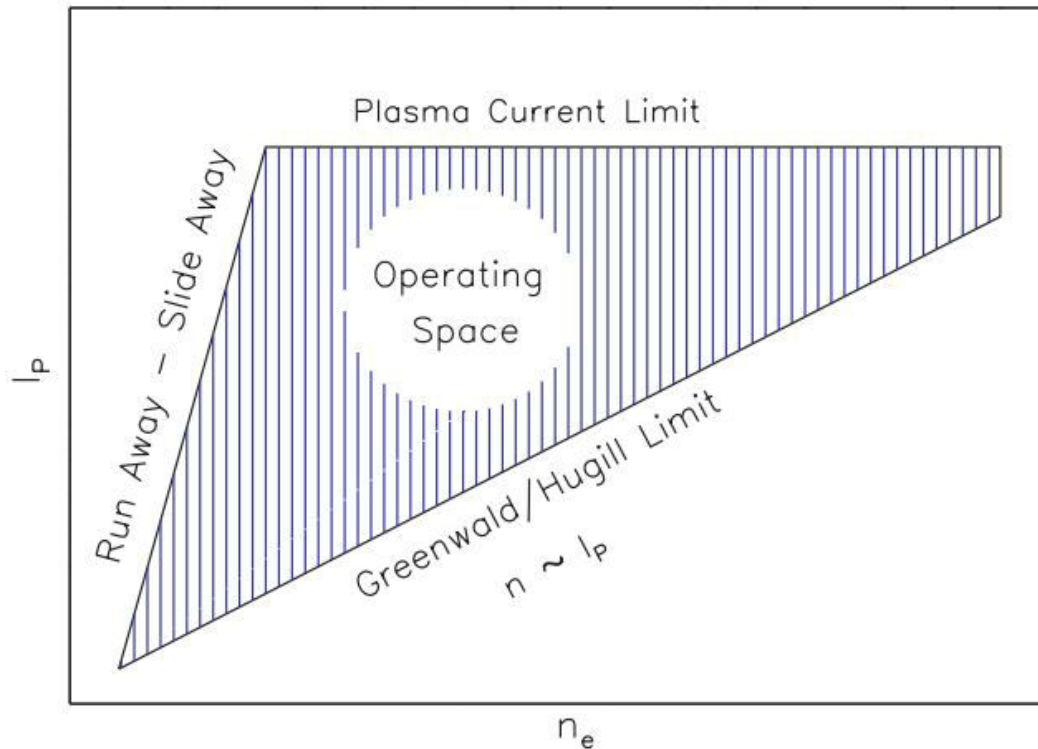


Figure 2.9: A schematic of the operating space for tokamaks. Operation is bounded by a low-density limit characterized by run-away fast electrons and a high-density limit proportional to the plasma current. The limit on plasma current is due to MHD kink instabilities. Figure from [Greenwald 2002]

The robustness of the plasma centering is also important. D-shape plasmas are indeed vertically unstable and a precise feedback control is used to avoid so-called Vertical Displacement Events (VDEs). During a VDE, a hot low-resistivity plasma collides with the first wall and the thermal quench occurs when enough plasma has been stripped by the walls.

A recent review¹ on the JET tokamak listed the main underlying causes of these disruptions. Figure 2.10 illustrates the variety of physical or technical phenomena that can trigger a disruption in JET and some of them are given in Tables 2.1 and 2.2.

¹De Vries, Johnson, et al. 2011.

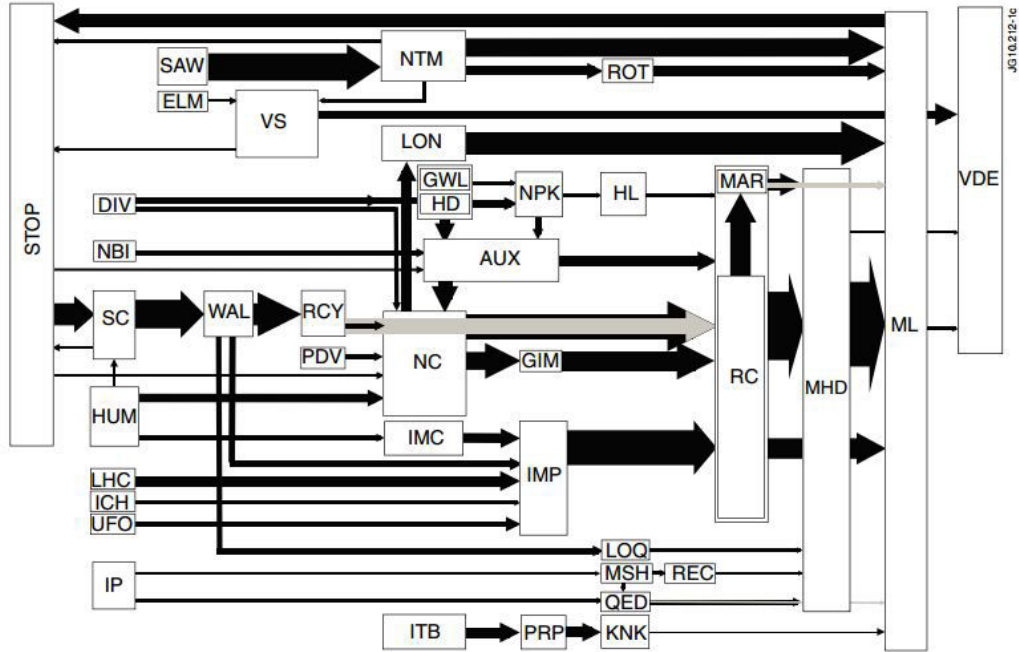


Figure 2.10: A schematic overview, showing the statistics of the sequence of events for 1654 unintentional disruptions at JET during the period 2000 to 2010. The width of the connecting arrows indicates the frequency of occurrence with which each sequence took place (only those paths with an occurrence of $> 0.2\%$ are shown). Note that the disruption process could start at any node (event) in the overview, which generally, but necessarily, flows from left to right. The labels correspond to those listed in tables 2.1 and 2.2.

Main types of physics problem	Label
General (rotating) $n = 1$ or 2 MHD	MHD
Mode lock	ML
Low q or $q_{95} \simeq 2$	LOQ
Edge q close to rational (> 2)	QED
Radiative collapse ($P_{rad} > P_{in}$)	RC
Greenwald limit (nGW)	GWL
Strong pressure profile peaking	PRP
Large edge localized mode (ELM)	ELM
Vertical displacement event	VDE

Table 2.1: Examples of physics problems

Type of technical problem	Label
Impurity control problem	IMC
Influx of impurities	IMP
Density control problem	NC
Problem with vertical stability control	VS
Human error	HUM

Table 2.2: Examples of technical problems

More details can be found in [De Vries, Johnson, et al. 2011; Schuller 1995] and methods to avoid these physics problems will now be discussed.

2.3 Disruption control strategies

We have seen in section 2.2 that disruptions have multiple causes and in section 2.1.2 that their consequences can be deleterious for the tokamak walls and structure. They must be avoided and multiple strategies are currently developed and tested. The problem of disruptions can be tackled at different times. In section 2.3.1, the disruption avoidance schemes will be presented. The aim is to operate the tokamak in a "disruption-free" domain (passive avoidance) and to be able to answer to any spontaneous events (active avoidance) by adapting the scenario to recover a stable plasma.

If the control system is not able to do so (or if it does not have enough time) the plasma must be shut down in a way which does not damage the tokamak. It is what is called the mitigation of disruptions. Different methods will be presented in section 2.3.2 and chapter 3. A sketch of these different levels of control is presented in Figure 2.11.

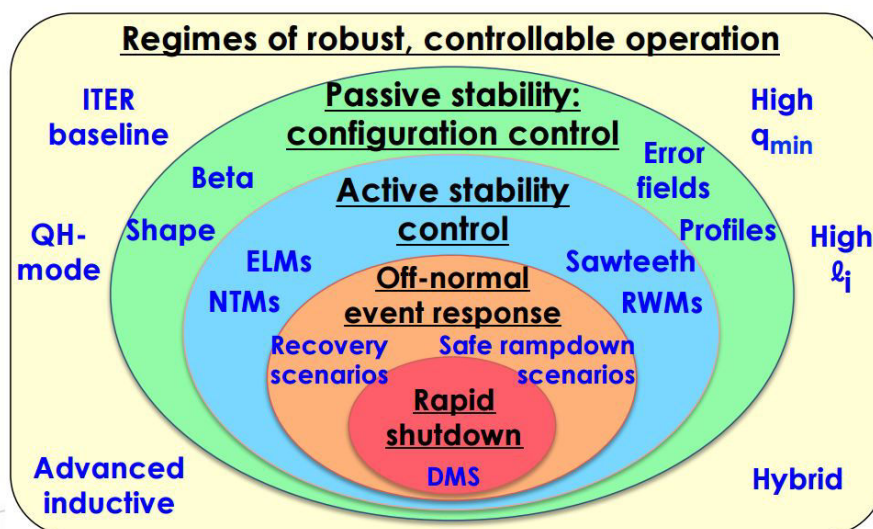


Figure 2.11: Figure from Ted Strait presentation at the ITPA MHD in ITER, showing the different levels of disruption control strategies.

2.3.1 Disruption avoidance

Operational domain and scenarios To avoid disruptions, the first thing to do is to operate as far as possible from disruptions operational limits (recall Figure 2.9). It means that plasma scenarios must be designed taking these limits into account. An example of an advanced scenario developed at JET can be found in [Rapp, Corre, et al. 2009] where the aim is to achieve maximum performance while avoiding the trigger of large disruptive MHD instabilities like $m/n = 2/1$ and $3/2$ Neoclassical Tearing Modes (NTMs).

In these scenarios, the challenge is also to deal with peeling-ballooning instabilities called Edge Localized Modes (ELMs) which are characterized by the quasi-periodic relaxation of the pressure pedestal profile which results in the expelling of particles and energy from the bulk plasma to the edge. This particular scenario triggers so-called "type-III" ELMs which are more frequent and have a lower deposited power on the PFCs than "type-I" ELMs. This is done by injecting edge impurities to change the pedestal profile.

Even within these limits, events like radiation instabilities at the edge can provoke a disruption (see Figure 2.10 and associated tables). They should be detected and handled.

Event handling Various methods have recently been developed to mitigate pre-disruptive events like Neoclassical Tearing modes (NTM) and internal kink modes (see section 2.2). On several machines, real-time control of NTMs has been demonstrated using Electron Cyclotron Current Drive (ECCD) and Electron Cyclotron Resonance Heating (ECRH) to change the current profile at the resonant surfaces $q = 2/1$ and $q = 3/2$ and mitigate $2/1$ and $3/2$ NTMs^m. Modeling of the NTM stabilization by ECCD has also been done in [Fevrier, Maget, et al. 2015]. In tokamaks, sawtooth oscillations (successive crashes of an internal kink mode) can also destabilize NTMs and lead to a disruption. Sawtooth control is currently studied in several devices and important progress has been madeⁿ. Control of NTMs has also been studied in DIII-D^o with the use of ECCD and Resonant Magnetic Perturbations (RMPs).

All these methods of avoidance need a robust plasma control system which is able to adapt the scenario in case of a plasma instability but also in case of the failure of a coil or of a heating system. Active research is on-going to build a fast and reliable system for ITER^p.

2.3.2 Disruption prediction and mitigation

Methods of disruption avoidance are sometimes not sufficient to prevent the plasma from disrupting. Thus, a system of mitigation of disruptions is needed. The aim is to trigger a disruption which is harmless for the tokamak. Section 2.1.2 presented the three main deleterious consequences of "uncontrolled" disruptions and their effects on the device. The "controlled" disruption should mitigate as much as possible these three phenomena

^mZohm, Gantenbein, et al. 2007; Felici, Goodman, et al. 2012.

ⁿFelici, Goodman, et al. 2012; Nowak, Buratti, et al. 2014; Chapman 2011.

^oVolpe, M. E. Austin, et al. 2009.

^pSnipes, Gribov, and Winter 2010.

at the same time. To do that, we must predict the occurrence of disruptions and be able to react on time.

Disruption prediction As disruptions are fast and violent events, it is a challenge to detect them and to act fast enough. As we saw in section 2.2 multiple causes can trigger a disruption, and a unique detector is often not enough to detect all of them. The easiest way is to define thresholds on specific measurements, for example the Locked-Mode (LM) signal in JET. Above a certain value the control system automatically switches to a scenario extinguishing the plasma. The difficulty is then to define appropriate thresholds and control parameters to both detect most disruptions and avoid false alarms. The physical phenomena leading to disruptions being very complex and non-linear, simple models have been devised so far. Recent progress are made due to machine learning techniques. Real time disruption predictors have been trained on several tokamaks, like JET^q, using neural networks and show promising results. However, they must be trained to be efficient and will probably not be available for the first day of ITER operation. More complex methods have also been studied^r, with some success.

As soon as they are predicted, disruptions should be mitigated. We will now present the objectives of mitigation for ITER and the two methods of mitigation currently planned. Then, chapter 3 will review the current status of research on the massive gas injection method.

Objectives of mitigation for ITER ITER load mitigation will consist of a highly reliable disruption prediction, active and passive schemes for disruption avoidance and a disruption mitigation system reducing thermal and electromagnetic loads. The latter is essential to avoid the melting of ITER full-W divertor and Be first wall. Table 2.3 gives the expected impact of disruptions in ITER and the tolerable values for each effect, and Figure 2.12 presents the resulting ITER operational space that requires disruption mitigation. The green area indicates the parameters for which unmitigated disruptions are expected to stay within the no-damage limit. This limit is given by estimations of heat and electromagnetic loads on the divertor during the TQ and on the first wall during the CQ. This sketch does not take into account runaway electron beams which can be generated during the CQ. Note that when the thermal energy of the plasma is increased, the mitigation efficiency should increase as well. To achieve this, the ITER Disruption

	Heat loads (in $MJ \cdot m^{-2} \cdot s^{-1/2}$)	RE beams	Mech. loads
Expected in ITER	450	$I_{RE} = 10$ MA	10
Tolerable value	40	$I_{RE} = 2$ MA	1

Table 2.3: Objectives of mitigation for ITER

Mitigation System (DMS) will massively inject impurities. The current design of the

^qRattá, Vega, et al. 2010.

^rMurari, Vega, et al. 2009.

ITER DMS is a hybrid system using Massive Gas Injection (MGI) and Shattered Pellet Injection (SPI), methods which have demonstrated their efficiency on current tokamaks. Three upper port plugs and one equatorial plug are allocated in ITER for thermal and electromagnetic load mitigation, as well as the mitigation or suppression of the RE beams. The amount of injected impurities will be limited by the capability of ITER's cryo-pumps ($8 \text{ k} \cdot \text{Pa} \cdot \text{m}^3$ for thermal load mitigation for example). Another important parameter for the ITER DMS is the time delay between the activation of the system of mitigation and the initiation of the mitigated TQ. This so-called "reaction time" should be as short as possible. The aim of the ITER DMS is to reduce heat loads by dissipating most of the

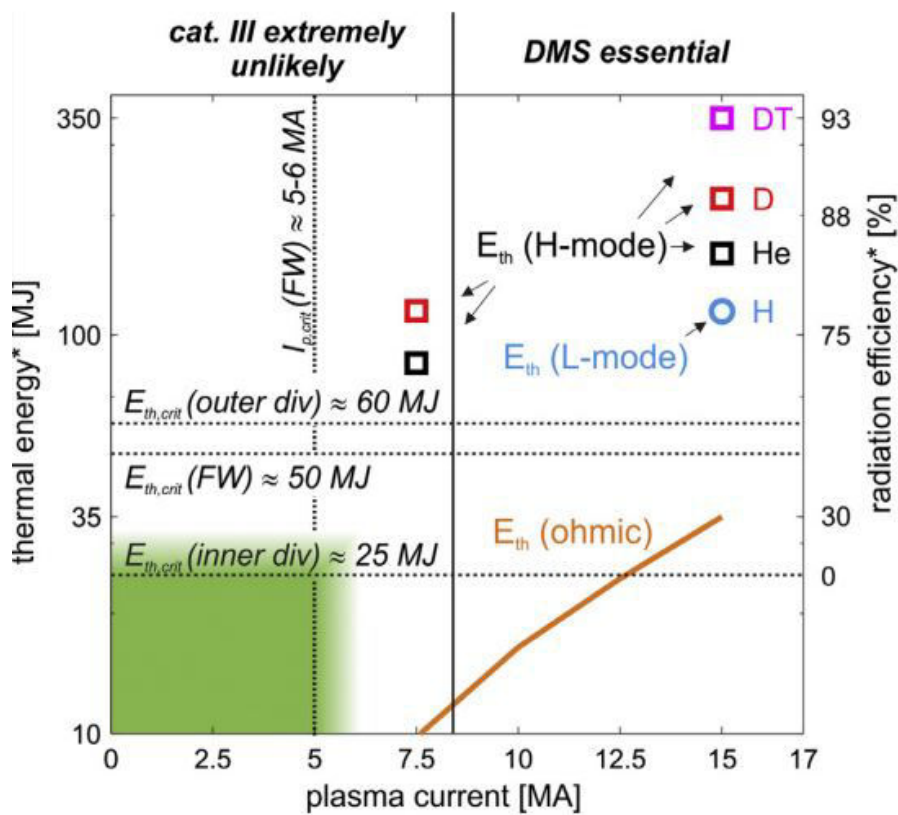


Figure 2.12: *ITER operational space that requires disruption mitigation, based on estimations of heat and electro-magnetic loads limits, Figure from [Lehnen, H R Koslowski, et al. 2014]. The green area is the area where the disruption mitigation system is not mandatory.*

thermal energy by radiation, to increase the plasma density to prevent the formation of RE beams, and to control the duration of the CQ to reduce electromagnetic loads.

Pellets One of the two mitigation methods for ITER is the injection of pellets^s. These pellets are gas-accelerated by room-temperature low-Z gas and can reach velocities of 300-600 m/s. Pellets penetrate into the plasma farther than gas jets (like MGI) and the impurities are deposited more suddenly. It means that the assimilation of impurities can be larger than with MGI but also that it could result in highly peaked radiated heat loads.

^sCommaux, L. Baylor, et al. 2010; E. Hollmann, M. Austin, et al. 2013.

Moreover, they can damage wall tiles if they are not fully ablated during their transit across the plasma, which may happen, for example, if they arrive too late or if they are not ablated enough by the cold CQ plasma. The Shattered Pellet Injection (SPI) solves this problem by breaking the pellets into shards before they enter the plasma. Different methods to shatter the pellets have been studied and the simple bending of the injection tube seems to be a very efficient method (see Figure 2.13). The fact that the pellets are shattered prevents wall tiles damage and also increases the impurity ablation surface and therefore reduces the subsequent assimilation time. Controlling the composition of the shattered pellet is challenging and active research is on-going to optimise the system. Next experimental campaigns on the DIII-D tokamak will mostly focus on this method of mitigation^t. The main flaw of the pellet injection is that it can generate much more

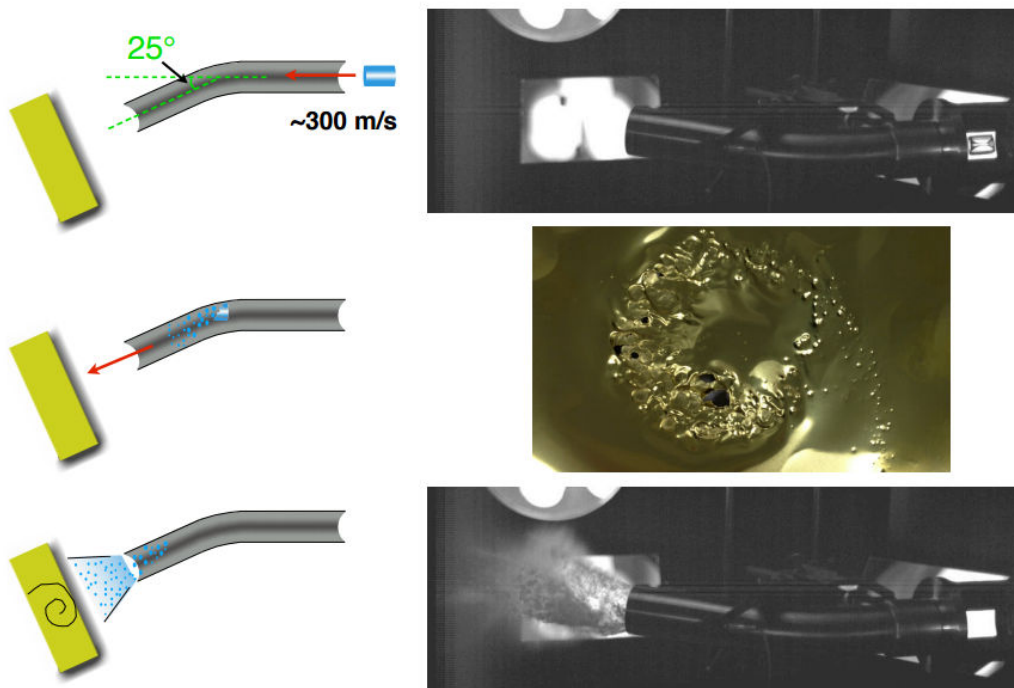


Figure 2.13: Simple breaker tube with single bend proved effective to shattered large pellets on DIII-D, Figure from [Combs and L. R. Baylor 2013]

runaway electrons than MGI.

Massive Gas Injection The principle of massive gas injection is described by its own name. One massively injects neutral gas at the plasma edge. The number of particles injected can be 10 – 1000 times larger than the initial plasma content. Different injection methods have been studied^u but most MGI experiments have been done with fast valves. These valves typically open in $\simeq 1\text{ms}$ and the gas contained in a pre-filled reservoir (at up to 50 bars of gas pressure) is emptied directly at the plasma edge (in ASDEX Upgrade

^tCombs and L. R. Baylor 2013.

^uSaint-Laurent, Martin, et al. 2014.

for example) or in a vacuum tube whose length limits the reaction time of the MGI (time between the activation of the DMS and the TQ). The technical drawing of the JET DMVs can be seen on Figure 2.14 and 2.15.

The first objective of massive gas injection is to reduce heat loads by dissipating most of the thermal energy by radiation. The radiated energy will be dissipated homogeneously on all the vacuum vessel area, instead of being dissipated on a smaller part of the wall. This is done by injecting noble gases like Argon (Ar) or Neon (Ne). MGI shutdown timescales depend on many parameters within each tokamak including gas species, plasma thermal energy, q -profile, and the length of the vacuum tube. However, several crucial questions are still unresolved and the next chapter will discuss them while reviewing the current status of research on this method of mitigation.

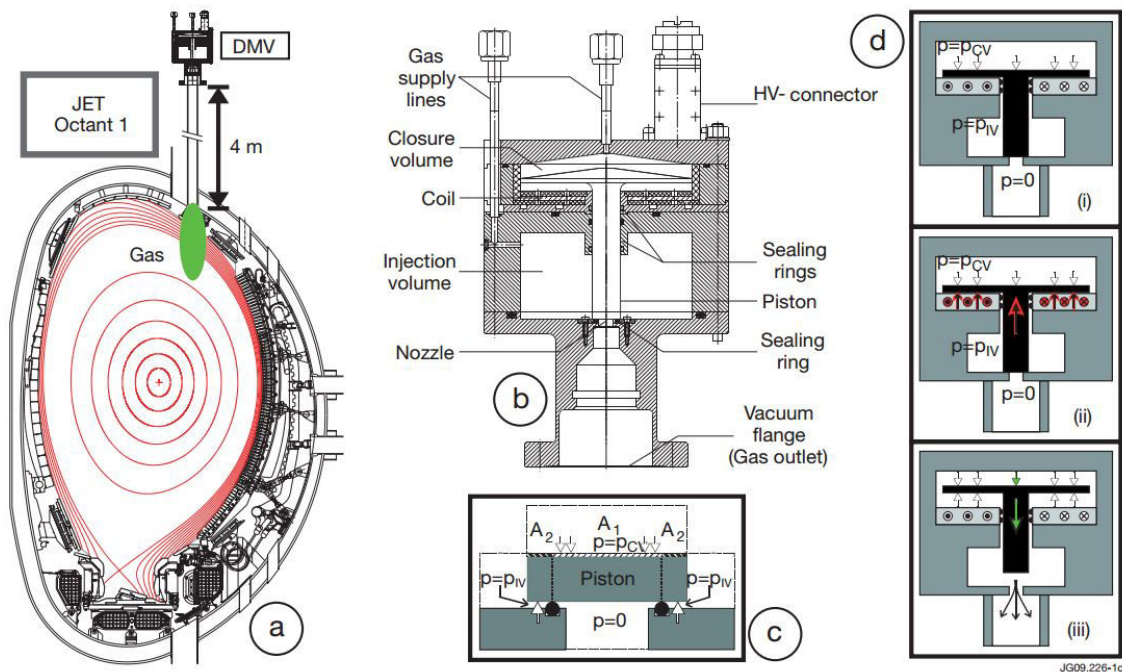


Figure 2.14: (a) Poloidal cut of JET. The DMV-1 position on top is indicated. (b) Technical drawing of the DMV-1. (c) Illustration of the variable force on the piston. (d) Valve operation principle. (i) Initial position sealed tightly by p_{CV} . (ii) Transient current induces eddy currents to lift the piston. (iii) Gas flows through the nozzle. The pressure p_{CV} forces the piston to close (green arrow). Figure from [U. Kruezi 2009]

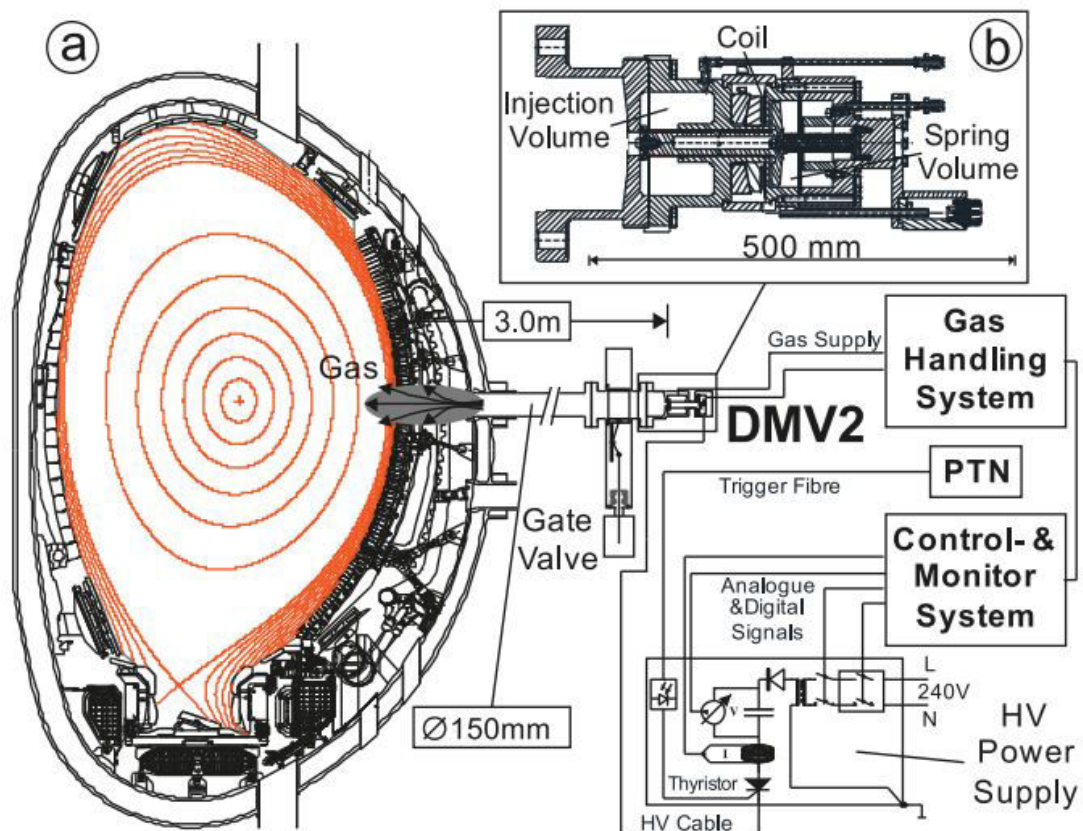


Figure 2.15: (a) Poloidal cross-section of the JET Torus showing the scheme of the new DMS. The Pulse Termination System (PTN) triggers the MGI via fibre (discharging the High Voltage (HV) Power Supply Unit (PSU)). (b) Cut through the new DMV (DMV2). Figure from [Jachmich, Uron Kruezi, et al. 2015]

3

Review of knowledge on massive gas injection

The principle of massive gas injection is to trigger a "controlled" disruption. It means a disruption which effects do not damage the tokamak walls and structure. Section 2.1.2 presented the three main deleterious consequences of an "uncontrolled" disruption and its effects on the tokamak. Most tokamaks have already done experiments on massive gas injection during the past fifteen years. JT-60U, ASDEX Upgrade, Tore Supra, DIII-D, JET, Alcator C-Mod, TEXTOR have all done dedicated campaigns. Moreover, a broad modeling effort on disruptions started a decade ago. This section will focus on the principle of disruption mitigation by massive gas injection and how large heat loads, mechanical loads and runaway electrons beams can be mitigated. The emphasis will be put on recent experimental and numerical results and remaining open questions to solve in view of designing ITER disruption mitigation system (ITER DMS).

3.1 Thermal loads mitigation

Heat loads during a shutdown by massive gas injection come from a combination of conduction and radiation. To predict the heat loads for ITER a complex problem needs to be solved. These heat loads will indeed depend on the impurity deposition of the MGI, the neutral transport and the plasma response to the MGI. 2D simulations with the TOKES code predicted wall temperature close to the Be melting point in ITER^a, however neglecting the 3D dynamic of the MGI.

Experimentally, it has been observed in various devices than the injected impurities are stopped at the plasma edge of hot pre-TQ plasmas, around the $q = 2$ magnetic ratio-

^aLandman, Pestchanyi, et al. 2013.

nal surface^b and we will discuss the mechanisms which could explain this gas stopping in chapter 5.

As there is a need to radiate as much thermal energy as possible, experiments and simulations focused on the fraction of energy dissipated by radiation, or the radiation fraction f_{rad} , defined by the ratio of the energy dissipated by radiation over the total thermal energy of the plasma ($= E_{rad}/E_{th}$). Measuring this radiation fraction during the TQ requires fast time resolution and an accurate separation between the TQ and the CQ, which is often difficult to define experimentally. Toroidal radiation asymmetries can also affect the accuracy of the measured f_{rad} . Nevertheless, most tokamaks report being able to radiate more than 90% of the initial thermal energy (see Figure 3.1). In order to achieve

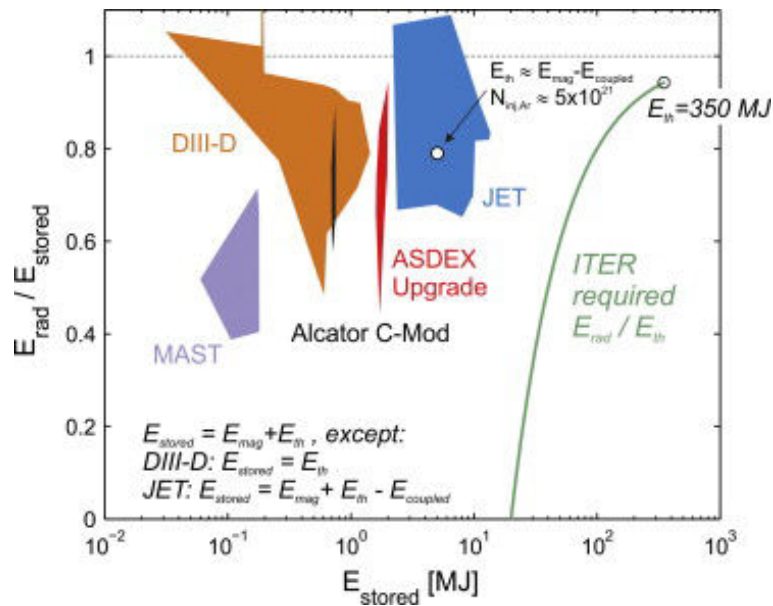


Figure 3.1: Radiation efficiency during MGI using high-Z noble gases (Ne, Ar) and mixtures of these with D_2 and He. Figure from [Lehnen, H R Koslowski, et al. 2014]

that, small quantities of high-Z impurities (at least 1%) are needed to avoid significant divertor heat loads during the TQ.

However, for high thermal energy fraction the radiation efficiency saturates at 80% on JET, despite further increase of the number of Ar particles injected. In ITER, this radiation efficiency should be higher than $\simeq 95\%$ to avoid divertor melting during ITER TQ (recall Figure 2.12). This number depends on the wetted area of the conducted heat loads which is not well-known. Local radiation peaking is also a concern for ITER as it can result in a localised melting of the wall. In several devices, radiation peaking during the pre-TQ have been reduced with the use of multiple injectors. However, the radiation distribution is expected to be driven by macro MHD instabilities during the TQ, as shown by NIMROD simulations^c and by DIII-D and JET experiments. The observed Toroidal Peaking Factor (TPF) is well below 2 in most devices but the influence of the MGI location and MHD rotation on the radiation peaking must be understood more deeply. Evidence

^bBucalossi, C. Reux, et al. 2011; C. Reux, Bucalossi, et al. 2010.

^cIzzo 2013.

for significant conducted heat loads during the CQ has also been observed in MAST^d and should be studied in future simulations and experiments.

3.2 Mitigation of runaway electron beams

Runaway electrons during spontaneous disruptions were regularly observed with the JET Carbon wall and in many devices. However, unmitigated disruptions with the ITER-like wall tend to produce almost no runaway electrons^e. This lower amount of RE is partly due to the slower current quenches but also to a different temperature of the post-TQ background plasma.

However, to study the generation of runaway electrons and to find ways to avoid them, we need a reproducible scenario which generates runaway beams. In JET, it has been demonstrated that even with the ILW^f, one can generate REs with the use of Argon MGI under specific conditions. Pure Argon MGI accelerates the CQ and thus increases the accelerating electric field generating runaways. Mixing Argon with Deuterium increases the electron density of the plasma due to the good mixing efficiency of deuterium, thus reducing the amount of REs. The runaway existence domain was thus mapped in JET using different D_2+Ar mixtures in various pressures, different toroidal fields, plasma pre-disruption densities and plasma shapes (see Figure 3.2). Understanding the runaway formation and its various dependencies is crucial in view of designing disruption mitigation strategies. Large experimental and modeling efforts (particularly with JOREK) are currently ongoing to find a satisfactory scenario to mitigate the formation of RE beams. The level of magnetic fluctuations and the plasma shape have been found to have an important effect on the runaway generation. The impact of magnetic fluctuations have been studied experimentally and with modeling and show a threshold above which runaways seem to be unconfined before becoming dangerous for the device (see [Zeng, H. R. Koslowski, et al. 2013; C. Reux and al. 2015] and Figure 3.3). Starting with these reproducible scenarios (Pure Argon MGI with different pressures in the DMV-1) which lead to 0.7 – 1.0 MA runaway beams lasting between 30 and 100 ms, recent experiments on JET have demonstrated the efficiency of a second MGI which prevents the formation of the beam if the DMV-2 is fired before the TQ triggered by the first injection. If it is fired after the TQ, the second injection has no effect on the runaway beam and the mitigation is completely inefficient^g. If fired before the TQ, the second injection can prevent the RE beam from being generated, as can be seen on Figure 3.4. This is presumably due to the different properties of the plasma background (post first MGI) in JET compared to other experiments (DIII-D, ASDEX Upgrade) in which a second MGI was able to partly mitigate the RE beam even when firing it after the TQ. Future experimental campaigns and modeling with various codes such as the ones presented in this thesis will try to understand this phenomenon.

^dThornton, Gibson, et al. 2012.

^eVries, G Arnoux, et al. 2012.

^fC. Reux and al. 2015.

^gC. Reux and al. 2015.

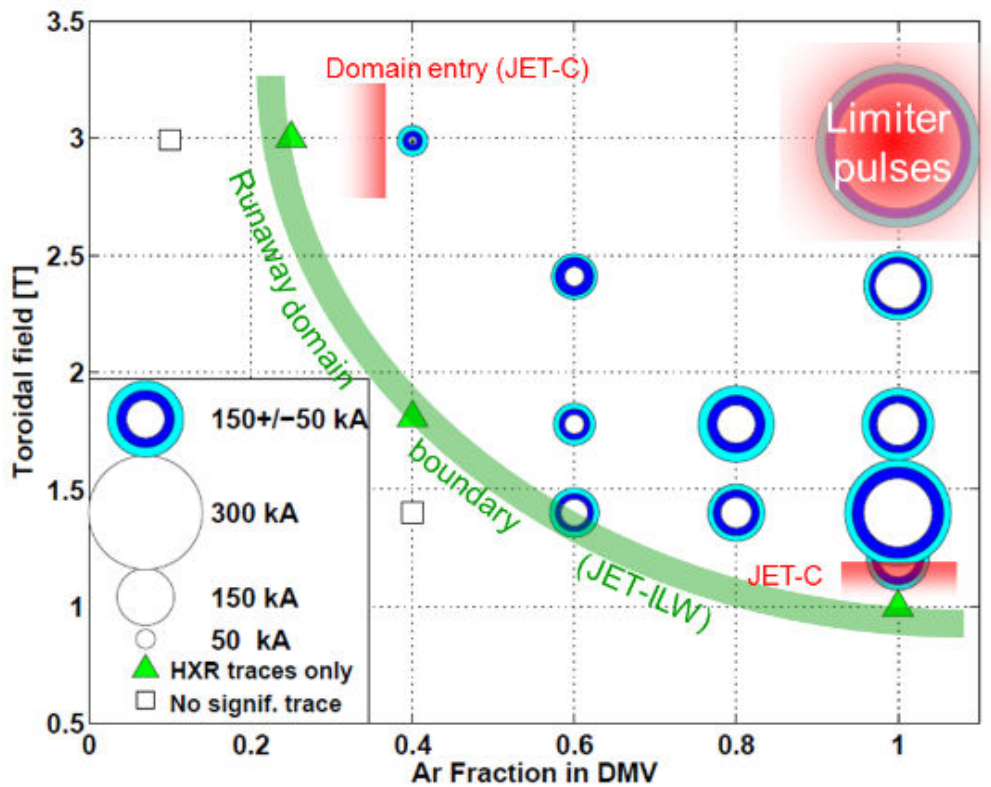


Figure 3.2: Runaway electron existence domain map as a function of toroidal field and argon fraction in the disruption mitigation valve. The domain entry points/boundaries is given for JET-C and JET-ILW. Circle size indicates the maximum runaway current reached during the disruption. Figure from [C. Reux and al. 2015]

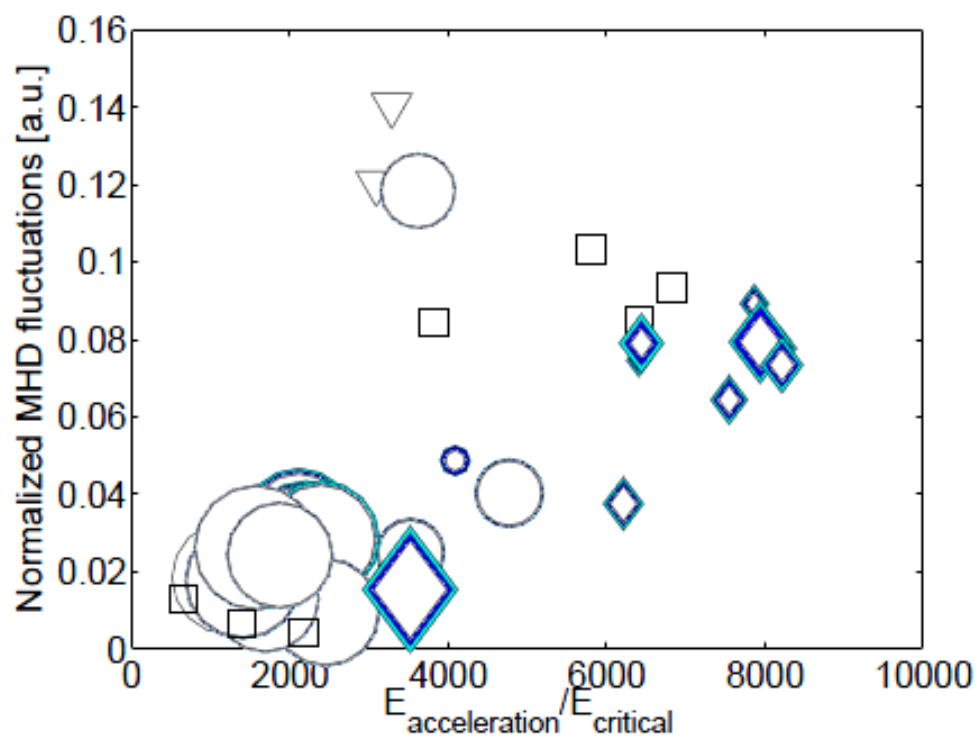


Figure 3.3: Runaway electron existence domain map as a function of normalized magnetic fluctuations and ratio of accelerating electric field over critical electric field. Marker size indicates the magnitude of the runaway current. Figure from [C. Reux and al. 2015]

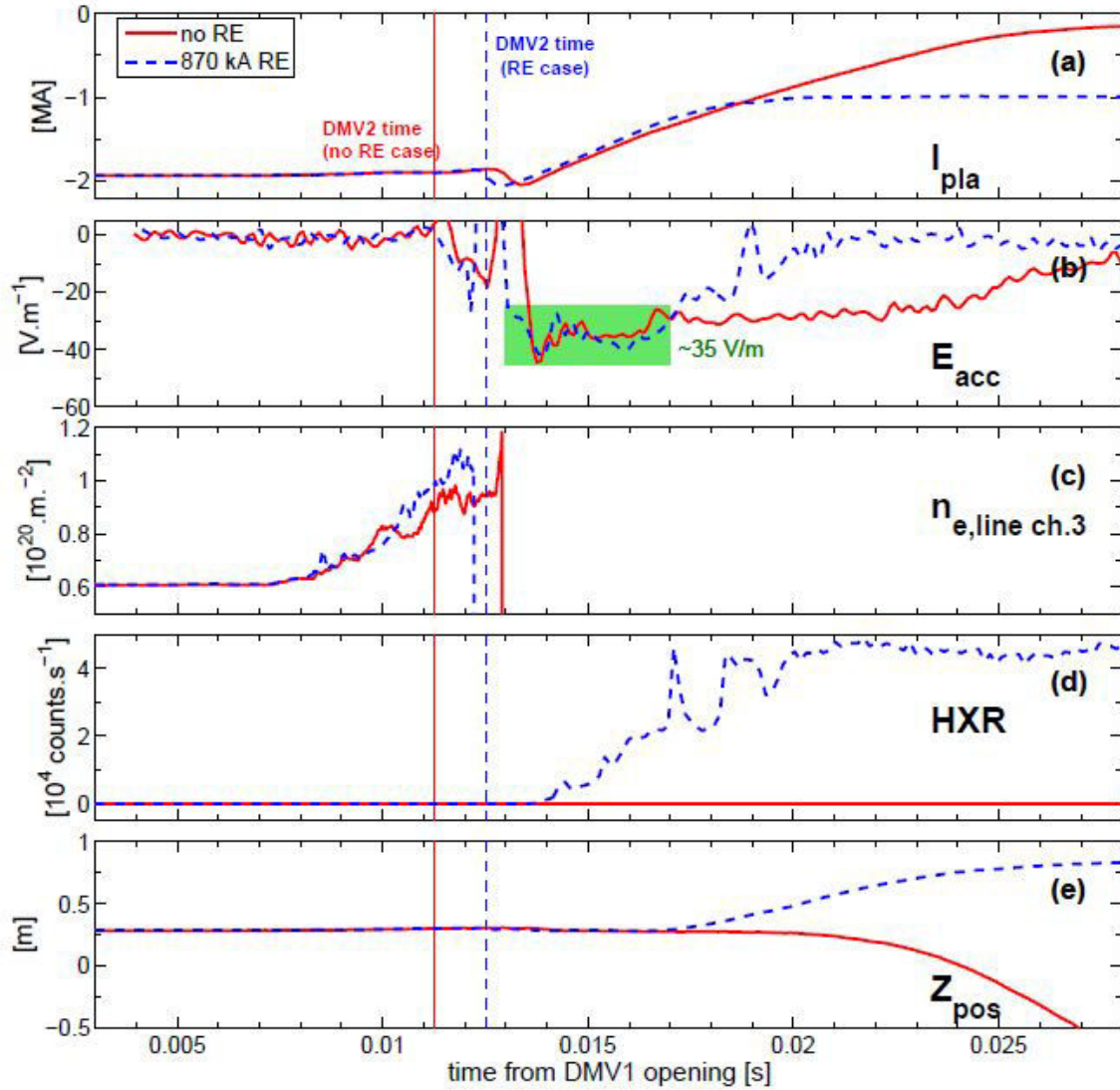


Figure 3.4: Runaway beam early mitigation. Runaway current as a function of DMV-2 firing time with respect to the thermal quench of the DMV-1-only disruption. (a) Plasma current (b) Accelerating electric field (c) line-integrated density, chord 3. (d) Hard X-ray total count rate (e) Current centroid vertical position. Figure from [C. Reux and al. 2015]

3.3 Current quench duration control

The DMS should not increase vessel forces over those of an unmitigated disruption, which should be inside the engineering margin on ITER. As sketched on Figure 3.5, CQ times should be shorter than 150 ms to avoid huge forces associated to halo currents and longer than 50 ms to avoid high induced currents and associated eddy current forces on blanket modules and the tokamak structure. Recent experiments on JET with the new ITER-like wall show that a sufficient margin is kept (see Figure 3.6). Halo current rotation

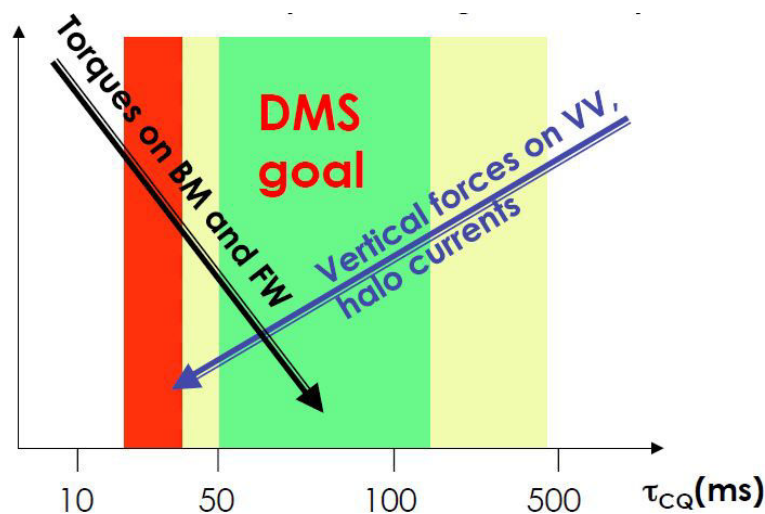


Figure 3.5: Optimum current quench duration to limit both halo and eddy currents

have been observed on DIII-D^h, ASDEX Upgrade or JETⁱ and might be a concern if this rotation induces large asymmetries in the halo current force and if this force rotates at a frequency driving a vacuum vessel mode. Modeling efforts are ongoing to try to understand the physics of halo current diffusion and rotation with various codes including JOREK^j, DINA^k and TSC.

Experimentally, disruptions triggered by MGI have 2 times lower halo currents than unmitigated disruptions^l. Recent results on JET^m with the ITER-like wall are promising because they suggest a long CQ duration (above 100 ms) for unmitigated disruptions in ITER, meaning that it will not be difficult to get a mitigated CQ duration in the 50 – 150 ms range. In carbon machines, the CQ is usually much shorter due to the large amount of carbon impurities released from the walls during the TQ. The choice of a full-W divertor for ITER will thus help keeping a sufficient margin and increasing the controlability of the mitigated CQ duration.

As presented in this chapter, open questions still remain. The following chapter will

^hEvans, A. Kellman, et al. 1997.

ⁱPautasso, Zhang, et al. 2011; Riccardo, G Arnoux, et al. 2010.

^jHoelzl, G. T. A. Huijsmans, et al. n.d.

^kMiyamoto, Isayama, et al. 2014.

^lLehnen, Alonso, et al. 2011.

^mVries, G Arnoux, et al. 2012.

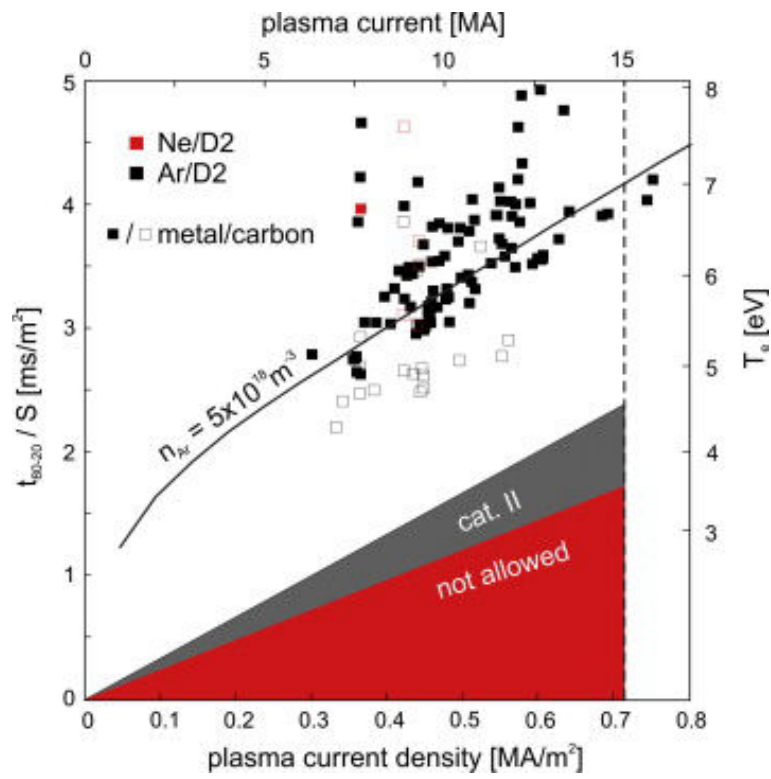


Figure 3.6: Normalised linear current decay time ($S =$ plasma cross-section area) in JET during injection of Ne and Ar mixed with 90% D_2 .

present the theoretical framework used to study disruptions and the numerical tools used in this thesis.

4

MGI triggered disruptions modeling: fundamentals and simulation tools

Contents

1.1	The challenge of controlling nuclear fusion	1
1.1.1	The stakes	2
1.1.2	The principle	2
1.2	Magnetic confinement with the tokamak concept	5
1.2.1	Magnetic configuration	6
1.2.2	Coordinate systems	6
1.2.3	Plasma Facing Components, the divertor configuration and vertical stability	8
1.2.4	JET and ITER	8
1.3	Outline of the thesis	13

4.1 Magnetohydrodynamics

To study disruptions, we will adopt a fluid framework known as magnetohydrodynamics (MHD). In this chapter, the fluid equations are derived from the kinetic description of the plasma. We will briefly sketch the origin of the kinetic formalism, then describe how the fluid equations are derived. We will derive the MHD equations used in the 3D code JOREK. In the process, we will also derive a 1D model for the neutral gas penetration

into the plasma which will be used in the code IMAGINE. Finally, we will present the specificities of the two codes developed and used in this thesis.

4.1.1 From kinetic to fluid description^a

We consider a population of N particles of the species s , with mass m_s and charge e_s , located at $\mathbf{x}_i(t)$ and with a velocity $\mathbf{u}_i(t)$. This population is described by its distribution function $F_s(\mathbf{x}, \mathbf{u}, t)$. The exact distribution function is a sum of Dirac functions of each particle:

$$F_s(\mathbf{x}, \mathbf{u}, t) = \sum_{i=1}^N \delta(\mathbf{x} - \mathbf{x}_i(t)) \delta(\mathbf{u} - \mathbf{u}_i(t)) \quad (4.1)$$

The conservation of particles and momentum in the phase space is simply expressed with the fundamental equation:

$$\frac{dF_s}{dt} = 0 \quad (4.2)$$

where $d/dt = \partial/\partial t + \mathbf{u} \cdot \nabla + \mathbf{a} \cdot \partial/\partial \mathbf{u}$ with \mathbf{u} the velocity and \mathbf{a} the acceleration. If only electromagnetic forces are considered and if we choose to work with an average distribution function $f_s = \langle F_s \rangle$ we obtain the following equation, called the kinetic equation:

$$\frac{\partial f_s}{\partial t} + \mathbf{u} \cdot \nabla f_s + \frac{e_s}{m_s} (\mathbf{E} + \mathbf{u} \times \mathbf{B}) \cdot \frac{\partial f_s}{\partial \mathbf{u}} = C_s(f_s) \quad (4.3)$$

If the collision operator $C_s(f_s)$ is neglected, we get the Vlasov equation:

$$\frac{\partial f_s}{\partial t} + \mathbf{u} \cdot \nabla f_s + \frac{e_s}{m_s} (\mathbf{E} + \mathbf{u} \times \mathbf{B}) \cdot \frac{\partial f_s}{\partial \mathbf{u}} = 0 \quad (4.4)$$

In plasmas, this 6-dimensional equation is coupled to the Maxwell equations describing the evolution of the electric and magnetic fields:

$$\nabla \cdot \mathbf{E} = \frac{\sigma}{\varepsilon_0} \quad (4.5)$$

$$\nabla \cdot \mathbf{B} = 0 \quad (4.6)$$

$$\nabla \times \mathbf{E} = -\frac{\partial \mathbf{B}}{\partial t} \quad (4.7)$$

$$\nabla \times \mathbf{B} = \mu_0 \mathbf{J} + \frac{1}{c^2} \frac{\partial \mathbf{E}}{\partial t} \simeq \mu_0 \mathbf{J} \quad (4.8)$$

where ε_0 is the vacuum permittivity and μ_0 the magnetic permeability, σ and \mathbf{J} are the charge and current densities, and c is the speed of light.

Solving these coupled equations is still very challenging and expensive in terms of computational time. It is usually done to study small-scale phenomena like plasma turbulence.

^aHazeltine and Meiss 2013.

For larger space and time scale phenomena such as disruptions, it is currently unrealistic to numerically solve these equations. We rather use a fluid approach.

Fluid equations are obtained by taking moments of the Vlasov equation, i.e. multiplying it by powers of \mathbf{u} and integrating over the whole velocity space.

We define the density n_s , the velocity \mathbf{v}_s and the pressure tensor $\bar{\mathbf{p}}_s$ by:

$$n_s = \int f_s d^3\mathbf{u} \quad (4.9)$$

$$n_s \mathbf{v}_s = \int \mathbf{u} f_s d^3\mathbf{u} \quad (4.10)$$

$$\bar{\mathbf{p}}_s = m_s \int \mathbf{u}' \mathbf{u}' f_s d^3\mathbf{u} \text{ with } \mathbf{u}' = \mathbf{u} - \mathbf{v}_s \quad (4.11)$$

The pressure tensor is decomposed into the scalar pressure p_s and the stress tensor $\bar{\boldsymbol{\pi}}_s$: $\bar{\mathbf{p}}_s = p_s \bar{\mathbf{I}} + \bar{\boldsymbol{\pi}}_s$ where $\bar{\mathbf{I}}$ is the identity tensor. The stress tensor contains the anisotropic and off-diagonal terms of the pressure tensor. We define the mass density of a species $\rho_s = m_s n_s$ and the fluid mass density $\rho = m_i n_i + m_e n_e$.

Integration of the Vlasov equation over the velocity space yields the continuity equation:

$$\frac{\partial n_s}{\partial t} + \nabla \cdot (n_s \mathbf{v}_s) = 0 \quad (4.12)$$

Multiplying the Vlasov equation by \mathbf{u} and integrating yields the momentum equation:

$$\rho_s \left(\frac{\partial \mathbf{v}_s}{\partial t} + \mathbf{v}_s \cdot \nabla \mathbf{v}_s \right) = n_s e_s (\mathbf{E} + \mathbf{v}_s \times \mathbf{B}) - \nabla p_s - \nabla \cdot \bar{\boldsymbol{\pi}}_s \quad (4.13)$$

At the following order we obtain the pressure equation:

$$\frac{\partial p_s}{\partial t} + \mathbf{v}_s \cdot \nabla p_s + \gamma p_s \nabla \cdot \mathbf{v}_s + (\gamma - 1) [\nabla \cdot \mathbf{q}_s + \bar{\boldsymbol{\pi}}_s : \nabla \mathbf{v}_s] = 0 \quad (4.14)$$

where γ is the ratio of the specific heats. \mathbf{q}_s is the microscopic heat flux and we would need higher order moments to calculate it.

4.1.2 MHD equations

We now consider the plasma as a single fluid of mass density ρ , momentum density $\rho \mathbf{v} = \rho_e \mathbf{v}_e + \rho_i \mathbf{v}_i$ and pressure $p = p_e + p_i$. We assume the quasi-neutrality of the plasma, which means that the electron and ions densities are locally equal:

$$n = n_e = n_i \quad (4.15)$$

This is true to a very good approximation if the system and the phenomena we are looking at both have a characteristic length larger than the Debye length ($\simeq 10^{-5}$ m, length above which charges are electrically screened).

By adding up the continuity equations 4.12 for each species we obtain the evolution equation for ρ :

$$\frac{\partial \rho}{\partial t} + \nabla \cdot (\rho \mathbf{v}) = 0 \quad (4.16)$$

Since $m_i/m_e \gg 1$, the electron inertia is neglected compared to the ion inertia. Thus $\rho \simeq \rho_i$ and $\rho \mathbf{v} \simeq \rho_i \mathbf{v}_i$. Using the quasi-neutrality and adding up the equations 4.13 we obtain the following ion momentum equation:

$$\rho \left(\frac{\partial \mathbf{v}}{\partial t} + \mathbf{v} \cdot \nabla \mathbf{v} \right) = \mathbf{J} \times \mathbf{B} - \nabla p \quad (4.17)$$

with $\mathbf{J} = n_e e (\mathbf{v}_i - \mathbf{v}_e)$. Finally, we also obtain the pressure equation:

$$\frac{\partial p}{\partial t} + \mathbf{v} \cdot \nabla p + \gamma p \nabla \cdot \mathbf{v} = 0 \quad (4.18)$$

These equations and the Maxwell equations form the standard ideal MHD system.

4.2 Gas-plasma interaction

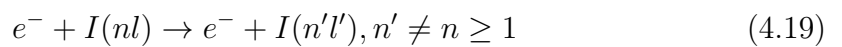
The equations presented above are valid for a closed system, i.e. a plasma without any additional sources of particles, heat or momentum. Moreover, they do not take into account neutral particles which are injected during a massive gas injection. To correctly model the impact of MGI on the plasma, we must treat the behaviour of impurities in a hot plasma, i.e. include atomic processes and transport of neutrals.

4.2.1 Atomic processes

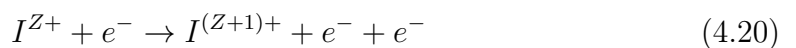
The charge-state distribution of an impurity depends on its temperature and the characteristics of the plasma in which this impurity is injected. It is governed by several atomic processes. Most atomic processes considered in this thesis are electron impact processes, i.e. the inelastic electron impact on an impurity I (in a quantum state characterized by principal and angular momentum quantum numbers n and l).

Many processes can occur in a plasma, but the probability of a reaction can change by orders of magnitude depending on the plasma temperature and density. Within the plasma parameter range considered in this thesis, the main processes are:

- Excitation: an electron excites an atom and transfers part of its energy to it.



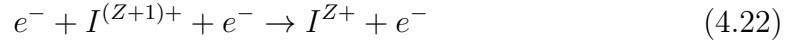
- Ionization: the collision of an ion with an electron releases another electron.



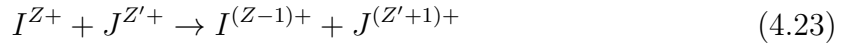
- Radiative recombination: an ion captures an electron and releases a photon.



- Three-body recombination: this process is inverse to electron-impact ionization and it is effective only at high plasma densities.



Ion impact processes can also be important, in particular at low temperature (in the eV region). An important heavy-particle collision process in low-temperature plasma is the charge-exchange (or charge transfer) reaction:



This reaction allows energy exchange between hot and cold particles at the plasma edge. All these processes are characterized by a reaction cross-section $\sigma(v)$ which defines the collision frequency associated to each process. This cross-section depends on the relative speed of the interacting particles and is usually averaged over a Maxwellian velocity distribution to give the reaction rate per time and volume units:

$$n_1 n_2 \langle \sigma(v) v \rangle \quad (4.24)$$

where n_1, n_2 are the densities of the reactants. The evolution of each species in the plasma can be calculated from these reaction rates.

Processes involving molecules such as D_2 -ions elastic collisions^b will be neglected in this thesis but could be studied in future work.

A plasma also emits radiation, which decreases its energy. Main radiative processes are the bremsstrahlung and the line radiation.

The bremsstrahlung radiation is emitted when a charged particle is accelerated (due to its interaction with other particles). In the following we will use the non-relativistic formula given in [J. Wesson 2004]:

$$P_{brem}[W \cdot m^{-3}] = \frac{Z_i^2 n_i [m^{-3}] n_e [m^{-3}]}{7.69 \times 10^{18}} T_e [eV]^{1/2} \quad (4.25)$$

where P_{brem} is the emission power density, Z_i is the atomic number of the plasma ions (or the effective atomic number in case of an impure plasma).

Line radiation is emitted by ions and atoms when an electron is moving from one orbital to another of lower energy. It is usually the case when an electron has excited an atom or an ion (see Eq.4.19). The emitted radiation has a discrete wavelength and this is thus used in plasma diagnostics to characterize the impurity content of plasmas.

The power radiated by line radiation depends on the impurity density for each charge-state $n_{i,imp}$, the electron density n_e in the plasma and a radiation rate coefficient $L_{i,lines}$ which

^bGuillemaut, Pitts, et al. 2014.

depends on the charge-state i of the impurity and on the plasma temperature and density.

$$P_{lines} = \sum_{i=0}^N n_e n_{i,imp} L_{i,lines}(n_e, T_e) \quad (4.26)$$

Of course, the reaction rates L_{lines} depend on the impurity species (for example, heavier ones like Tungsten will radiate more than lighter ones such as Carbon or Oxygen).

The ADAS database^c will be used in this thesis to compute the radiation rate coefficients and the reaction cross-sections of these processes (except where otherwise specified).

4.2.2 Transport of neutrals

Mechanisms governing the transport of neutrals during a MGI are still unclear. One of the objectives of chapter 5 will be to improve our understanding of these processes.

If we start from first principles, i.e. Eq. 4.12, 4.13, the transport of neutrals is purely convective^d and the equations for the neutral density n_0 and velocity V_0 are:

$$\frac{\partial n_0}{\partial t} = -\nabla \cdot (n_0 V_0) + S_{n_0} \quad (4.27)$$

$$m_0 n_0 \frac{dV_0}{dt} = -\nabla P_0 + f_{\rightarrow n} \quad (4.28)$$

where P_0 is the neutral pressure, $f_{\rightarrow n}$ is the friction on neutrals associated to atomic processes, and S_{n_0} is the sources and sinks of neutrals due to ionization and recombination processes.

$f_{\rightarrow n}$ is proportional to n_0 and to the relative speed of the reactants (one being the neutral and the other being, for example, an impurity ion).

$$f_{\rightarrow n} = -\alpha_f n_0 (V_0 - V_k) \quad (4.29)$$

However, in most codes a diffusive transport of neutrals is often assumed. Such a model can be derived using strong assumptions on the neutral velocity and on the velocity of the impurity ions. Indeed, if we assume that $V_k = 0$ and $d_t V_0 = 0$, Eq. 4.28 implies that:

$$\nabla P_0 = -\alpha_f n_0 V_0 \quad (4.30)$$

with $\nabla P_0 = k_B \nabla (n_0 T_0)$ (T_0 in Kelvin). If we also assume that the temperature of neutrals is the same in the whole gas cloud, we obtain the following expression for V_0 :

$$V_0 = \frac{-k_B T_0 \nabla n_0}{\alpha_f n_0} \quad (4.31)$$

^cSummers n.d.

^dMeier and Shumlak 2012.

Replacing V_0 by its expression in Eq.4.27 implies:

$$\frac{\partial n_0}{\partial t} = -\nabla \cdot \left(\frac{k_B T_0}{\alpha_f} \nabla n_0 \right) + S_{n_0} \quad (4.32)$$

which is a diffusion equation for n_0 with a diffusion coefficient $D_n = k_B T_0 / \alpha_f$. Such a diffusive model is usually used for SOL parameters and intrinsic impurities coming from the tokamak walls (with $n_n \ll n$). An example of such a diffusion coefficient for neutrals can be found in [C Reux 2010], where D_n is linked to charge-exchange and ionization processes:

$$D_n = \frac{\lambda^2}{\tau} = \frac{3k_B T_i}{n_i (\langle \sigma v \rangle_{c.x.} + \langle \sigma v \rangle_{ion})} \quad (4.33)$$

Studies with codes such as SOLEDGE, EIRENE^e or TOKAM2D including such models for the transport of neutrals have been done and phenomena such as wall recycling, gas-puffing, divertor detachment or the impact of neutrals on turbulence can be simulated^f. However, no consensus has been reached yet for MGI where $n_n \geq n$ in most cases. In this case, the neutral gas cloud can have only a small fraction of ionized impurities in its core and most assumptions used to derive a diffusive model are not valid. Especially, MGI neutrals arrive at the plasma edge with a certain momentum which is much larger than for a gas puff. Assuming $dV_0/dt = 0$ has no justification a priori.

We will now present a new first-principle code devoted to this study.

4.3 The 1D first principle code IMAGINE

As just said, mechanisms describing the neutral gas propagation and its penetration into the plasma are still unclear. As these processes governs the cooling phase dynamics and duration, it is important to better understand them.

The first-principle 1D fluid code, IMAGINE, has been developed for this purpose.

4.3.1 Equations and assumptions

IMAGINE is a 1D radial code, in slab geometry, whose equations are thus averaged on flux surfaces. It includes a complete model of atomic physics with ADAS coefficients. Neutral transport is convective, in agreement with first principles. The equations for a deuterium MGI derive from Eqs. 4.12, 4.13, 4.14 with sources taking atomic processes into account. The stress tensors are neglected and the heat flux closure for the electrons is taken from Braginskii. We assume that $\nabla \cdot q_n = 0$. The equations which are solved by the code are:

$$\partial_t n_e = n_e n_0 I - n_e^2 R + \partial_r (D \partial_x n_e) \quad (4.34)$$

^eReiter and Baelmans 2005.

^fTamain, Tsitrone, et al. 2007; Tamain, Bonhomme, et al. 2013; Marandet, Tamain, et al. 2013.

$$\partial_t \left(\frac{3}{2} n_e T_e \right) = -n_e (n_0 I E_{ion} + n_0 L_{lines} + n_e R \frac{3}{2} T_e) - n_e^2 L_{brem+rec} + \partial_r (\chi n_e \partial_x T_e) \quad (4.35)$$

$$\partial_t \left(\frac{3}{2} n_e T_i \right) = \frac{3}{2} n_e (IP_0/e - n_e R T_i - \langle \sigma v \rangle_{cx} (n_0 T_i - P_0/e)) + \partial_r (\chi n_e \partial_x T_i) \quad (4.36)$$

$$\partial_t n_0 = -\partial_r (n_0 V_0) - n_e n_0 I + n_e^2 R \quad (4.37)$$

$$m_0 n_0 \partial_t V_0 = -m_0 n_0 V_0 \partial_r V_0 - \partial_r P_0 - m_0 (n_0 n_e \langle \sigma v \rangle_{cx} + n_e^2 R) V_0 \quad (4.38)$$

$$\partial_t P_0 = -V_0 \partial_r P_0 - \frac{5}{3} P_0 \partial_r V_0 - n_e I P_0 + n_e^2 R (e T_i + \frac{1}{3} m_0 V_0^2) + n_e \langle \sigma v \rangle_{cx} (e n_0 T_i - P_0 + \frac{1}{3} m_0 n_0 V_0^2) \quad (4.39)$$

Where n_e and T_e are the electron density and temperature (in eV) of the plasma, T_i is the ion temperature (in eV) of the plasma, n_0 is the neutral density, P_0 and V_0 are the pressure and radial velocity of the neutrals. $n_i (= n_e)$ is the plasma ion density and we do not distinguish ions from the initial plasma and impurity ions. γ depends on the injected gas. In the case of a monoatomic gas such as Argon $\gamma = \frac{5}{3}$ whereas $\gamma = \frac{7}{5}$ if the injected impurity is a diatomic gas such as D_2 . In the following we will neglect the bond-dissociation energy of D_2 molecules into D atoms and thus only evolve the neutral D density. Assuming that this energy is the same as for H_2 molecules, i.e. about 5 eV, this seems reasonable in the sense that it is smaller than the ionisation energy of two D atoms by a factor of about 5. The influence of molecular processes might still be studied in future work.

All other quantities are atomic physics parameters (ionization, recombination and radiation). Neutral transport is convective and a friction between neutrals and impurity ions due to charge-exchange is taken into account, as well as the energy transfer between ions and neutrals due to charge-exchange.

α_{fric} is a parameter introduced to test the influence of the friction term and should be equal to 0 or 1. $\langle \sigma v \rangle_{cx}$ is the reaction cross-section of the charge-exchange process. v_i is the thermal velocity of the plasma ions.

The code can also model an Argon MGI, following all ionization states (see [Fil, Nardon, et al. 2014]). The results presented in the next chapter are for pure deuterium MGI.

4.3.2 Simulation domain and numerical scheme

An original aspect of this code is that the simulated domain comprises not only the plasma but also the gas reservoir (see Figure 4.1). The vacuum injection tube which links the gas reservoir and the plasma edge is also included. We consider a slab geometry, with x the radial coordinate. $x = 0$ corresponds to the plasma center and $x = x_{max}$ corresponds

to the end of the reservoir. The plasma is between $x = 0$ and $x = a$, where a is the minor radius of the plasma. The vacuum tube is between $x = a$ and $x = a + L_{tube}$ where L_{tube} depends on the DMV we want to simulate. The reservoir is between $x = x_{max} - x_{res}$ and $x = x_{max}$ and is initially filled with a constant neutral density.

In terms of numerics, a MUSCL[§] scheme (for *Monotonic Upstream-Centered Scheme*

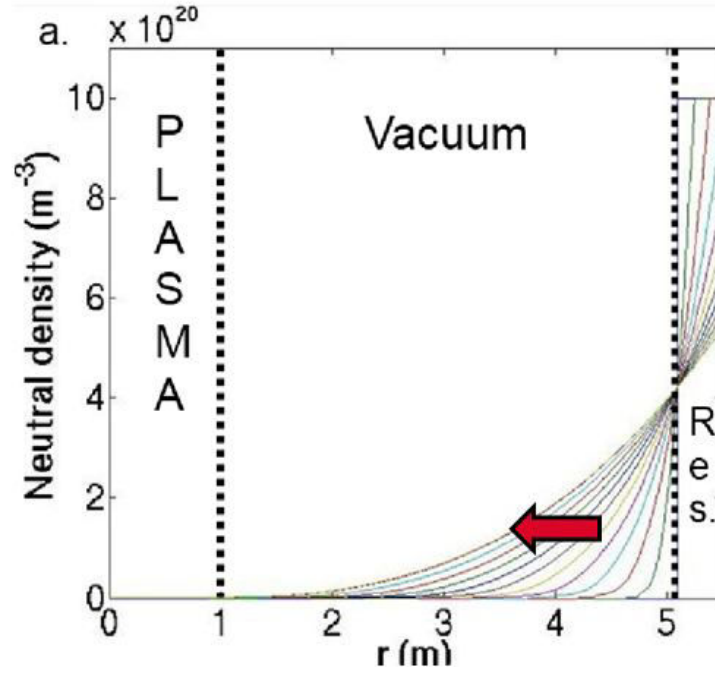


Figure 4.1: *IMAGINE* simulation domain, $r/r_{max} = 0$ correspond to the plasma center and $r/r_{max} = 1$ to the edge of the reservoir of neutrals

for Conservation Laws) is used to deal with shock waves. It is a finite volume method providing highly accurate numerical solutions even when the solution exhibits shocks, large gradients or discontinuities.

The principle of this numerical method is the following:

Let us consider the following simple 1D scalar system:

$$\partial_t u + \partial_x F(u) = 0 \quad (4.40)$$

Where u represents a state variable and F represents a flux variable. The domain is decomposed in $(x_1, \dots, x_i, \dots, x_N)$ grid elements and $u_i = u(x_i)$.

A basic scheme uses piecewise constant approximations for each cell, such as:

$$\frac{du_i}{dt} + \frac{1}{\Delta x_i} [F(u_i) - F(u_{i+1})] = 0 \quad (4.41)$$

[§]Leer 1976.

This scheme is unfortunately not able to handle shocks or sharp discontinuities. It is thus extended by using piecewise linear approximations of each cell, such as:

$$u(x) = u_i + \frac{(x - x_i)}{(x_{i+1} - x_i)} (u_{i+1} - u_i) \quad \forall x \in [x_i, x_{i+1}] \quad (4.42)$$

Evaluating fluxes at the cell edges we get the following semi-discrete scheme:

$$\frac{du_i}{dt} + \frac{1}{\Delta x_i} [F(u_{i+1/2}) - F(u_{i-1/2})] = 0 \quad (4.43)$$

where $u_{i+1/2}$ and $u_{i-1/2}$ are the piecewise approximate values of cell edge variables

$$\begin{aligned} u_{i+1/2} &= 0.5 (u_i + u_{i+1}) \\ u_{i-1/2} &= 0.5 (u_{i-1} + u_i) \end{aligned} \quad (4.44)$$

However, this scheme is not a "total variation diminishing" (TVD) scheme and spurious oscillations are observed at the discontinuities (particularly at the MGI reservoir exit). The MUSCL scheme extends this idea by using slope limited left and right extrapolated states.

$$\frac{du_i}{dt} + \frac{1}{\Delta x_i} [F_{i+1/2}^* - F_{i-1/2}^*] = 0 \quad (4.45)$$

where $F_{i+1/2}^*$ and $F_{i-1/2}^*$ are numerical fluxes which are nonlinear combinations of first and second-order approximations of the flux function. They are functions of $u_{i+1/2}^L, u_{i+1/2}^R, u_{i-1/2}^L$ and $u_{i-1/2}^R$, defined as:

$$\begin{aligned} u_{i+1/2}^L &= u_i + 0.5\phi(r_i)(u_i - u_{i-1}) \\ u_{i+1/2}^R &= u_{i+1} - 0.5\phi(r_i)(u_{i+1} - u_i) \\ u_{i-1/2}^L &= u_{i-1} + 0.5\phi(r_{i-1})(u_i - u_{i-1}) \\ u_{i-1/2}^R &= u_i - 0.5\phi(r_i)(u_{i+1} - u_i) \end{aligned} \quad (4.46)$$

with $r_i = \frac{u_i - u_{i-1}}{u_{i+1} - u_i}$

The function $\phi(r_i)$ is quite important and is called a flux limiter function (or slope limiter function). Its role is to limit the slope of the piecewise approximations, ensuring that the solution is TVD.

In IMAGINE, we use the ospre limiter function^h, defined as:

$$\phi_{op}(r) = \frac{1.5(r^2 + r)}{(r^2 + r + 1)}; \quad \lim_{r \rightarrow \infty} \phi_{op}(r) = 1.5 \quad (4.47)$$

^hSerrano, Climent, et al. 2013.

and the numerical fluxes are defined by the Kurganov and Tadmor central schemeⁱ.

$$\begin{aligned} F_{i-\frac{1}{2}}^* &= \frac{1}{2} \left\{ \left[F \left(u_{i-\frac{1}{2}}^R \right) + F \left(u_{i-\frac{1}{2}}^L \right) \right] - a_{i-\frac{1}{2}} \left[u_{i-\frac{1}{2}}^R - u_{i-\frac{1}{2}}^L \right] \right\} \\ F_{i+\frac{1}{2}}^* &= \frac{1}{2} \left\{ \left[F \left(u_{i+\frac{1}{2}}^R \right) + F \left(u_{i+\frac{1}{2}}^L \right) \right] - a_{i+\frac{1}{2}} \left[u_{i+\frac{1}{2}}^R - u_{i+\frac{1}{2}}^L \right] \right\} \end{aligned} \quad (4.48)$$

$a_{i\pm\frac{1}{2}}$ is the maximum absolute value of the eigenvalue of the Jacobian of $F(u(x, t))$ over cells $i, i \pm 1$. The calculation of this Jacobian for IMAGINE equations will be detailed the appendix.

4.3.3 Limits of the model

We work in slab geometry, which means that an axisymmetry is assumed for both toroidal and poloidal directions (symmetry around the magnetic axis and the torus axis). It implies that injected impurities are spread over the plasma surface, which results in a lower radiation. Indeed, line radiation is proportional to $n_0 n_e$ with $n_e \propto n_0$ as n_e increases due to ionization and thus $P_{rad} \propto n_0^2$. This also implies that the parallel dynamic of the gas cloud is supposed to be instantaneous. These are two limitations of the code which prevent us from studying radiation peaking or asymmetries at the plasma edge.

To be able to compare the simulations to the experiment, one must also ensure that both the number of particles and the gas flow at the reservoir exit in the simulations are compatible with the experiment. The method to define the input parameters will be described in section 5.2.

This code will be used to study MGI starting with the gas propagation from the reservoir to the plasma followed by the gas penetration into the plasma. The results of this study will be presented in chapter 5.

The IMAGINE code is useful to describe the MGI-plasma interaction at the very edge (typically between $r/a = 0.8$ and $r/a = 1$) but then a more complex model is needed. We will now present the second code used in this thesis, the 3D non-linear MHD code JOREK.

4.4 The 3D non-linear MHD code JOREK

JOREK is a non-linear MHD code in 3D toroidal geometry including the X-point and the Scrape-Off Layer (SOL) in the computational domain. In this thesis, we have developed and used the so-called "model 500" of JOREK, which is single-fluid large aspect ratio reduced MHD with an equation for neutral density and additional terms related to atomic physics in several equations.

In this section, JOREK equations and assumptions will be presented.

ⁱKurganov and Tadmor 2000.

4.4.1 Equilibrium: Grad-Shafranov equation

In MHD codes and particularly in JOREK, we first solve the Grad-Shafranov (GS) equation. Its numerical solution provides the equilibrium magnetic configuration (given by $\psi(R, Z)$) and the radial pressure profile p .

The magnetic field can indeed be expressed as:

$$\mathbf{B} = F(\psi)\nabla\varphi + \nabla\psi \times \nabla\varphi \quad (4.49)$$

where φ is the toroidal angle and ψ the poloidal flux defined in a point P by:

$$\psi(P) = \int \int_{\Sigma_P} \mathbf{B} \cdot d\Sigma_P \quad (4.50)$$

where Σ_P is the disk lying on P whose axis is the tokamak axis of symmetry.

The force balance equation can then be rewritten as an equation for ψ which leads to the GS equation:

$$\nabla \cdot \frac{1}{R_0^2} \nabla \psi = \frac{j_\varphi}{R_0} = -p'(\psi) - \frac{FF'(\psi)}{R_0^2} \quad (4.51)$$

where R_0 is the tokamak major radius, j_φ the toroidal current density and $p' = dp/d\psi$. In practice, one must provide the functions p' and FF' and solve for ψ . These functions are fitted on experimental measurements. The EFIT code (for Equilibrium Fitting) is an equilibrium code and is used to interpret and fit the experimental data. The EFIT profiles are not directly used since they do not take kinetic measurements into account in this particular shot. Instead, HRTS n_e and T_e measurements are used to compute the pressure profile, assuming $T_i = T_e$. Mapping this profile on the EFIT ψ and deriving with respect to ψ provides p' . The FF' profile is then adjusted so that the flux surface averaged toroidal current density profile $j_{mean}(\psi_n) = \langle j_\varphi/R \rangle / \langle 1/R \rangle$ (where ψ_n is the normalized EFIT ψ , equal to 0 on the magnetic axis and 1 at the last closed flux surface) remain close to the one provided by EFIT. For this purpose, the relationship between p' , FF' and j_{mean} provided by the flux surface averaged Grad-Shafranov equation is used.

Moreover, the EFIT poloidal flux ψ is also used as a boundary condition in JOREK.

4.4.2 JOREK equations

The reduced MHD model We want to reduce the computational time as much as possible by simplifying the resistive MHD model. To do this, MHD equations are reduced into a set of scalar equations inspired by the four-field model derived in [Strauss 1997]. In the reduced MHD model we assume that the toroidal field B_φ is constant in time and that the poloidal field B_p is smaller than the toroidal field, which leads to the following expression for \mathbf{B} :

$$\mathbf{B} = F_0 \nabla\varphi + \nabla\psi \times \nabla\varphi, \text{ with } \frac{B_p}{B_\varphi} = \frac{|\nabla\psi|}{F_0} \ll 1 \quad (4.52)$$

where $F_0 = R_0 B_{\varphi 0}$ is approximately constant. In this model, we also neglect the poloidal component of the potential vector ($\mathbf{B}_p = \nabla \times \mathbf{A}$), leading to:

$$\mathbf{A} = A_\varphi \mathbf{e}_\varphi = \frac{\psi}{R} \mathbf{e}_\varphi \quad (4.53)$$

Finally, the velocity \mathbf{v} is decomposed into its parallel (to the unperturbed magnetic field) and poloidal components, and the electron and ion temperatures T_e and T_i are assumed to be equal ($T_e = T_i = T/2$).

Eight physical variables (normalized as summarized in Table 4.1) are evolved in time: poloidal flux ψ , toroidal current density j , poloidal flow potential u , toroidal vorticity ω , plasma mass density ρ , total (ion + electron) pressure ρT , parallel velocity v_{\parallel} and neutral mass density ρ_n , according to the following differential equations:

$$\frac{\partial \psi}{\partial t} = \eta(T) \Delta^* \psi - R[u, \psi] - F_0 \frac{\partial u}{\partial \phi} \quad (4.54)$$

$$j = \Delta^* \psi \quad (4.55)$$

$$R \nabla \cdot \left(R^2 \rho \nabla_{pol} \frac{\partial u}{\partial t} \right) = \frac{1}{2} [R^2 |\nabla_{pol} u|^2, R^2 \rho] + [R^4 \rho \omega, u] + [\psi, j] - \frac{F_0}{R} \frac{\partial j}{\partial \phi} \quad (4.56)$$

$$+ [\rho T, R^2] + R \mu(T) \nabla^2 \omega + \nabla \cdot ((\rho \rho_n S_{ion}(T) - \rho^2 \alpha_{rec}(T)) R^2 \nabla_{pol} u)$$

$$\omega = \nabla_{pol}^2 u = \frac{1}{R} \frac{d}{dR} \left(R \frac{du}{dR} \right) + \frac{d^2 u}{dZ^2} \quad (4.57)$$

$$\frac{\partial \rho}{\partial t} = -\nabla \cdot (\rho \mathbf{v}) + \nabla \cdot (D_{\perp} \nabla_{\perp} \rho + D_{\parallel} \nabla_{\parallel} \rho) + \rho \rho_n S_{ion}(T) - \rho^2 \alpha_{rec}(T) \quad (4.58)$$

$$\frac{\partial(\rho T)}{\partial t} = -\mathbf{v} \cdot \nabla(\rho T) - \gamma \rho T \nabla \cdot \mathbf{v} + \nabla \cdot (\kappa_{\perp} \nabla_{\perp} T + \kappa_{\parallel} \nabla_{\parallel} T) + \frac{2}{3R^2} \eta_{Spitzer}(T) j^2 \quad (4.59)$$

$$- \xi_{ion} \rho \rho_n S_{ion}(T) - \rho \rho_n L_{lines}(T) - \rho^2 L_{brem}(T)$$

$$\rho B^2 \frac{\partial v_{\parallel}}{\partial t} = -\rho \frac{F_0}{2R^2} \frac{\partial(B^2 v_{\parallel}^2)}{\partial \phi} - \frac{\rho}{2R} [B^2 v_{\parallel}^2, \psi] - \frac{F_0}{R^2} \frac{\partial(\rho T)}{\partial \phi} + \frac{1}{R} [\psi, \rho T] \quad (4.60)$$

$$+ B^2 \mu_{\parallel}(T) \nabla_{pol}^2 v_{\parallel} + (\rho^2 \alpha_{rec}(T) - \rho \rho_n S_{ion}(T)) B^2 v_{\parallel}$$

$$\frac{\partial \rho_n}{\partial t} = \nabla \cdot (\mathbf{D}_n : \nabla \rho_n) - \rho \rho_n S_{ion}(T) + \rho^2 \alpha_{rec}(T) + S_n \quad (4.61)$$

where (R, Z, φ) is a direct toroidal coordinate system, ∇_{pol} denotes the del-operator in the poloidal plane, the Poisson brackets are defined as $[f, g] = \frac{\partial f}{\partial R} \frac{\partial g}{\partial Z} - \frac{\partial f}{\partial Z} \frac{\partial g}{\partial R}$ and the parallel gradient as $\nabla_{\parallel} = \mathbf{b}(\mathbf{b} \cdot \nabla)$ where $\mathbf{b} = \mathbf{B}/|\mathbf{B}|$.

The velocity vector is defined as

$$\mathbf{v} = \mathbf{v}_{E \times B} + v_{\parallel} \mathbf{B} = R^2 \nabla \varphi \times \nabla u + v_{\parallel} \mathbf{B} \quad (4.62)$$

The resistivity η which appears in the induction equation (Eq. 4.54) is typically increased in JOREK simulations compared to the Spitzer value in order to thicken the current sheets which otherwise would be too thin to be resolved (for the same purpose, a hyper-resistivity term, not shown in Eq. 4.54, may be used). However, in the energy equation (Eq. 4.59), the Joule heating term $\eta_{Spitzer} j^2$ uses the Spitzer resistivity in order not to alter the energy balance.

Table 4.1: Normalization of quantities in JOREK. Variable names with subscript ‘‘SI’’ denote quantities in SI units, while variables without this subscript are the ones used in JOREK. n_0 and ρ_0 are the initial central plasma particle and mass density. The vacuum magnetic permeability is denoted μ_0 and the Boltzmann constant k_B .

R_{SI} [m]	= R	Major radius
Z_{SI} [m]	= Z	Vertical coordinate
\mathbf{B}_{SI} [T]	= \mathbf{B}	Magnetic field vector; see Eq. (4.52)
ψ_{SI} [T · m ²]	= ψ	Poloidal magnetic flux
$j_{\phi,SI}$ [A · m ⁻²]	= $-j/(R \mu_0)$	Toroidal current density; $j_{\phi,SI} = \mathbf{j}_{SI} \cdot \hat{e}_{\phi}$
n_{SI} [m ⁻³]	= ρn_0	Particle density
ρ_{SI} [kg · m ⁻³]	= $\rho \rho_0$	Mass density = ion mass × particle density
T_{SI} [K]	= $T/(k_B \mu_0 n_0)$	Temperature = electron + ion temperature
p_{SI} [N · m ⁻²]	= $\rho T/\mu_0$	Plasma pressure
\mathbf{v}_{SI} [m · s ⁻¹]	= $\mathbf{v}/\sqrt{\mu_0 \rho_0}$	Velocity vector; see Eq. (4.62)
$v_{\parallel,SI}$ [m · s ⁻¹]	= $v_{\parallel} \cdot B_{SI}/\sqrt{\mu_0 \rho_0}$	Parallel velocity component, where $B_{SI} = \mathbf{B}_{SI} $
u_{SI} [m · s ⁻¹]	= $u/\sqrt{\mu_0 \rho_0}$	Velocity stream function
$\omega_{\phi,SI}$ [m ⁻¹ · s ⁻¹]	= $\omega/\sqrt{\mu_0 \rho_0}$	Toroidal vorticity; see Eq. (4.57)
t_{SI} [s]	= $t \cdot \sqrt{\mu_0 \rho_0}$	Time
γ_{SI} [s ⁻¹]	= $\gamma/\sqrt{\mu_0 \rho_0}$	Growth rate; $\gamma_{SI} = \ln[E_{SI}(t_2)/E_{SI}(t_1)]/[2\Delta t_{SI}]$; Energy $E_{SI}[J]$
η_{SI} [$\Omega \cdot m$]	= $\eta \cdot \sqrt{\mu_0/\rho_0}$	Resistivity
μ_{SI} [kg · m ⁻¹ · s ⁻¹]	= $\mu \cdot \sqrt{\mu_0/\rho_0}$	Dynamic viscosity
D_{SI} [m ² · s ⁻¹]	= $D/\sqrt{\mu_0 \rho_0}$	Particle diffusivity (\parallel or \perp)
κ_{SI} [m ⁻¹ · s ⁻¹]	= $\kappa \cdot n_0/\sqrt{\mu_0 \rho_0}$	Heat diffusivity (\parallel or \perp), where χ_{SI} [m ² · s ⁻¹] = κ_{SI}/n_{SI}
$S_{ion,SI}$ [m ⁻³ · s ⁻¹]	= $S_{rec}/(\sqrt{\mu_0 \rho_0} n_0)$	Ionisation rate coefficient
$\alpha_{rec,SI}$ [m ⁻³ · s ⁻¹]	= $\alpha_{rec}/(\sqrt{\mu_0 \rho_0} n_0)$	Recombination rate coefficient
$E_{ion,SI}[J]$	= $\xi_{ion}/(\frac{2}{3}\mu_0 n_0)$	Ionisation energy
$L_{lines/brem,SI}[W \cdot m^3]$	= $L_{lines/brem}/(\frac{2}{3}\mu_0 \sqrt{\mu_0 \rho_0} n_0^2)$	Radiation rate coefficients (lines or bremsstrahlung)

Impurities in JOREK S_{ion} and α_{rec} designate respectively the ionization and recombination rate coefficients for deuterium, parameterized according to [Voronov 1997; Huddlestone and Leonard 1965].

$$S_{ion}(T_e) = \langle \sigma_{ion} v \rangle = 0.2917 \times 10^{-13} \left(\frac{13.6}{T_e} \right)^{0.39} \frac{1}{0.232 + \frac{13.6}{T_e}} \exp\left(-\frac{13.6}{T_e}\right) \quad (4.63)$$

$$\alpha_{rec}(T_e) = \langle \sigma_{rec} v \rangle = 0.7 \times 10^{-19} \left(\frac{13.6}{T_e} \right)^{\frac{1}{2}} \quad (4.64)$$

where S_{ion} and α_{rec} are in m³/s and T_e is in eV.

ξ_{ion} is the normalized ionization energy of a D atom, which is considered to be 13.6 eV.

In this model, we neglect the bond-dissociation energy of D_2 molecules. Assuming that this energy is the same as for H_2 molecules, i.e. about 5 eV, this seems reasonable in the sense that it is smaller than the ionisation energy of two D atoms by a factor of about 5. L_{lines} and L_{brem} designate the line and bremsstrahlung radiation rate coefficients. A fit of ADAS data^j is used for line radiation and bremsstrahlung is parameterized according to [J. Wesson 2004] (Eq. 4.25). It is interesting to compare the energy sink rates related to atomic physics which appear in the energy equation (Eq. 4.59), i.e. $\xi_{ion}S_{ion}$, L_{lines} and L_{brem} . This is done in Figure 4.2. For $T_e > 10$ eV, ionization slightly dominates line radiation, while below 10 eV, line radiation is dominant. The bremsstrahlung rate coefficient is roughly 5 orders of magnitude smaller than the other two rates, but of course it should not be compared directly since in Eq. 4.59 it is multiplied by ρ^2 whereas the other rates are multiplied by $\rho\rho_n$. The relative influence of these terms will be discussed in details in section 6.2.5.

S_n is a volumetric neutral source term used to simulate the influx of gas from the MGI.

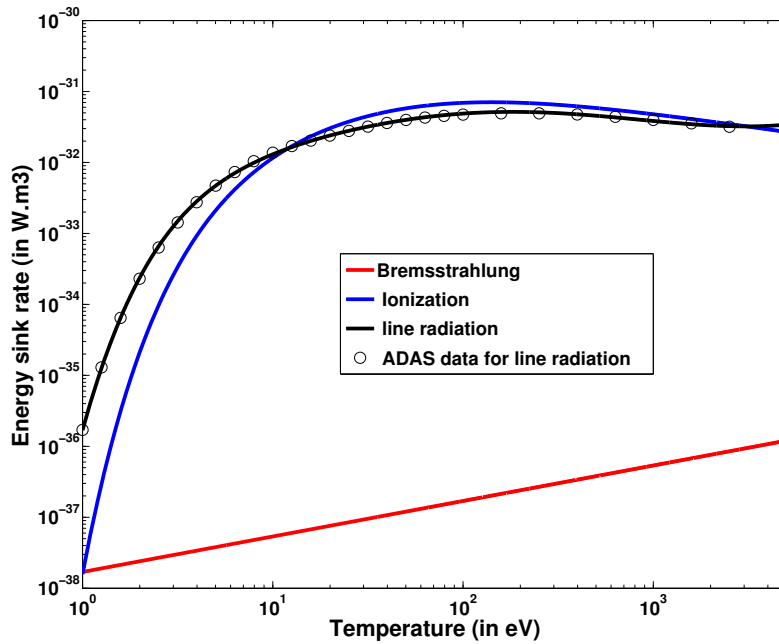


Figure 4.2: Energy sink rates related to atomic physics which appear in Eq. 4.59: $\xi_{ion}S_{ion}$, L_{lines} and L_{brem}

Its parametrization will be described in detail in section 6.2.2.

One limit of this model is the purely diffusive treatment of neutral transport, which does not stem directly from first principles as IMAGINE does. This point must be kept in mind in the interpretation of the results presented in chapter 6.

Boundary conditions Ideal wall boundary conditions are implemented where the boundary of the computational domain is parallel to the magnetic flux surfaces. It means that

^jSummers n.d.

all variables are constant on this type of boundary. At the divertor targets, where flux surfaces intersect the boundary, Bohm boundary conditions are applied for the parallel velocity, the temperature and the density: the parallel velocity is imposed to be equal to the sound speed on the divertor: $v_{\parallel} = c_s = \sqrt{\gamma T_e / m_i}$, and the temperature and density outflow is left free. For all other variables, Dirichlet conditions are imposed, i.e. their values are constant on the boundary. It is planned to study the influence of reflective conditions and recycling in future work.

4.4.3 Initialization, numerics and computational resources

JOREK is a 3D code and its grid is discretized in 2D bi-cubic Bezier finite elements^k in the poloidal plane and the toroidal direction is decomposed in Fourier series. The Bezier elements have their own local coordinates (s,t) related to the global cylindrical coordinate system (R, Z, φ) in which the equations are defined. In a JOREK run, the equilibrium flux surfaces are first calculated by solving the Grad-Shafranov equation for the magnetic flux (see 4.4.1). The grid is then re-aligned to follow these flux surfaces. An example of flux-aligned grid is shown in Figure 4.3. The boundary of the computational domain is

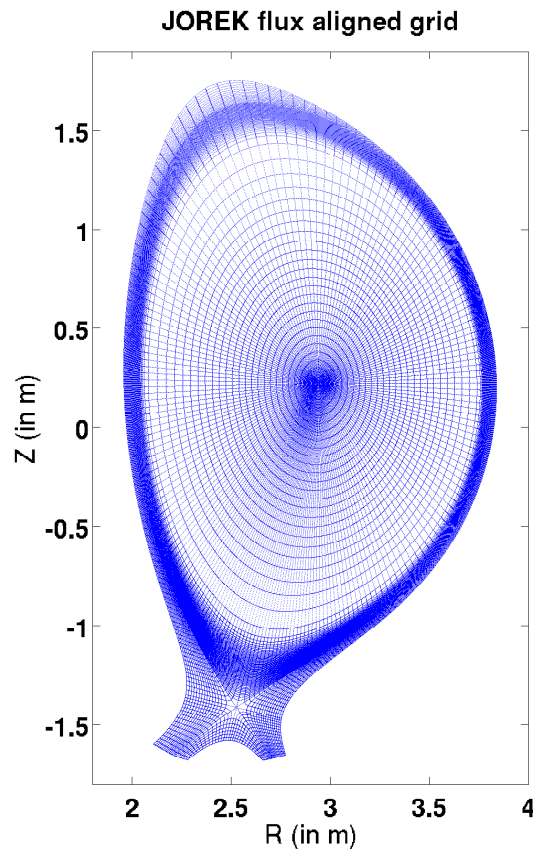


Figure 4.3: *JOREK flux-aligned grid*

^kCzarny and G. T. A. Huysmans 2008; G T A Huysmans, Pamela, et al. 2009.

chosen to be close to the tokamak walls, in the far SOL, and to follow the divertor plates. Then, the equilibrium flows are established in a time scale of $\simeq 10^2$ JOREK times t_J ($t_J \simeq \tau_A$, with τ_A the Alfvén time defined by $\tau_A = a\sqrt{\mu_0 n_i m_i}/B$).

Because of the Bohm conditions on the targets ($v_{\parallel} = c_s$), the time step needs to be small at the beginning ($\simeq 10^{-3}t_J$) and progressively increased. The perturbation modes ($n > 1$) are then added in the simulation. Typical time steps evolve between $10^{-2} t_J$ and $10 t_J$ (i.e. $\simeq 3.5 \cdot 10^{-2} - 3.5 \mu\text{s}$). The equations (4.54-4.61) presented above are solved in the weak form, fully implicitly at each time step using the Gears scheme¹. The matrix is inverted with the PaStiX sparse matrix library (Parallel Sparse matrix package^m), using the GMRESⁿ method. The code is parallelized with MPI and OpenMP. Most of our simulations have been run on the HELIOS (from IFERC-CSC) and CCRT-CURIE (from CEA) supercomputers. A typical run on HELIOS uses 36 nodes and one time step takes around 200 s. A full simulation represents around 10^4 node-hours.

After the simulations, post-processing is done to visualize, analyze and interpret the data.

¹Hoelzl, Merkel, et al. 2012.

^mHénon, Ramet, and Roman 2002.

ⁿSaad and Schultz 1986.

5

First principle modeling of neutral gas penetration during massive gas injection

Contents

2.1	Disruptions and their consequences	16
2.1.1	Disruption phases	16
2.1.2	Consequences of disruptions	17
2.2	Causes of disruptions	23
2.3	Disruption control strategies	26
2.3.1	Disruption avoidance	27
2.3.2	Disruption prediction and mitigation	27

The next two chapters will focus on simulating an experimental shot done with the JET tokamak. We will first quickly describe the experimental shot (then with more details in section 6.2.1). Then, we will apply the codes described in the previous chapter to get a better understanding of the physics involved in a MGI-triggered disruption. In the present chapter, we will use the code IMAGINE (see 4.3) to study the gas propagation from the reservoir to the plasma and the interaction between the gas and the plasma during the pre-TQ phase. The JOREK code will be applied in the next chapter to study the TQ and the MHD events responsible for it.

5.1 JET shot 86887

We simulate JET pulse 86887 which has been done during MGI experiments (summer 2013). This is an Ohmic D plasma pulse with $B_t = 2$ T, $I_p = 2$ MA, $q_{95} = 2.9$ in which a disruption was MGI-triggered by activating the Disruption Mitigation Valve number 2 (DMV-2), pre-loaded with D_2 at 5 bar ($P_{res}^{exp,D_2} = 5 \cdot 10^5$ Pa), at $t = 61.013$ s. The volume of the DMV2 reservoir is $V_{res}^{exp} = 10^{-3}$ m³ and its temperature is about 293 K, so it initially contains about $1.2 \cdot 10^{23}$ D_2 molecules, which represents roughly 100 times more D nuclei than initially present in the plasma.

Electron density n_e and temperature T_e profiles measured by High Resolution Thomson Scattering (HRTS) just before the MGI, together with fits of these profiles used as initial conditions in IMAGINE (and JOREK) simulations, are shown in Figure 5.1. Central values are $n_e = 3 \cdot 10^{19}$ m⁻³ and $T_e = 1.2$ keV. In JOREK, the transport of neutrals is assumed to

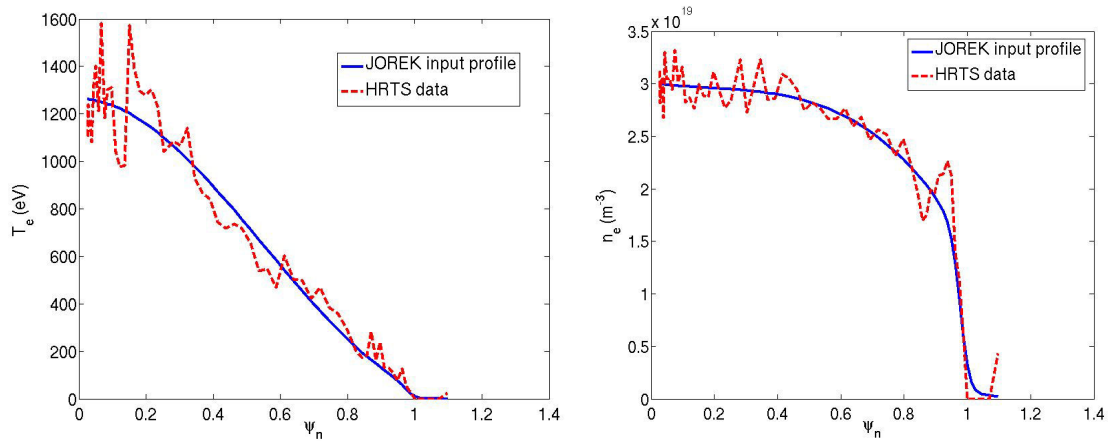


Figure 5.1: *Experimental T_e and n_e profiles from high resolution Thomson scattering (dashed lines) and fits of these profiles used as initial conditions in the JOREK simulations (plain lines)*

be diffusive, for simplicity and numerical reasons. However, in the equations presented in section 4.3 (eq. 4.37), which stem from first principles and which are solved by IMAGINE, the transport of neutrals is purely convective. We wonder here which mechanisms influence the neutrals dynamics during the cooling phase of a MGI-triggered disruption.

5.2 Simulation settings

As IMAGINE is a 1D code, the realistic geometry of the gas injector cannot be used. However, we can choose the input parameters to match three critical experimental quantities: the initial number of neutrals in the reservoir N_{res} , the initial flux of neutrals out of it Φ_{res} , and the sound velocity in the reservoir $c_{s,res}$.

In IMAGINE, three input parameters are available regarding the DMV: the initial neutral density n_{res}^{sim} and pressure P_{res}^{sim} in the reservoir and the radial size of the reservoir $\delta_{x,res}^{sim}$. Their values are thus chosen according to experimental quantities.

One difficulty when simulating a D_2 MGI is that the model would in principle require a set

of equations for the D_2 molecules with $\gamma = 7/5$, and a set of equations for the D atoms with $\gamma = 5/3$. However, for simplicity, we ignore here the existence of D_2 molecules and do as if the reservoir contained D atoms. By so doing, we neglect the dissociation energy of D_2 molecules. Assuming that this energy is the same as for H_2 molecules, i.e. about 5 eV, this seems reasonable in the sense that it is smaller than the ionization energy of two D atoms by a factor of about 5. Thus, in the simulations, n_0 is the D atom density. When setting the input parameters for the simulations, one should pay special attention to this point. Hence, in the equations below, we use a superscript to specify whether quantities refer to D atoms or D_2 molecules.

Considering the simulation domain as a slab of length $2\pi R_0$ and height $2\pi a$, with R_0 the major radius and a the minor radius of the machine, the three above-mentioned conditions translate to:

$$N_{res}^D = 2V_{res}^{exp} n_{res}^{exp,D_2} = 4\pi^2 R_0 a \delta_{x,res}^{sim} n_{res}^{sim,D} \quad (5.1)$$

$$\Phi_{res}^D = 2A_{orifice}^{exp} c_{s,res}^{exp,D_2} n_{res}^{exp,D_2} = 4\pi^2 R_0 a c_{s,res}^{sim,D} n_{res}^{sim,D} \quad (5.2)$$

$$c_{s,res}^{exp,D_2} = \left(\gamma_{D_2} \frac{P_{res}^{exp,D_2}}{2m_D n_{res}^{exp,D_2}} \right)^{1/2} = c_{s,res}^{sim,D} = \left(\gamma_D \frac{P_{res}^{sim,D}}{m_D n_{res}^{sim,D}} \right)^{1/2} \quad (5.3)$$

Equation 5.2 anticipates on the result presented in the next section that the gas velocity at the exit of the DMV is the sound velocity (both in the experiment and simulation).

After some simple algebra, equations 5.1, 5.2 and 5.3 yield the following expressions for the input parameters $n_{res}^{sim,D}$, $P_{res}^{sim,D}$ and $\delta_{x,res}^{sim}$:

$$n_{res}^{sim,D} = \frac{2A_{orifice}^{exp}}{4\pi^2 R_0 a} n_{res}^{exp,D_2} = \frac{2A_{orifice}^{exp}}{4\pi^2 R_0 a} \frac{P_{res}^{exp,D_2}}{k_B T_{res}^{exp,D_2}} \quad (5.4)$$

$$P_{res}^{sim,D} = \frac{\gamma_{D_2}}{\gamma_D} \frac{A_{orifice}^{exp}}{4\pi^2 R_0 a} P_{res}^{exp,D_2} \quad (5.5)$$

$$\delta_{x,res}^{sim} = \frac{V_{res}^{exp}}{A_{orifice}^{exp}} \quad (5.6)$$

where V_{res}^{exp} is the volume of the gas reservoir in the experiment.

5.3 Gas propagation in vacuum

Simulations of D_2 MGI in JET have been carried out. The initial conditions are a constant neutral density $n_{res}^{sim,D}$ in the reservoir (blue curve on Figure 5.2 and calculated to match JET 86887 MGI settings) and n_e, T_e profiles from the HRTS presented above for the plasma (between $r = 0$ and $r = 1$). Between the gas reservoir and the plasma, the neutrals propagate into a vacuum tube. The gas propagation into this tube is found similar to measurements in laboratory experiments (see [Bozhenkov, Lehnen, et al. 2011]) with the formation of a rarefaction wave and a velocity of $3 \cdot c_{s,res}$ for the first particles.

This rarefaction wave is the analytical solution of the 1D Euler equations for neutrals which are solved by IMAGINE during this first phase (the neutrals have not yet reached the plasma). The modeling of this phase allows one to obtain a realistic neutral flux at the edge of the plasma which is indeed found similar to the experimental measurement at the vacuum tube exit^a. The formula given in [Bozhenkov, Lehnen, et al. 2011] for the number of neutrals exiting the vacuum injection tube and entering the plasma per unit time (formula which is used in JOREK) is compared to IMAGINE results in Figure 5.3. One can see that the first phase of the gas injection is similar with the difference that IMAGINE takes into account the reservoir depletion whereas the Bozhenkov formula does not.

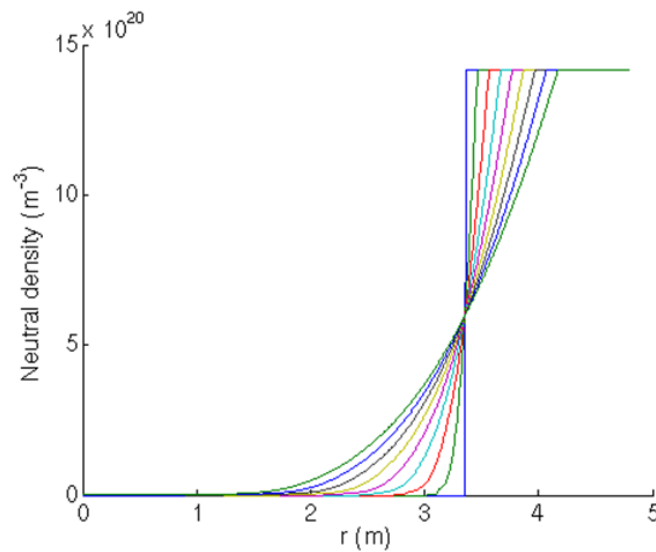


Figure 5.2: Evolution of the neutral density profiles for the gas propagation in the reservoir and the vacuum injection tube, just before reaching the plasma

^aBozhenkov, Lehnen, et al. 2011.

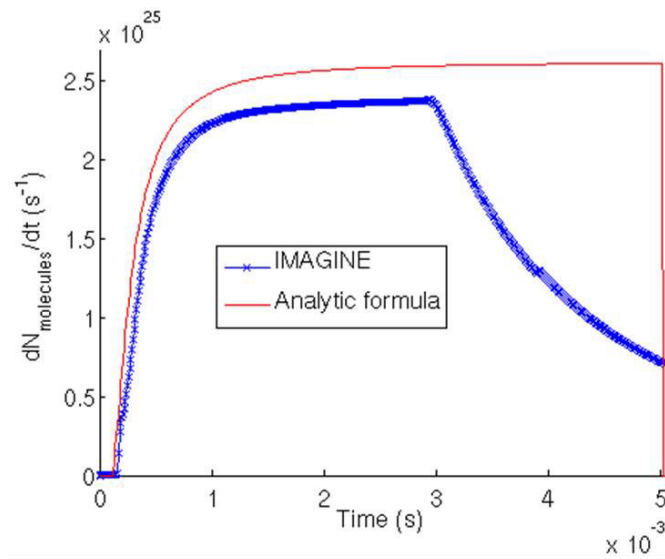


Figure 5.3: Comparison between *IMAGINE* and *Bozhenkov* formula for the neutral gas flow at the plasma edge

5.4 Cold front penetration

After this first phase of the gas propagation into the vacuum tube, the first neutral particles reach the plasma edge. The neutrals thus interact with the plasma by many atomic processes and the dominant physics mechanisms are still unclear in the literature. Theoretical models have been proposed in [Rozhansky, Senichenkov, et al. 2006; Parks and Wu 2014]. Parks states that the plasma pressure impresses on the frontal surface of the gas jet and drives a shock wave running inwards and backwards. However, no justification of this statement is given. For Rozhansky, the neutrals are pushing the plasma by creating an $E \times B$ flow and several mechanisms can impact this flow (either braking or accelerating it).

In IMAGINE, as described in section 4.3, we include ionization, recombination, charge-exchange, bremsstrahlung and line radiation processes. The aim is to understand the important mechanisms driving the gas penetration into the plasma.

For our simulation of the JET shot 87886, it takes 0.9 ms for the gas to propagate from the reservoir to the plasma edge, as presented in the previous section. Then, it starts penetrating into the plasma. It is found that the energy transfer by charge-exchange plays a major role in the gas penetration into the plasma and is a key ingredient to recover a realistic pre-TQ time as well as a realistic increase of the plasma density. Indeed, if we neglect charge-exchange in the simulation, we obtain a very fast and unrealistic cooling of the whole plasma. Figure 5.4 presents the evolution of the neutral density and the electron density profiles in a simulation neglecting charge-exchange. Figure 5.5 presents the evolution of the associated electron temperature profile. In this case, the gas rapidly

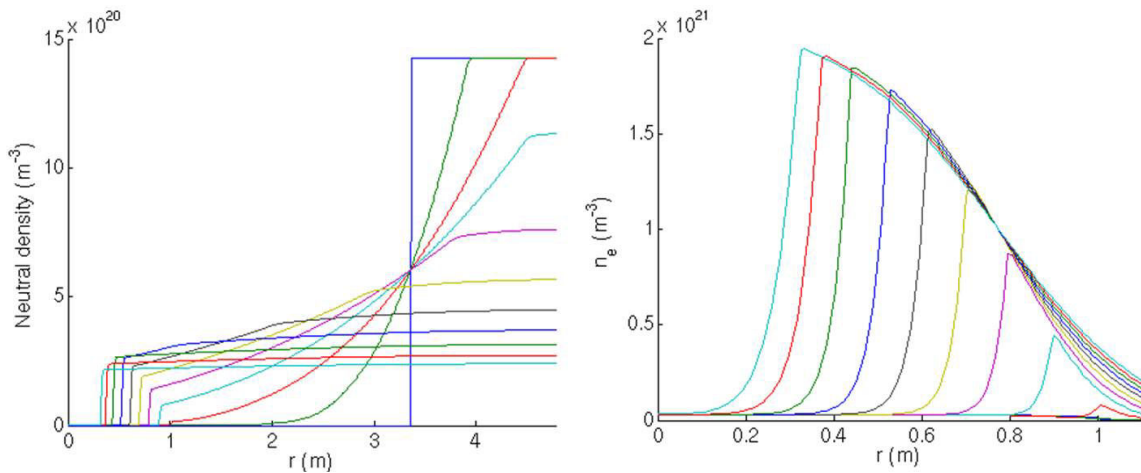


Figure 5.4: *left: Evolution of the neutral density profile, right: evolution of the electron density profile for the simulation without charge-exchange*

cools the whole plasma and propagates from the edge to the plasma center. It takes $\simeq 1$ ms for the gas to reach the $q = 2$ rational surface and only $\simeq 5$ ms to reach the plasma center and cool the whole plasma. Experimentally it takes a much longer time ($\simeq 12$ ms) to get a TQ associated to MHD events (absent in these simulations) as can be seen on Figure 6.7. In Figure 5.4 one can also observe that the increase of electron

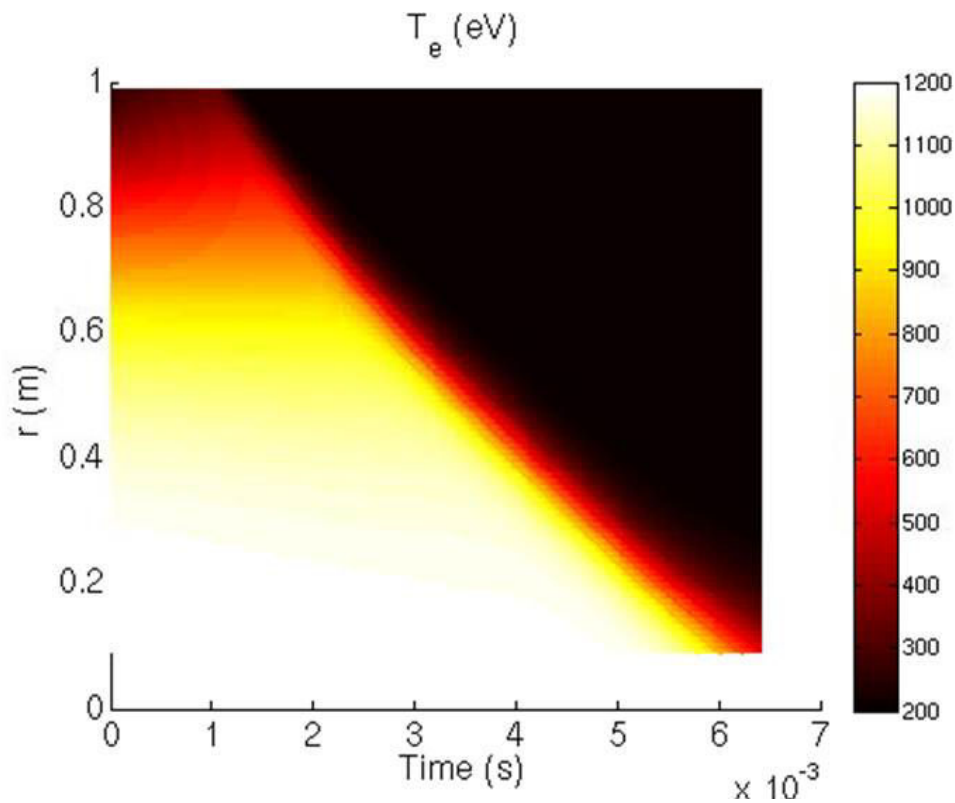


Figure 5.5: *Electron temperature evolution for the simulation neglecting charge-exchange*

density induced by the gas penetration is important (up to $2 \times 10^{21} \text{m}^{-3}$) and much higher than what is measured by interferometry for this experimental shot (see 6.14). In the simulation which includes charge-exchange, one can observe in Figure 5.7 a much slower gas penetration and plasma cooling. The slower gas penetration in this case is attributed to the very fast charge-exchange heating of the neutrals, which creates a shock wave slowing down the gas (see Figure 5.6 which presents the evolution of the neutral density profile). Only a fraction of the injected gas is transmitted, thus reducing the gas penetration as well as the increase of the electron density (see Figure 5.6). The increase of n_e is indeed one order of magnitude lower and comparable to the interferometry measurement in this case.

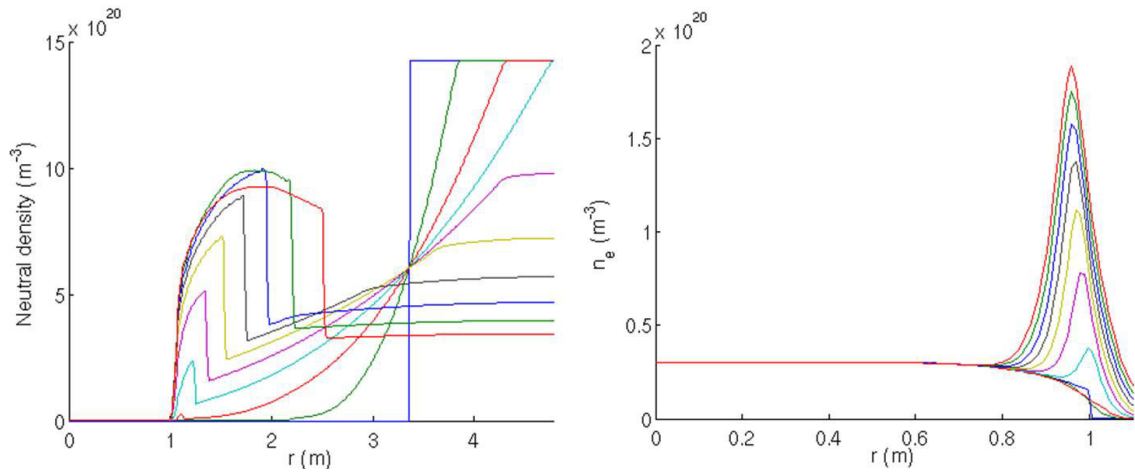


Figure 5.6: *left: Evolution of the neutral density profile, right: evolution of the electron density profile for the simulation with charge-exchange*

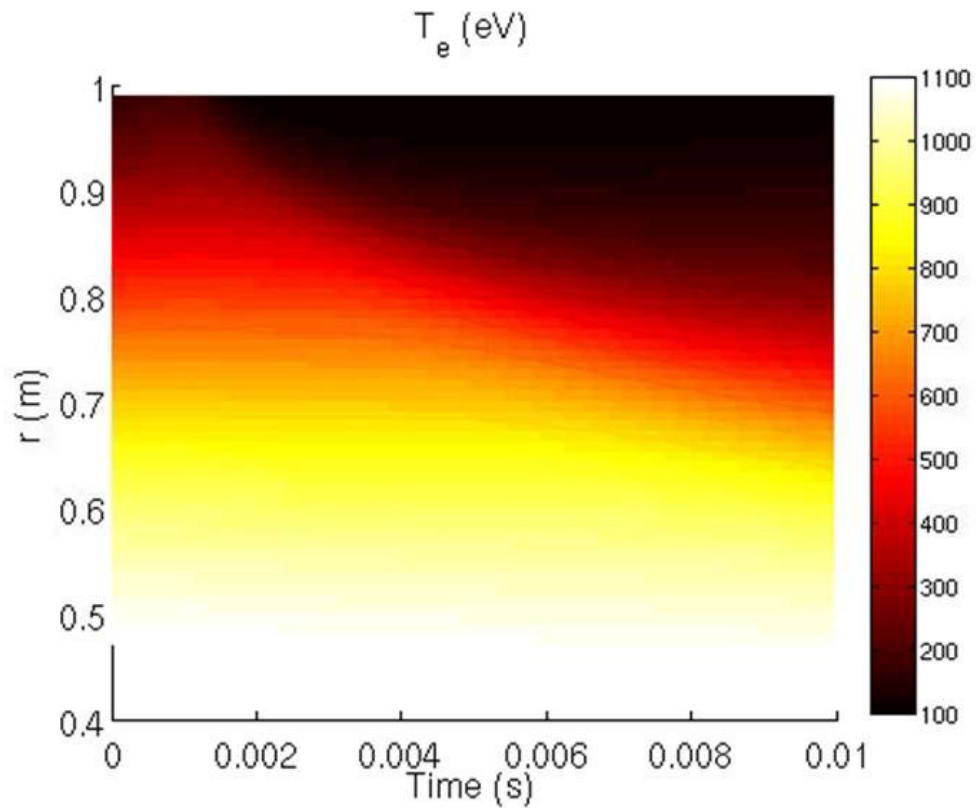


Figure 5.7: *Electron temperature evolution for the simulation including charge-exchange*

5.5 Energy conservation equations

From eq.4.34, 4.35, 4.36, 4.37, 4.38 and 4.39, we can write energy conservation equations for electrons, ions of the plasma and neutrals. For the electrons, we have:

$$\begin{aligned} \partial_t\left(\frac{3}{2}n_e T_e\right) = & \partial_x(\chi n_e \partial_x T_e) \\ & - n_e(n_0 I E_{ion} + n_0 L + n_e R \frac{3}{2} T_e) \end{aligned} \quad (5.7)$$

For the ions, we have:

$$\begin{aligned} \partial_t\left(\frac{3}{2}n_e T_i\right) = & \partial_x(\chi n_e \partial_x T_i) \\ & + \frac{3}{2}n_e(IP_0/e - n_e R T_i - \langle \sigma v \rangle_{cx} (n_0 T_i - P_0/e)) \end{aligned} \quad (5.8)$$

And for the neutrals, we have:

$$\begin{aligned} \partial_t\left(\frac{P_0}{\gamma-1} + \frac{1}{2}m_0 n_0 V_0^2\right) = & - \partial_x\left(\frac{\gamma P_0 V_0}{\gamma-1} + \frac{1}{2}m_0 n_0 V_0^3\right) \\ & - \frac{1}{2}m_0 V_0^2 n_e (n_0 I + n_e R + 2n_0 \langle \sigma v \rangle_{cx}) \\ & + \frac{n_e}{\gamma-1} (-IP_0 + n_e R e T_i + \langle \sigma v \rangle_{cx} (e n_0 T_i - P_0)) \end{aligned} \quad (5.9)$$

It is also interesting to write the energy conservation for ions and neutrals:

$$\begin{aligned} \partial_t\left(\frac{P_0}{\gamma-1} + \frac{1}{2}m_0 n_0 V_0^2 + \frac{3}{2}n_e e T_i\right) = & - \partial_x\left(\frac{\gamma P_0 V_0}{\gamma-1} + \frac{1}{2}m_0 n_0 V_0^3\right) \\ & + \partial_x(\chi n_e \partial_x T_i) \\ & - \frac{1}{2}m_0 V_0^2 n_e (n_0 I + n_e R + 2n_0 \langle \sigma v \rangle_{cx}) \end{aligned} \quad (5.10)$$

Then, we can plot each term of these equations, for the simulation which includes charge-exchange.

Figure 5.8 presents the electron energy balance. The electrons lose energy, mostly by ionization. Note that, as specified in section 4.3.3, radiation is lower than experimentally. Figure 5.9 presents the ion energy balance. Plasma ions lose energy by charge-exchange and gain energy by ionization. The energy of the neutrals is almost constant, as seen on Figure 5.10 which presents the ion + neutral energy balance. The code recovers the energy conservation and the energy lost by the system is attributed to the work done by the braking force on ionized species.

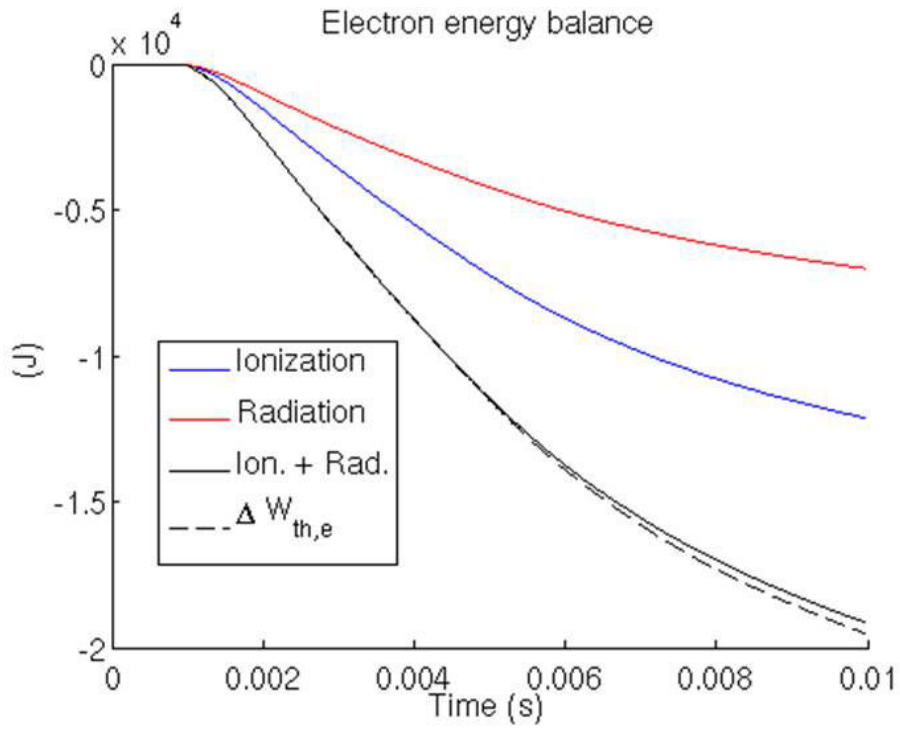


Figure 5.8:

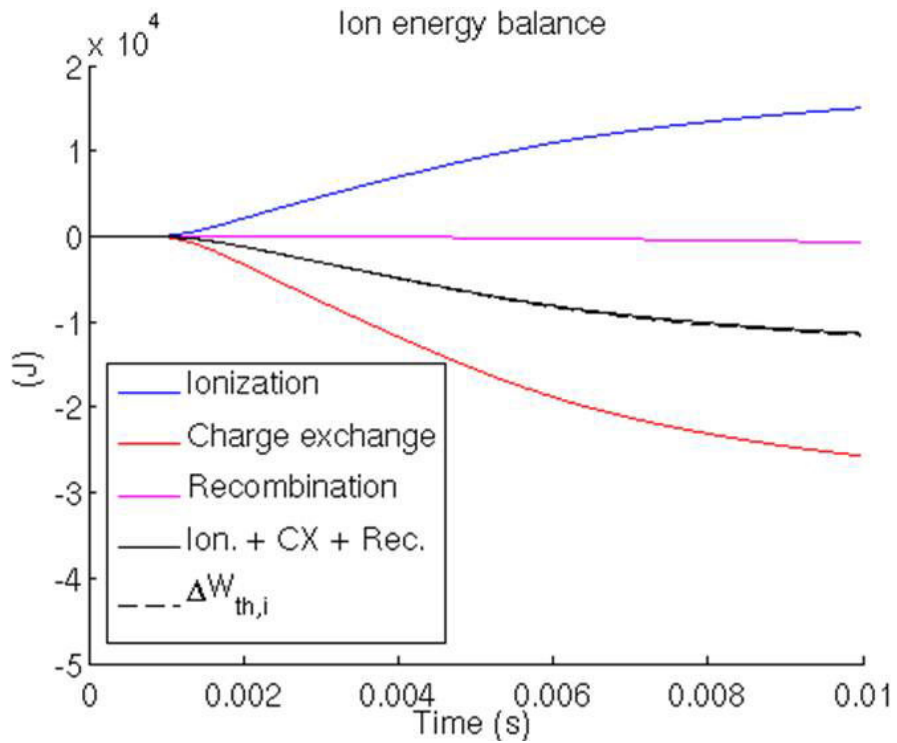


Figure 5.9:

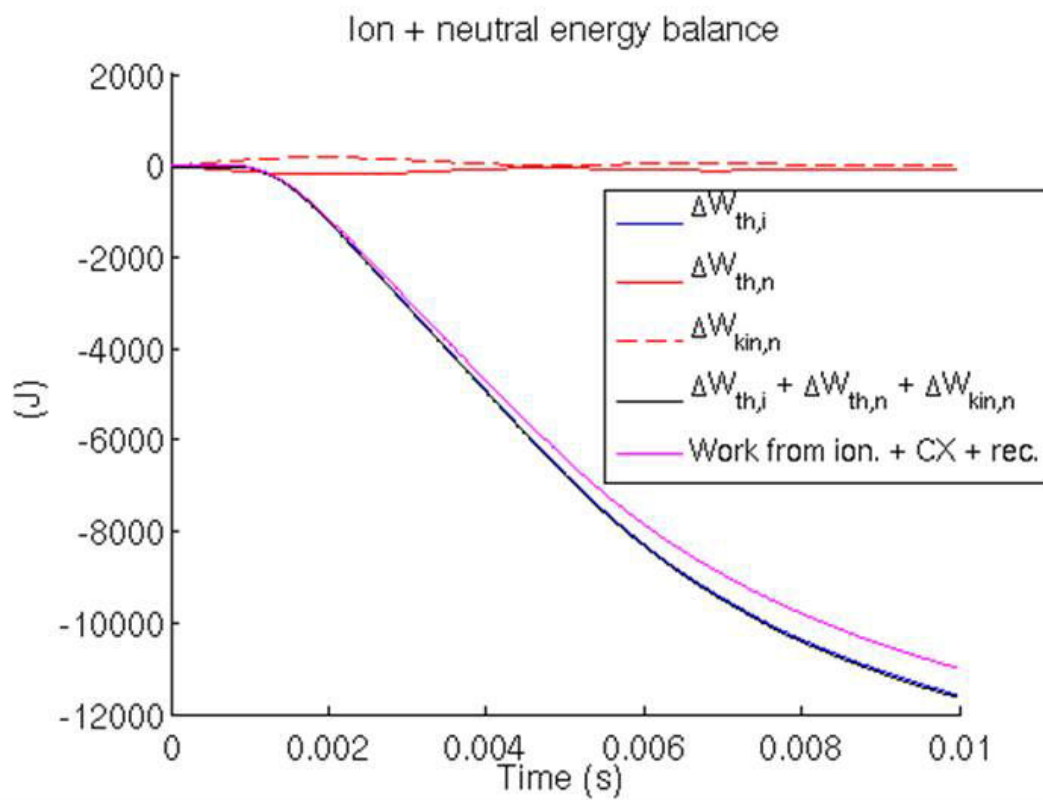


Figure 5.10:

6

3D MHD non-linear MHD modeling of the thermal quench

Contents

3.1 Thermal loads mitigation	33
3.2 Mitigation of runaway electron beams	35
3.3 Current quench duration control	39

The Thermal quench is one of the most violent macroscopic events in tokamak plasmas, and as its name indicates, it results in the loss of a large fraction of the plasma thermal energy. As it is a very fast event ($\simeq 1\text{ms}$), experimental diagnostics lack resolution (both in time and space) to accurately observe the phenomena occurring during a TQ. Modeling is therefore needed to understand this phase of disruptions. In the following, the JOREK code, presented in section 4.4, will be used.

6.1 Proof-of-principle simulation of a thermal quench in JET

At the beginning of this thesis, it had not been demonstrated that JOREK could simulate TQs and the reasons were unclear. Tore Supra simulations had been made during the PhD of Cedric Reux^a, showing the importance of the $q = 2$ rational surface and the destabilization of MHD modes, mostly tearing modes, by the MGI. The first objective of

^aC Reux 2010.

this thesis was thus to demonstrate the ability to model TQs with JOREK. In order to do that, it was chosen to move to JET simulations, as Tore Supra was in shutdown.

6.1.1 Set-up of neutral injection

The model used for these first simulations is the model presented in section 4.4.2 but without radiation terms, recombination, and ohmic heating. We thus have these equations for ρ , ρT and ρ_n :

$$\frac{\partial \rho}{\partial t} = -\nabla \cdot (\rho \mathbf{v}) + \nabla \cdot (D_{\perp} \nabla_{\perp} \rho + D_{\parallel} \nabla_{\parallel} \rho) + \rho \rho_n S_{ion}(T) \quad (6.1)$$

$$\frac{\partial(\rho T)}{\partial t} = -\mathbf{v} \cdot \nabla(\rho T) - \gamma \rho T \nabla \cdot \mathbf{v} + \nabla \cdot (\kappa_{\perp} \nabla_{\perp} T + \kappa_{\parallel} \nabla_{\parallel} T) - \xi_{ion}^* \rho \rho_n S_{ion}(T) \quad (6.2)$$

$$\frac{\partial \rho_n}{\partial t} = \nabla \cdot (\mathbf{D}_n : \nabla \rho_n) - \rho \rho_n S_{ion}(T) + S_n \quad (6.3)$$

In these simulations, we start from (n_e, T_e) profiles of the JET shot 77803 and we inject $\simeq 100$ times less particles compared to the experiment but with an increased energy loss by ionization ($\xi_{ion}^* \simeq 200$ eV). This particular experimental shot has a pure Argon MGI and the increase of ξ_{ion}^* artificially mimics the high radiative properties of a heavy gas such as Ar. The profile of the neutral source term S_n is axisymmetric and constant in time. The other simulation parameters are similar to the ones which will be detailed in section 6.2.2.

6.1.2 MHD triggered by the MGI

With this early model and these parameters, a TQ is obtained after 35 ms of simulation and lasts less than 1 ms. The very long pre-TQ time is not surprising as we inject few particles. The following sequence of events is observed.

The neutral injection increases the electron density at the edge up to 10^{20} m^{-3} which is 3 times the initial central density and cools down the edge of the plasma with a cold front penetrating inward at a speed of $\simeq 10 \text{ m} \cdot \text{s}^{-1}$. The increase of the plasma resistivity in the cooled region leads to a contraction of the current profile which destabilizes a $m/n = 2/1$ tearing mode 30 ms after the beginning of the injection, giving rise to a clearly visible magnetic island chain (see Figure 6.1). The 2/1 mode grows slowly during $\simeq 10$ ms and a stochastic layer is progressively created from the edge to the $q = 2$ surface (see Figure 6.2). Then, inner modes such as the 3/2, 4/3 and 5/4 grow rapidly, leading to field line stochastization over the whole plasma (see Figure 6.3), with fine structures on the current density distribution as well as the decrease of the central temperature within 1 ms (see Figure 6.5).

The simulated TQ duration is similar to the experiments on JET and so is the number of electrons added to the plasma when the TQ occurs (5.10^{23} particles). On the other

hand, the cooling phase duration (30 ms) is too large compared to the experiments, which is a consequence of the simplified atomic physics in this early model and the insufficient neutral gas flow. Another observation is that a temperature gradient remains at the edge (see Figure 6.6), which prevents the temperature from decreasing to very small values. This observation will be discussed in more detail in section 6.2.5. We also note that the TQ is not associated to a 1/1 internal kink mode, which is in contrast with some other disruption simulations (in particular NIMROD simulations). These simulations

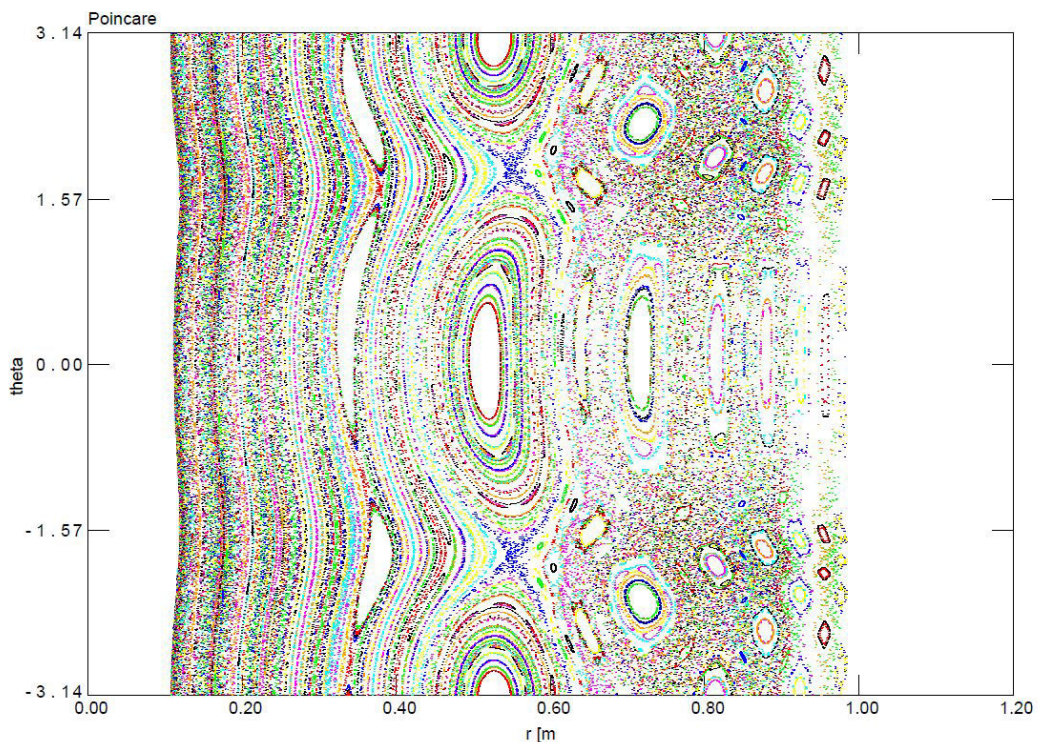


Figure 6.1: *Poincaré plot at $t = 30.6$ ms*

are a proof-of-principle that TQs and fast MHD events associated to it can be modeled with the JOREK code. However, the gas flow rate is much lower than in reality and the atomic physics is simplified, therefore more efforts were needed in order to validate JOREK MGI-triggered disruption simulations.

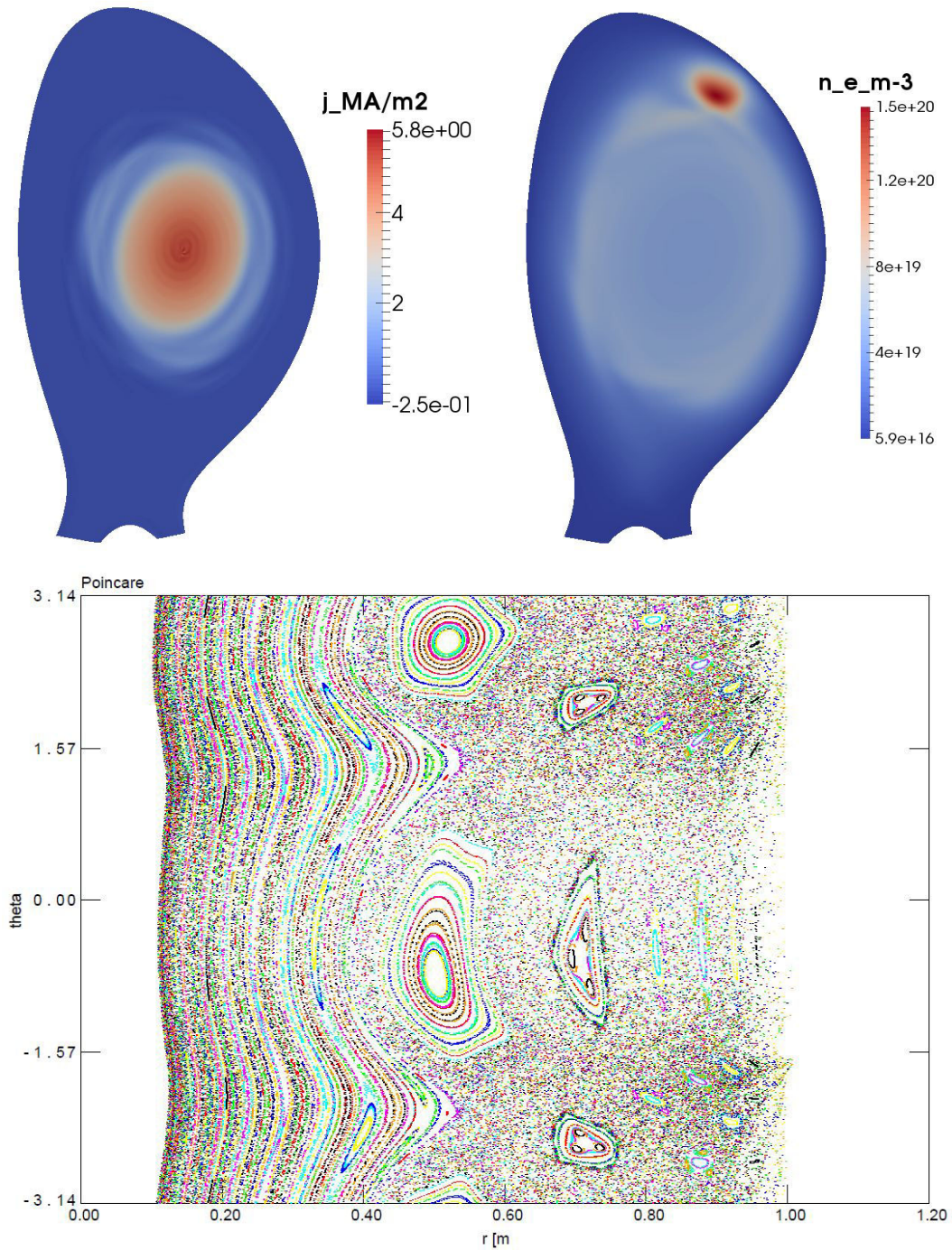


Figure 6.2: Poloidal cross-section of the toroidal current density (left), ion density (right) and associated Poincare plot before the thermal quench, at $t = 33.4$ ms

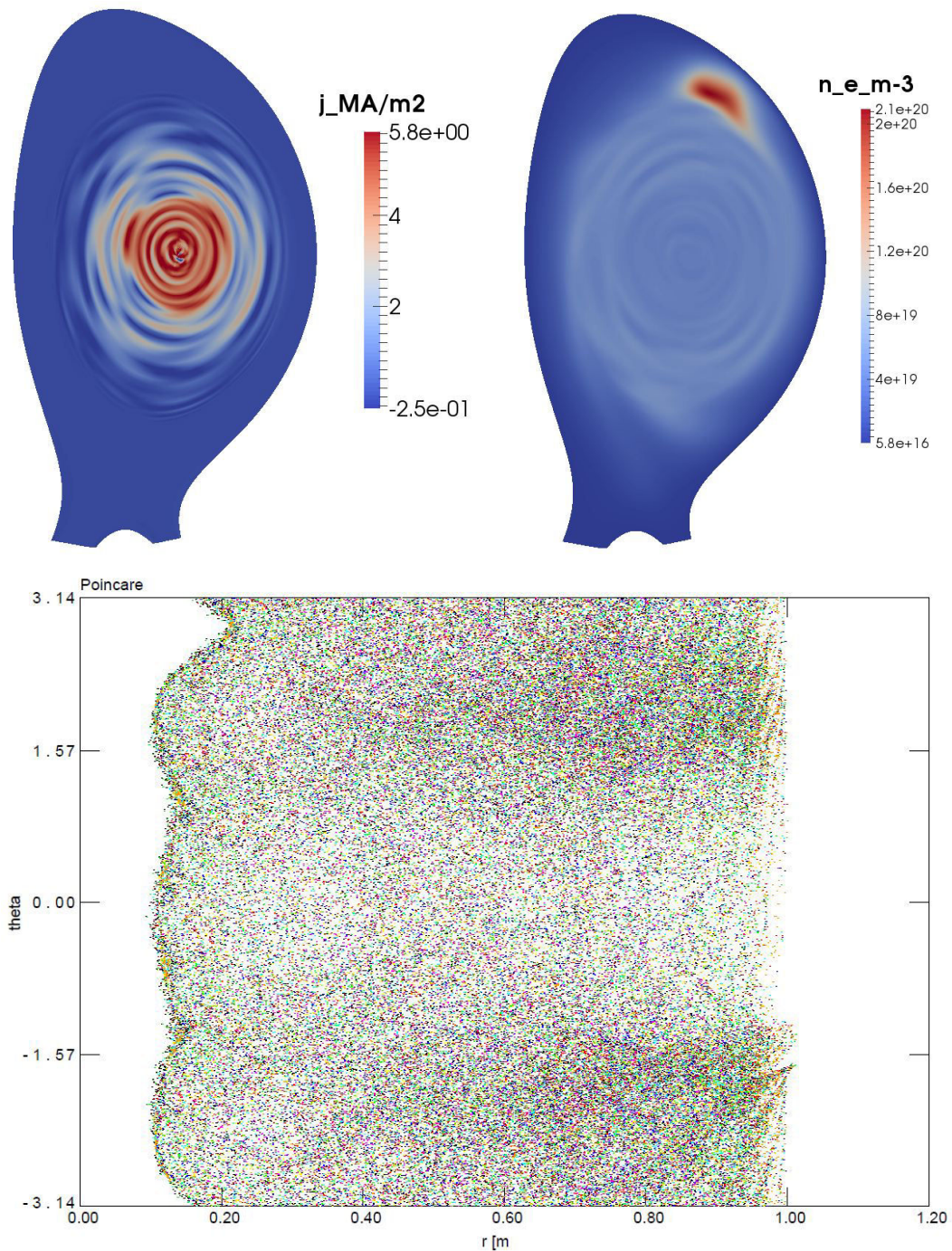


Figure 6.3: Poloidal cross-section of the toroidal current density (left), ion density (right) and associated Poincare plot during the thermal quench, at $t = 36.1$ ms

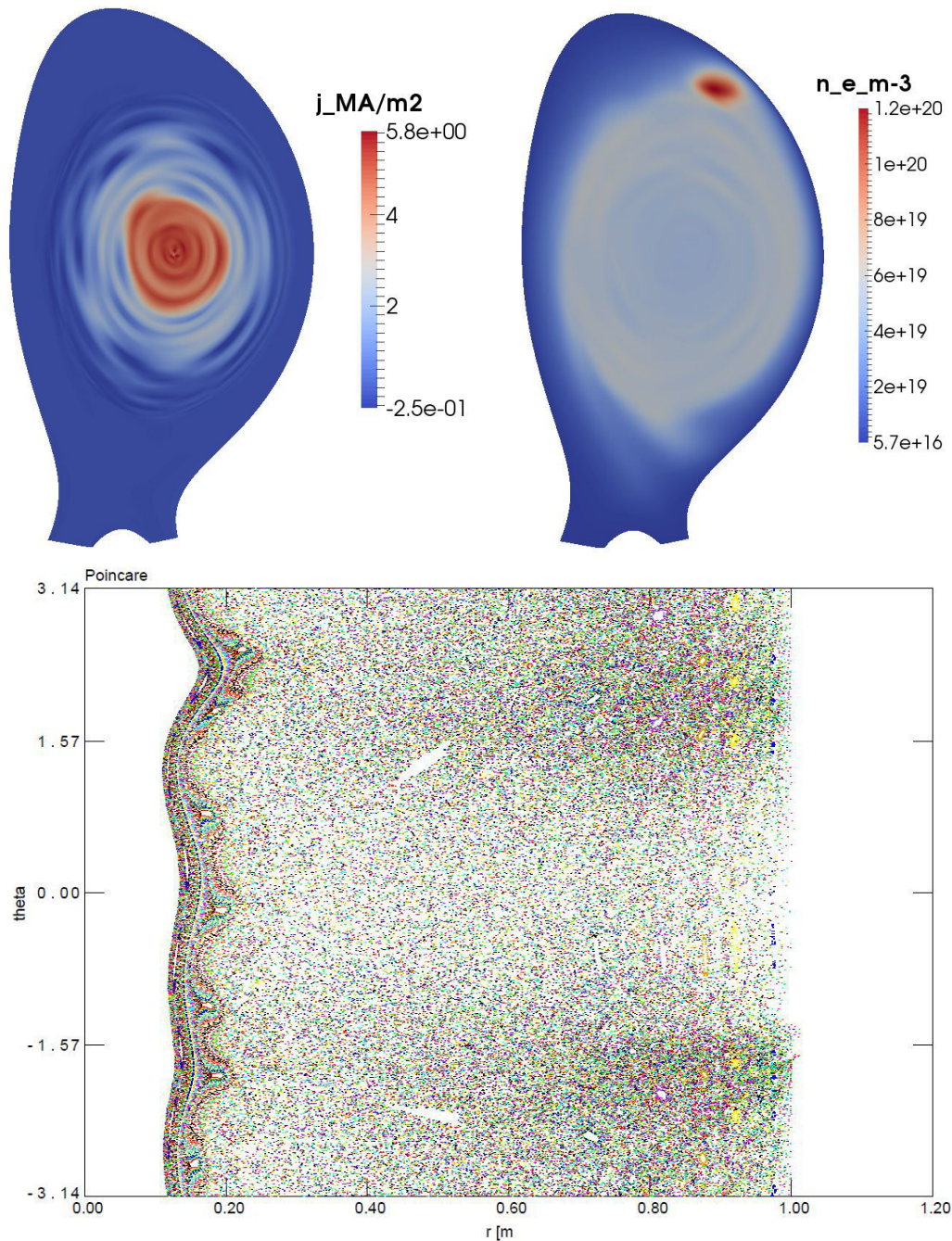
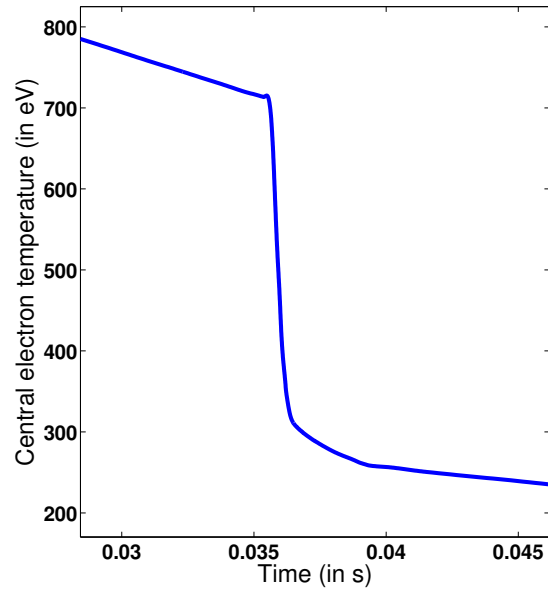
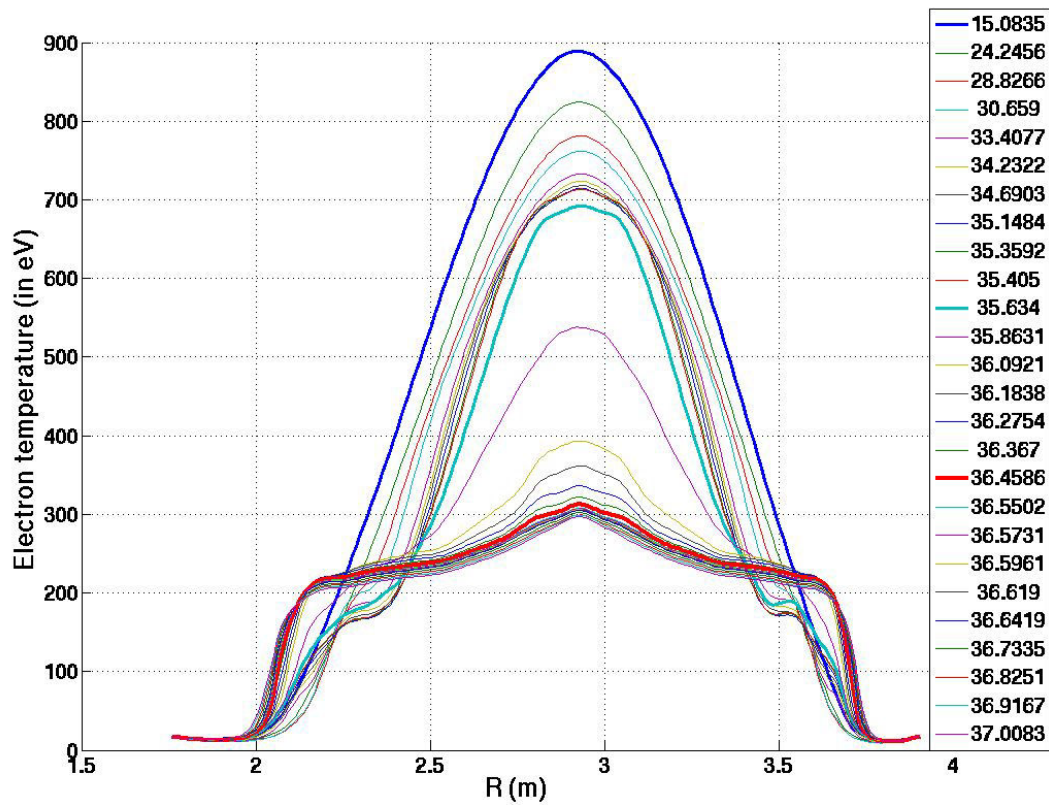


Figure 6.4: Poloidal cross-section of the toroidal current density (left), ion density (right) and associated Poincare plot after the thermal quench, at $t = 37$ ms

Figure 6.5: *Central temperature (in eV)*Figure 6.6: *Successive midplane temperature profile*

6.2 Toward code validation and quantitative comparison with experiment

After these first simulations, it has been decided to move to pure D_2 MGI to validate the code on a MGI presenting a simpler atomic physics than for Argon or Neon. We thus use the equations presented in section 4.4 which are valid for pure D_2 MGI. As recent experiments on JET are focused on Ar MGI or with a Ar/ D_2 mixture, pure D_2 shots were either very old or badly diagnosed. During our participation to the JET experimental campaign in 2013 we thus asked two dedicated shots with pure D_2 MGI to support the comparison between simulations and experiments. As it has been done for the IMAGINE simulations, we now focus on one of these two pulses, the JET shot 86887.

6.2.1 Experimental set-up : JET shot 86887

This shot has already been introduced in section 5.1 but in the previous chapter we focused on the pre-TQ phase and the dynamics of neutrals. Here, we will focus on the TQ phase and the MHD events responsible for it. Figure 6.7 shows an overview of the disruption phase. As previously seen, first effects of the MGI are visible from about 2 ms after the $DMV - 2$ trigger in the form of increases in the line integrated density, radiated power P_{rad} and magnetic fluctuations, and decreases in I_p and the central Soft-X Ray (SXR) signal. In this plot, the MGI is triggered at $t = 0$ s and we recall that it is a pure D_2 MGI with the JET DMV-2 pre-loaded at 5 bar ($5 \cdot 10^5$ Pa). The effects of the MGI intensify in time, especially the drop in SXR, until at about 12 ms, when the SXR signal quickly drops to zero and a burst of MHD activity, a peak on I_p and, a few milliseconds later, a peak on P_{rad} are observed. It is interesting to note that most of the drop of the central SXR signal occurs before the burst of MHD activity and on a rather slow timescale (on the order of 10 ms). The CQ ensues and lasts about 80 ms. We note that magnetic fluctuations and P_{rad} remain at a substantial level during the first 20 ms of this CQ. The main aim of the following simulations will be to shed light on the mechanisms at play in these different phases.

6.2. Toward code validation and quantitative comparison with experiment 79

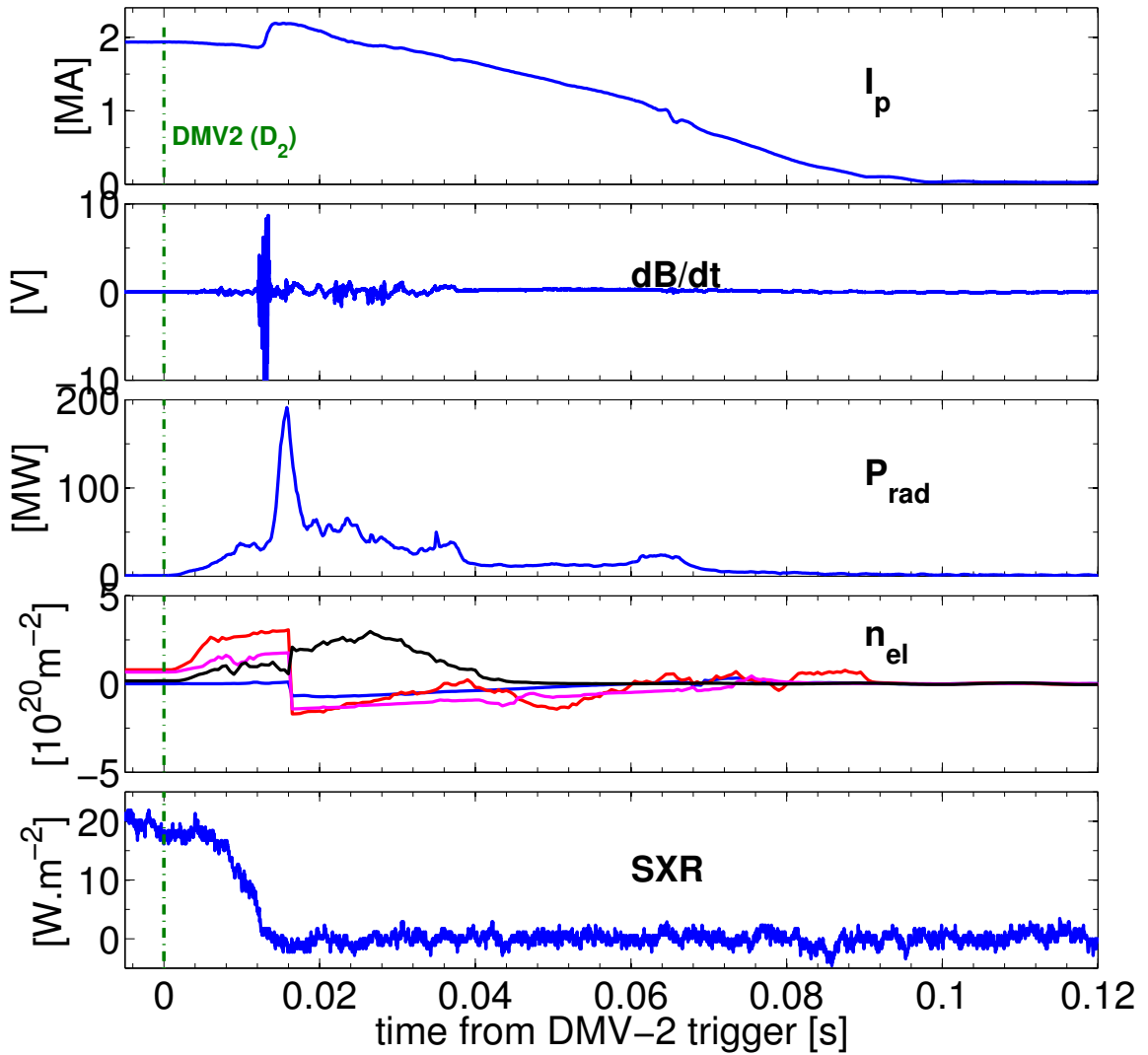


Figure 6.7: *Experimental time traces, from top to bottom: plasma current I_p , magnetic fluctuations from Mirnov coil H302, radiated power from bolometry, line integrated density from interferometry (valid until about 10 ms) and soft X-rays signal from a central chord. The time origin corresponds to the DMV2 trigger.*

6.2.2 Simulation set-up

In the simulations presented here, the initial value of the resistivity η at the centre of the plasma is $\eta_0 = 10^{-7}$ in JOEREK units, i.e. $\eta_{0,SI} = 3.5 \times 10^{-7} \Omega \cdot \text{m}$. The experimental Spitzer value^b is about $2 \times 10^{-8} \Omega \cdot \text{m}$, i.e. a factor 17.5 smaller than the simulation value. The temperature dependency of η is taken into account in JOEREK by using $\eta = \eta_0 \cdot (T_0/T)^{3/2}$, where T_0 is the initial temperature at the centre of the plasma. A rather large hyper-resistivity is also used in these simulations for numerical stability purposes, whose influence will be studied in section 6.2.6.

The parallel heat conductivity used in the simulations is $\kappa_{\parallel 0} = 800$ in JOEREK units, i.e. $\kappa_{\parallel 0,SI} = 6.7 \times 10^{28} \text{ m}^{-1} \text{ s}^{-1}$. The experimental Spitzer-Härm value^c is $6.9 \times 10^{29} \text{ m}^{-1} \text{ s}^{-1}$, i.e. a factor 10 larger than in the simulation. Similarly to the resistivity, κ_{\parallel} depends on the temperature: $\kappa_{\parallel} = \kappa_{\parallel 0} \cdot (T/T_0)^{5/2}$. The perpendicular heat conductivity is $\kappa_{\perp 0} = 5 \cdot 10^{-7}$ in JOEREK units, i.e. $\kappa_{\perp 0,SI} = 4.2 \times 10^{19} \text{ m}^{-1} \text{ s}^{-1}$ which corresponds to a χ_{\perp} typical of turbulent transport (of the order of $1 \text{ m}^2 \cdot \text{s}^{-1}$).

For the viscosity we use, in JOEREK units, $\mu = 10^{-6}$ and $\mu_{\parallel} = 10^{-4}$, i.e. $\mu_{SI} = 2.8 \cdot 10^{-7} \text{ kg} \cdot \text{m}^{-1} \cdot \text{s}^{-1}$ and $\mu_{\parallel,SI} = 2.8 \cdot 10^{-5} \text{ kg} \cdot \text{m}^{-1} \cdot \text{s}^{-1}$ and a temperature dependency of the perpendicular viscosity is taken into account, using $\mu_{\perp} = \mu_{0\perp} \cdot (T/T_0)^{-3/2}$. Typical particle diffusivities used in the simulations are $D_n = 10^{-2}$, $D_{\perp} = 10^{-5}$ and $D_{\parallel} = 10^{-2}$ in JOEREK units, i.e. $D_{n,SI} = 2.8 \times 10^4 \text{ m}^2/\text{s}$, $D_{\perp,SI} = 28 \text{ m}^2/\text{s}$ and $D_{\parallel,SI} = 2.8 \times 10^4 \text{ m}^2/\text{s}$. The choice of these values is dictated mainly by numerical stability reasons. Indeed, particle diffusion tends to smooth gradients and helps prevent numerical instabilities. In the absence of a first principles model for neutrals transport, it is not clear what a realistic value of D_n would be (in fact, a diffusive model may not even be appropriate). As for D_{\perp} , a typical value representative of turbulent transport would be $1 \text{ m}^2/\text{s}$, a factor 28 smaller than in the simulation. Finally, D_{\parallel} has no physical origin and is used only for numerical stability reasons. Efforts are currently made by the JOEREK community in order to overcome these numerical issues, including generalized finite elements, Taylor-Galerkin stabilization and an improved treatment of the grid center. Section 6.2.6 will discuss the influence of these parameters, in particular the impact of the resistivity and of D_{\perp} on the simulation results.

6.2.3 Overdensity created by the MGI

After solving the equilibrium as presented in section 4.4.1, the MGI is triggered by turning on the volumetric source term S_n appearing in Eq. 4.61.

The following expression is used:

$$S_n = \frac{dM_n}{dt}(t) \cdot \frac{f(R, Z, \phi)}{\int f dV} \quad (6.4)$$

^bJ. Wesson 2004.

^cJ. Wesson 2004.

6.2. Toward code validation and quantitative comparison with experiments

with the spatial shape of the source set as:

$$f = \exp\left(-\frac{(R - R_{MGI})^2 + (Z - Z_{MGI})^2}{\Delta r_{MGI}^2}\right) \cdot \exp\left(-\left(\frac{\phi - \phi_{MGI}}{\Delta\phi_{MGI}}\right)^2\right) \quad (6.5)$$

Here, $(R_{MGI}, Z_{MGI}, \phi_{MGI}) = (3.8 \text{ m}, 0.28 \text{ m}, 4.51 \text{ rad})$ is the position where neutrals from the JET DMV-2 are assumed to be delivered into the plasma and $\Delta r_{MGI} = 4 \text{ cm}$ and $\Delta\phi_{MGI} = 0.6 \text{ rad}$ are the assumed poloidal and toroidal extensions of the neutral source. Note that the value of $\Delta\phi_{MGI}$ is constrained by the number of toroidal harmonics n_{tor} included in the simulation (itself constrained by the code memory consumption), the real value being probably smaller than 0.6 rad.

The normalization by $\int f dV$ in Expression 6.4 ensures that the total mass of neutrals injected per time unit is equal to $\frac{dM_n}{dt}$. The parameterization of $\frac{dM_n}{dt}$ is based on laboratory experiments and modeling of the DMV reported in [Bozhenkov, Lehnen, et al. 2011]. After the valve opening, the gas travels inside a guiding tube of length $L_{tube} = 2.36 \text{ m}$ and cross-sectional area $A_{tube} = 1.8 \times 10^{-2} \text{ m}^2$, which is much larger than the valve orifice area. It is shown in [Bozhenkov, Lehnen, et al. 2011] and in section 5.3 of this thesis that this situation is well described with the 1D Euler equations, whose solution is a so-called "rarefaction wave". The forefront of this wave travels at a velocity of $3 \cdot c_s$, where c_s is the gas sound speed at the reservoir temperature. In the present case, $c_s = 923 \text{ m/s}$ and it therefore takes $t_0 = \frac{L_{tube}}{3c_s} \simeq 0.9 \text{ ms}$ for the first gas particles to arrive at the exit of the tube and enter the vacuum vessel through the midplane port of Octant 3.

$\frac{dN_n}{dt} = \frac{1}{m_{D_2}} \frac{dM_n}{dt}$ is represented in Figure 6.8. Before $t = t_0$, $\frac{dM_n}{dt} = 0$.

Then, for $t_0 < t < t_1$, the mass of gas entering the vessel per unit time is:

$$\frac{dM_n}{dt}(t) = \rho_{0_{DMV2}} A_{tube} K L_{tube} \frac{m^m}{(m+1)^{m+1}} \sum_{k=0}^{m+1} \frac{(-1)^{k-1} (m+1)!}{(m-k+1)! k!} (k-1) \left(\frac{L_{tube}}{c_s m}\right)^{k-1} (t)^{-k} \quad (6.6)$$

where $\rho_{0_{DMV2}} = m_{D_2} P_{DMV2} V_{DMV2} / (k_B T_{DMV2})$ is the initial mass density in the DMV2 reservoir, K is a factor calculated from laboratory experiments which depends mainly on the ratio of the valve orifice area to the tube area A_{tube} , and $m = 2/(\gamma - 1)$, where $\gamma = c_p/c_v$ is the ratio of specific heats ($m = 5$ for D_2). t_1 corresponds to the moment when the time integral of $\frac{dM_n}{dt}$ is equal to the mass of gas initially contained in the reservoir and logically, $\frac{dM_n}{dt} = 0$ for $t > t_1$ (this sharp cut at $t = t_1$ is an approximation of the model, in reality $\frac{dM_n}{dt}$ is continuous). A fit of IMAGINE results presented in Figure 5.3 taking into account the reservoir depletion could easily be used in the near future. As the MGI is turned on, the neutral density ρ_n increases and takes a spatial distribution similar to that of the source S_n , as shown in Figure 6.9. After a fast transient increase, ρ_n becomes approximately stationary, which indicates that an equilibrium is established between sources, sinks and transport terms in Eq. 4.61. The stationary neutral density at the injection location is on the order of 10^{19} m^{-3} .

The ionization of neutrals causes a local increase in plasma density, as can be seen in Figure 6.10. The density at the location where neutrals are deposited reaches several

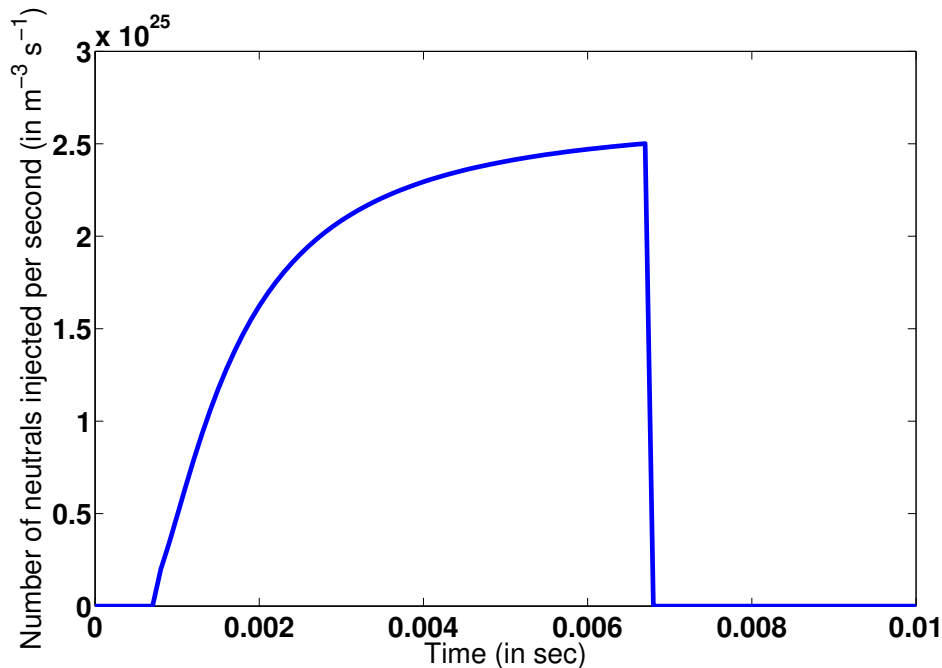


Figure 6.8: Number of D_2 molecules injected per time unit into the JET vacuum vessel by DMV2 pre-loaded with D_2 at 5bar, according to [Bozhenkov, Lehnen, et al. 2011]

times 10^{20} m^{-3} . This is accompanied by a cooling of the edge of the plasma, also visible on Figure 6.10.

Figure 6.11 shows that the overdensity expands in the parallel direction. In the simulations, parallel diffusion and convection contribute about equally to this expansion, but it should be kept in mind that parallel diffusion is present only for numerical stability reasons. In reality, the expansion should be purely convective. The origin of the convective expansion is worth being discussed. One can see in Figure 6.12 that a structure of v_{\parallel} is created by the MGI, with $v_{\parallel} \mathbf{b}$ pointing away from the overdensity. This parallel flow is presumably driven by a pressure gradient resulting from the heating by parallel thermal conduction of the overdense region faster than its cooling by energy loss terms related to atomic physics. A similar phenomenon is observed in JOREK pellet injection simulations^d.

The current model for neutrals in JOREK does not take into account IMAGINE results, and the Bozhenkov formulae (valid only at the vacuum tube exit) completely ignores these mechanisms.

It is thus important to set simulation parameters such that the increase in n_e be consistent with experimental observations. In order to do this, we use synthetic interferometry. In JET, the interferometer is installed 180° away toroidally from DMV2 (see Figure 6.13). Figure 6.14 shows experimental and simulated line-integrated densities for Lines of Sight (LoS) 2, 3 and 4 of the interferometer (see Figure 6.13 to visualize their location). Three simulations are shown, with $P_{DMV2} = 1, 2$ and 5 bar respectively. Although it does not go very far, the simulation with the experimental pressure $P_{DMV2} = 5$ bar gives a too large

^dFutatani, G. Huijsmans, et al. 2014.

6.2. Toward code validation and quantitative comparison with experiments⁸³

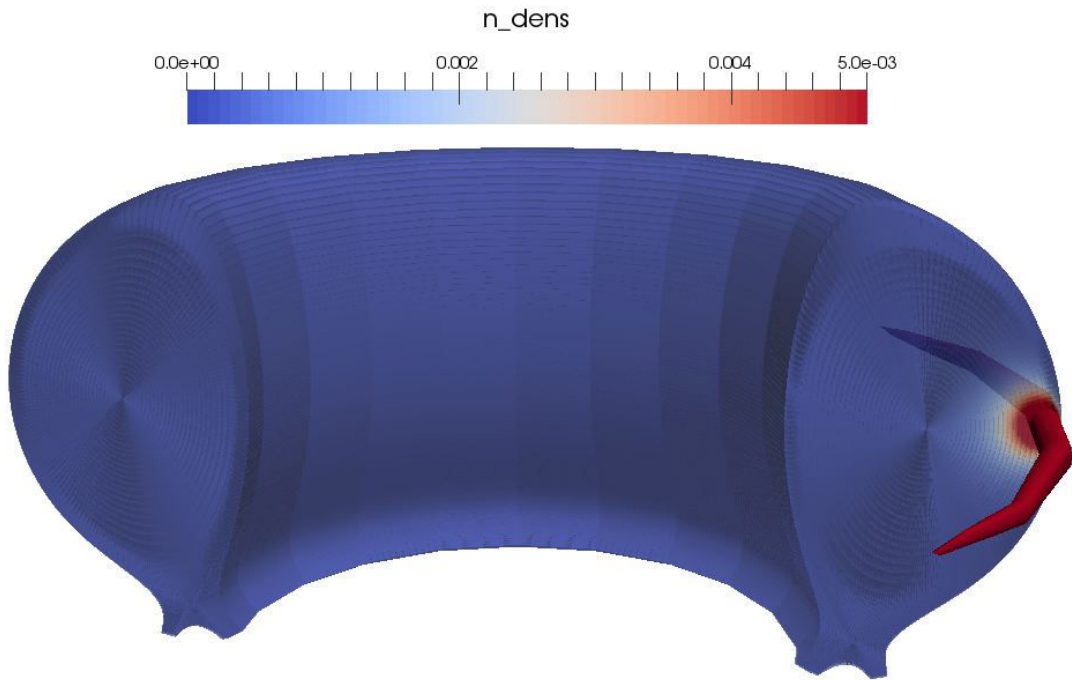


Figure 6.9: *Neutral density at the beginning of the MGI, in JOREK units*

increase when $P_{DMV2} = 1$ or 2 bar give a better match. This is remindful of experimental observations on the mixing efficiency of MGI (defined as the number of atoms delivered to the plasma divided by the number of atoms that have entered the vessel at a given time) which has been found of the order of a few tens of % in a range of experiments⁸. The simulations described in detail in the following use $P_{DMV2} = 1$ bar. Looking at Figure 6.14, LoS 2 and 3, which are rather central, are moderately well matched with $P_{DMV2} = 1$ or 2 bar while for LoS 4, which goes through the edge of the plasma, the simulated value is much lower than the measured one. We found that reducing D_{\perp} improves the overall match on the three LoS (see section 6.2.6), however, as stated above, it tends to cause numerical instabilities. Using a lower P_{DMV} than in the experiment is not surprising considering the IMAGINE results, i.e. that only a fraction of the injected gas actually penetrates into the plasma.

⁸Bozhenkov, Lehnen, et al. 2011.

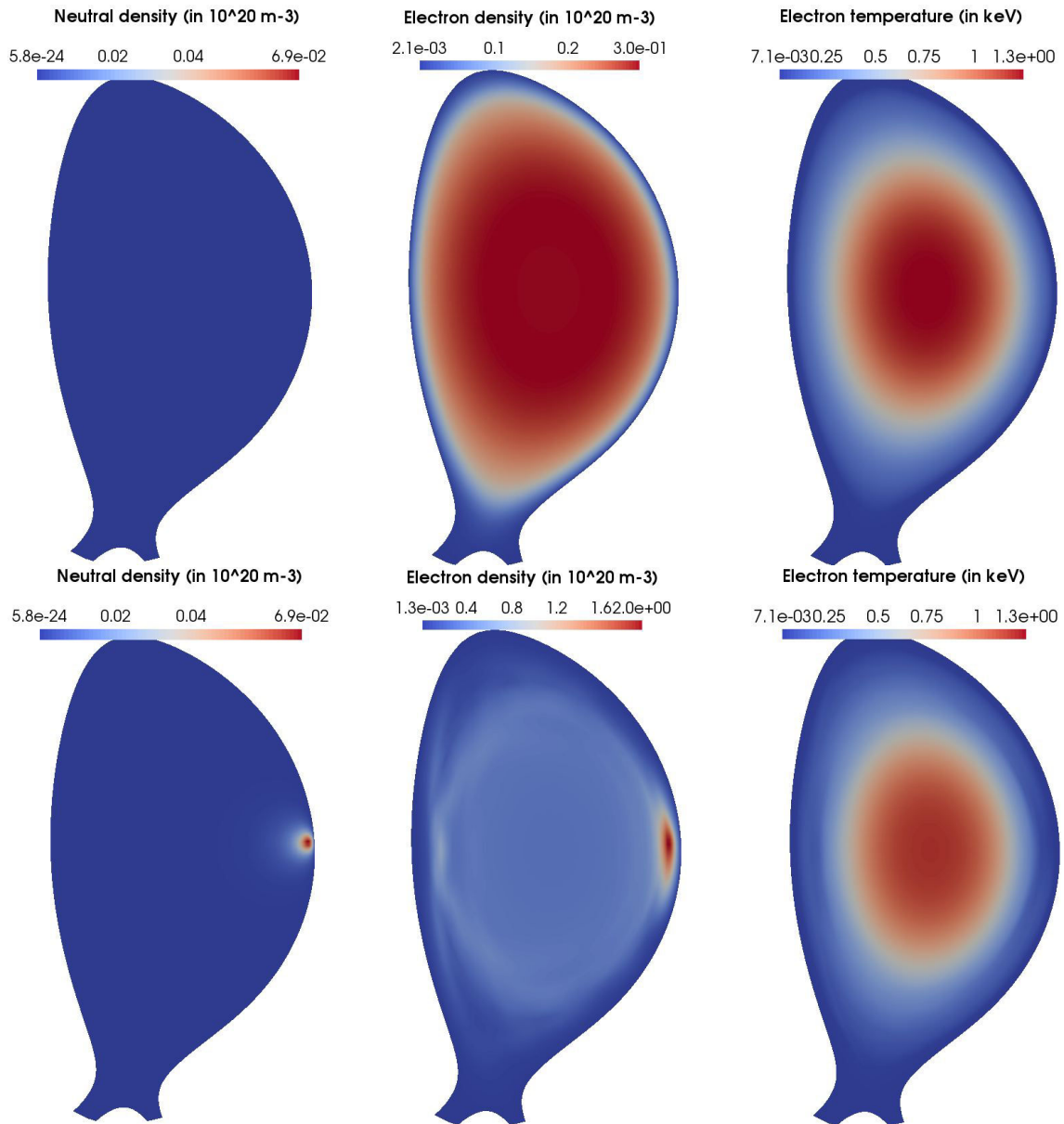


Figure 6.10: Poloidal cross-sections, in the plane of the gas entry point, before (top row) and during (bottom row) the MGI, of the neutral density (left column), electron density (middle column) and electron temperature (right column)

6.2. Toward code validation and quantitative comparison with experiments

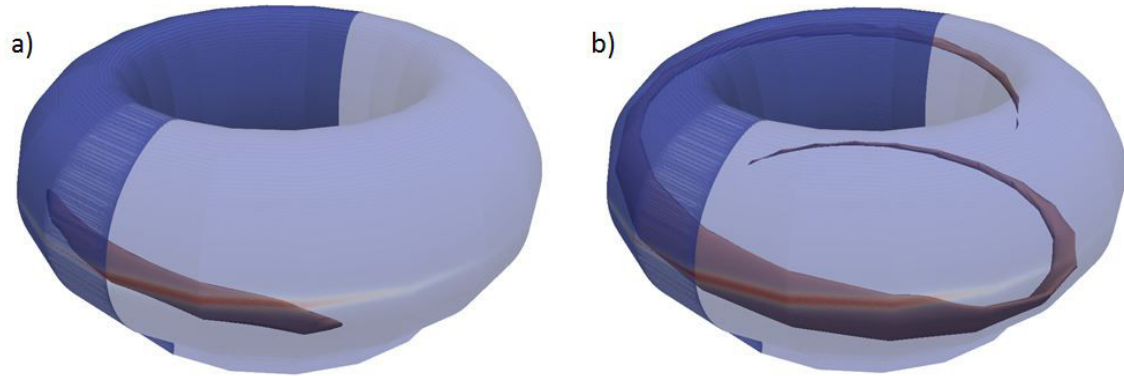


Figure 6.11: *Isocontours of the electron density at a) $t = 0.55 \text{ ms}$ and b) $t = 0.76 \text{ ms}$, showing the parallel expansion of the overdensity created by the MGI*

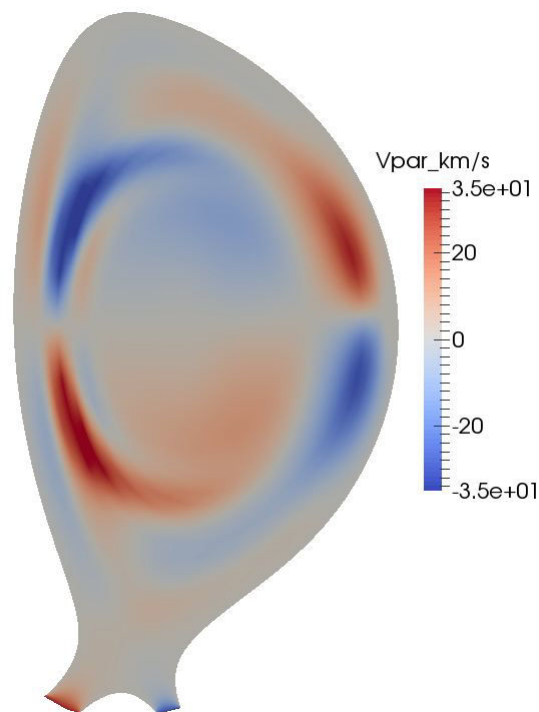


Figure 6.12: *Poloidal cross-section, in the plane of the gas entry point, of the parallel velocity*

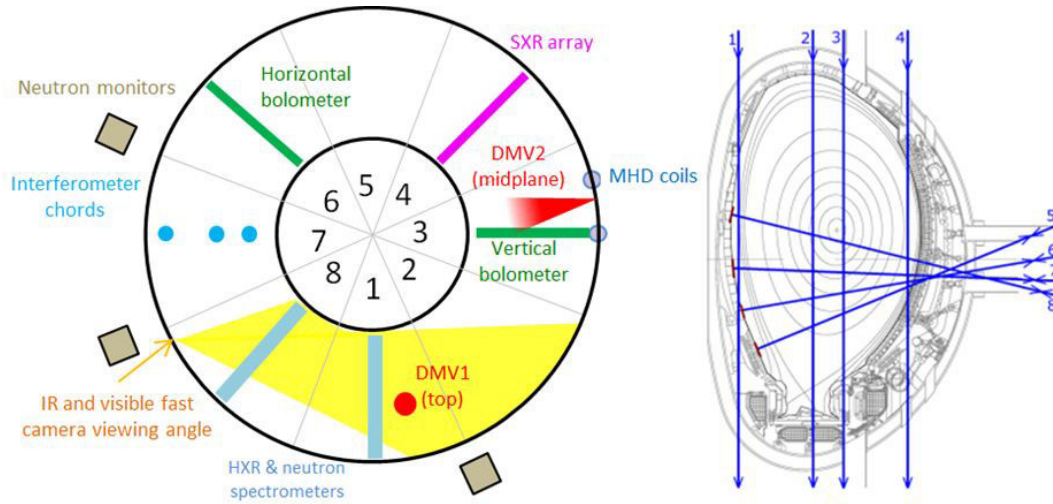


Figure 6.13: Left: Location of diagnostics, DMVs and octant numbers in JET, seen from the top. Right: Interferometer lines of sight

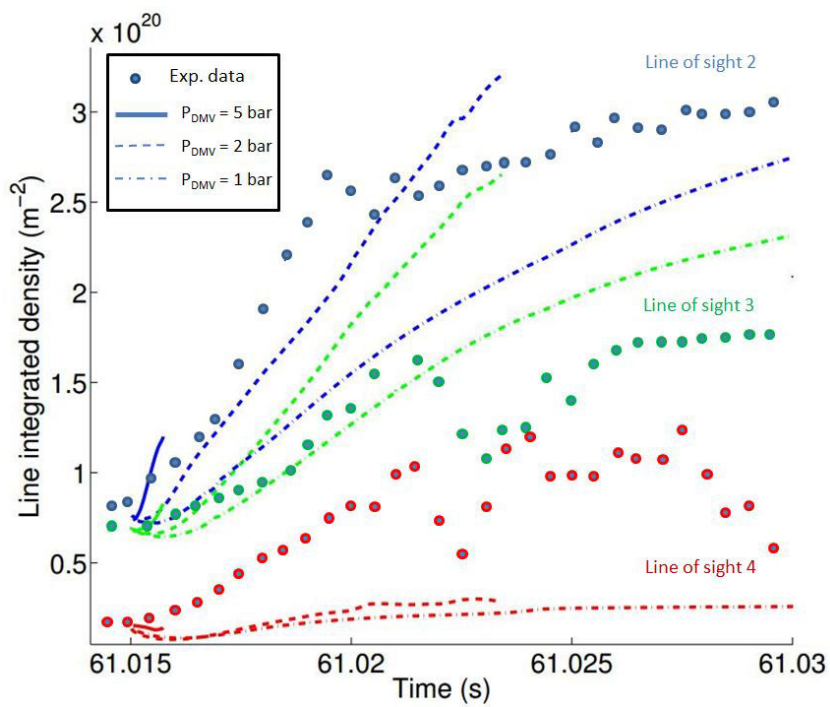


Figure 6.14: Experimental and simulated interferometry measurements for 3 lines of sight, with a scan of P_{DMV} in the simulations

6.2.4 MHD instabilities triggered by MGI

We now describe the MHD activity caused by the MGI. A particular focus is given on the role of the initial safety factor on the magnetic axis, q_0 . The value given by EFIT 10 ms before the MGI is $q_0 = 0.78$. The fact that $q_0 < 1$ is consistent with the presence of sawteeth in this discharge. However, EFIT is not constrained by polarimetry nor motional Stark effect measurements in this pulse, thus the value of q_0 should be taken with caution. Therefore, simulations have been run with 3 values of q_0 : 0.75, 0.94 and 1.04. This was done by changing the j_{mean} profile while keeping I_p (almost) constant. From SXR measurements, the sawtooth inversion radius (which should give the position of the $q = 1$ surface) is about $r/a = 0.3$ in the sawteeth preceding the MGI. The $q_0 = 0.94$ case has the $q = 1$ surface near this radius and may therefore be considered as the most realistic case. The simulations presented in this section all have $P_{DMV2} = 1$ bar. The case with $q_0 = 0.75$ has an initial central resistivity (in JOEREK units) of $\eta_0 = 10^{-7}$ while the other cases have $\eta_0 = 10^{-8}$. However, a large resistivity is also used and therefore the effective resistivity is $\eta_{eff} \simeq 10^{-6}$ in JOEREK units. Figures 6.15, 6.16 and 6.17 display time traces of the magnetic energies in the different toroidal harmonics in the three simulations (note the different time axes).

In all cases, a fast increase of the magnetic energies of all toroidal harmonics can be

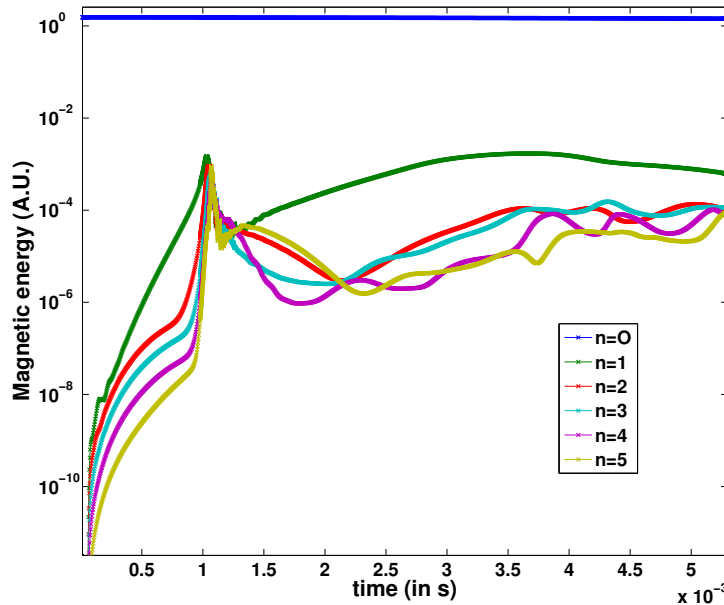


Figure 6.15: *Magnetic energies in the different toroidal harmonics for the simulation with $q_0 = 0.75$*

observed during the first millisecond or so. This increase is associated to the growth of magnetic islands, mainly $m/n = 2/1$, $3/2$ and $1/1$ (the latter only for cases with $q_0 < 1$), all of which are visible in the Poincare cross-sections shown in Figure 6.18. The $1/1$ mode (for simulations with $q_0 < 1$) is different from other modes because it is unstable even

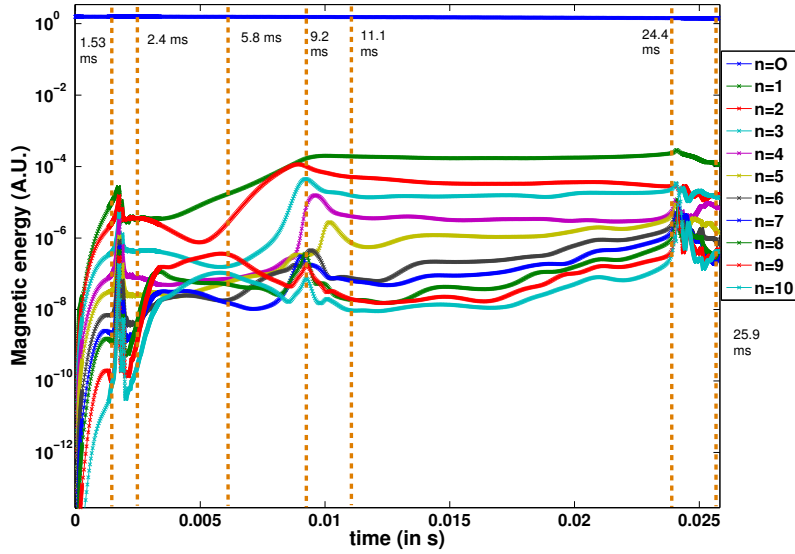


Figure 6.16: *Magnetic energies in the different toroidal harmonics for the simulation with $q_0 = 0.94$*

without MGI (as one would expect), as can be seen in Figure 6.19, which compares the magnetic energy in the $n = 1$ harmonic for cases with and without MGI. The energy grows in both cases but in the case without MGI, it starts from a very low level (numerical noise) and hence takes much longer to reach a significant amplitude, while in the other case it is seeded by the MGI and takes a much larger value from the beginning of the simulation. It can be observed in Figure 6.18 that O-points of all island chains are located at the outer midplane ($\theta = 0$), i.e. in front of the MGI. This is consistent with experimental observations based on measurements with the set of saddle loops. Note that NIMROD simulations also find that the O-point of the 1/1 mode is in front of the MGI location^f. Although a detailed analysis would be needed in order to understand what happens during this first phase of the simulations, the simultaneous growth of the energies of all harmonics suggests that the MGI drives the modes by directly imposing a 3D structure rather than by making the axisymmetric profiles unstable. A possible mechanism may be that the local cooling caused by the MGI reduces the toroidal current density j locally through an increased resistivity. The missing current would then cause the appearance of magnetic islands, with O-points at the position of the missing current (as in neoclassical tearing modes). The same current perturbation would also cause a magnetic perturbation $\delta\mathbf{B}$ in the core of the plasma which would give rise to a $\mathbf{j} \times \delta\mathbf{B}$ force pointing away from the MGI deposition region, consistently with the observed phase of the 1/1 mode. This simple picture has the interest of being consistent with the observed spatial phase of the modes, however a close look at the simulations results indicates that the reality is probably more complex. Another possibly important mechanism, for example, is that the MGI creates a 3D perturbation in the pressure field, to which \mathbf{j} and \mathbf{B} have to adapt in order for force

^fIzzo 2013.

6.2. Toward code validation and quantitative comparison with experiment⁸⁹

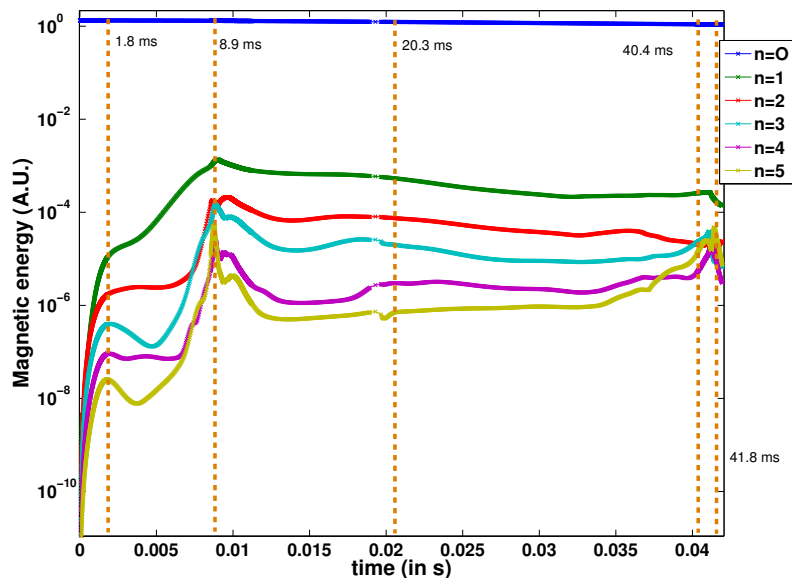


Figure 6.17: *Magnetic energies in the different toroidal harmonics for the simulation with $q_0 = 1.04$*

balance to pertain.

In simulations with $q_0 < 1$, a crash of the 1/1 mode can be observed at $t \simeq 1.2$ ms ($q_0 = 0.75$) and $t \simeq 1.6$ ms ($q_0 = 0.94$) (see Figures 6.15 and 6.16). The crash is preceded by a fast growth of high n harmonics, all harmonics reaching a comparable amplitude at the time of the crash, which is typical of the non-linear phase of the internal kink mode⁸. It is interesting to compare simulations and experiment in terms dB/dt measurements from Mirnov coils. This is done in Figure 6.20, where it appears that the burst of dB/dt in the experiment is 13 ms after the DMV2 trigger, which is much later than the crash of the 1/1 mode in the simulations. It is not clear experimentally whether there exist signs of a 1/1 mode crash near the same time as in the simulations. What is clear is that fluctuations on the same order as in the $q_0 = 0.75$ simulation are not observed at this time. As stated above, the inversion radius of sawteeth is consistent with the $q_0 = 0.94$ case, while the $q_0 = 0.75$ has the $q = 1$ surface much further out. The fact that the latter case produces very large magnetic fluctuations which are not observed experimentally is therefore not surprising and merely confirms that this case is not realistic. In the following, we will therefore focus on the $q_0 = 0.94$ and $q_0 = 1.04$ cases.

The second phase of the simulations, between 2 and 10 ms roughly, is characterised by a slower evolution of the magnetic energies. Taking a close look at Figures 6.16 and 6.17, one can see that after a short plateau-like phase between 2 and 3 ms, the $n = 1$ energy starts to increase again. Higher n harmonics follow. In the $q_0 = 0.94$ case in particular, it is interesting to see that $n = 2, 3, 4$ and 5 harmonics start to grow successively. This growth is associated to an increase in the width of magnetic islands which leads to the

⁸Biskamp 2004; Nicolas 2013.

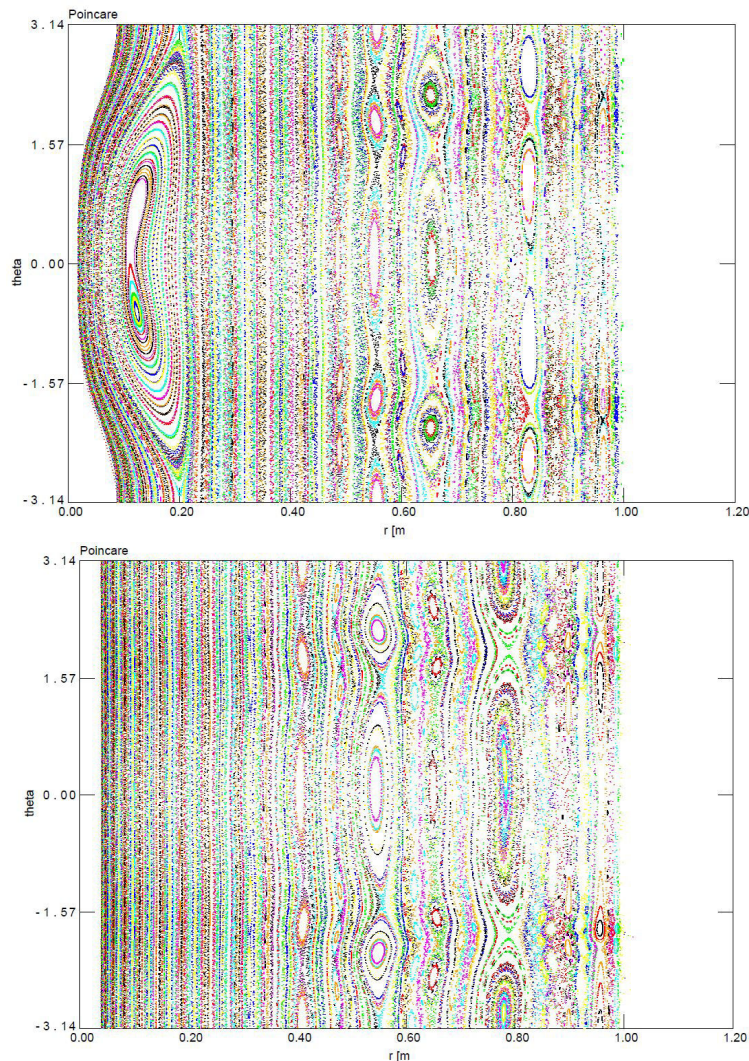


Figure 6.18: *Poincaré cross-sections after 1.53 ms for the $q_0 = 0.94$ case (top) and after 1.8 ms for the $q_0 = 1.04$ case (bottom)*

formation of a stochastic layer at the edge of the plasma and to small scale structures visible, for example, on j (see Figure 6.21). A peak of MHD activity is reached around 9 ms (see Figures 6.16 and 6.17). The non-simultaneous growth of the energies in the different harmonics, which contrasts with the first phase of the simulations, suggests that in this second phase, the growth of the modes is due to the axisymmetric profiles becoming unstable. An often described picture^h is that MGI contracts the current channel by cooling the edge of the plasma, making it more resistive. The loss of current at the edge induces current in the still hot region inside the cold front, creating a large current gradient which can strongly drive tearing modes, especially when it is located just inside low order rational surfaces, for example $q = 2$. This effect has been found in the JOREK simulation presented in the previous section, leading to the TQ (also in [Fil, Nardon, et al. 2014]). In the present simulations, this mechanism is probably at play too. The

^hBiskamp 2004.

6.2. Toward code validation and quantitative comparison with experiment 01

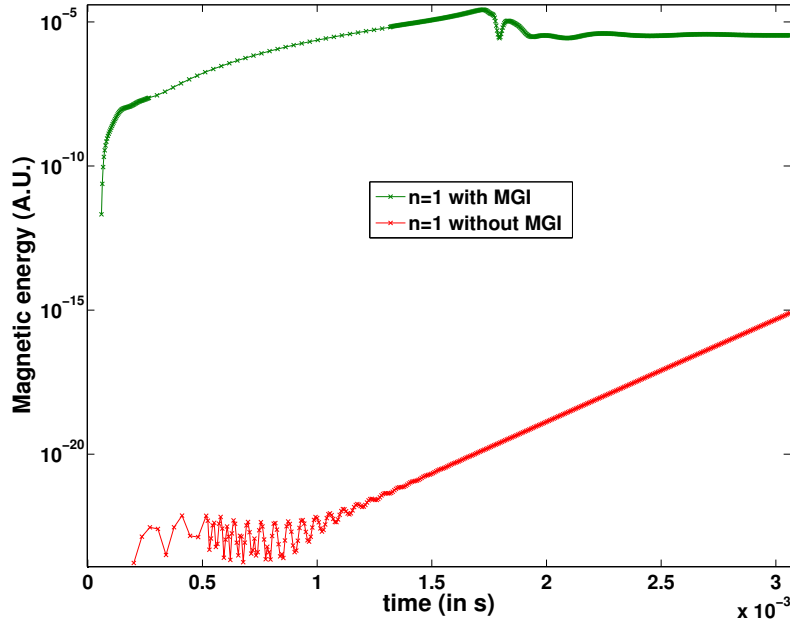


Figure 6.19: *Magnetic energy of the toroidal harmonic $n = 1$ for the simulation with $q_0 = 0.94$, with and without MGI*

successive growth of the $n = 1, 2, 3, 4$ and 5 harmonics in the $q_0 = 0.94$ case may be due to the successive destabilization of the $2/1, 3/2, 4/3, 5/4$ and $6/5$ modes as the cold front penetrates inward. Looking at the plasma current (Figure 6.22), a small spike appears at $t \simeq 10$ ms in the $q_0 = 1.04$ simulation. At the same time, a burst of magnetic fluctuations is visible for this simulation (see Figure 6.20). On the other hand, neither the I_p spike nor the burst in dB/dt are distinguishable in the simulation with $q_0 = 0.94$, which is probably related to the smaller extent of the stochastic layer and smaller magnetic energies in this case. Experimentally, both the I_p spike and the dB/dt burst are observed at about the same time as in the $q_0 = 1.04$ simulation, which is encouraging, but they are about one order of magnitude larger, indicating that the MHD activity in the simulations is much smaller than in the experiment. Reasons for this discrepancy will be discussed in section 6.2.6.

The third and last phase of the simulations is characterized by a much slower evolution of the energies for a few tens of millisecond, until a small burst of activity happens at $t \simeq 23$ ms for $q_0 = 0.94$ and $t \simeq 41$ ms for $q_0 = 1.04$. This burst is associated to the crash of a $1/1$ mode which can come into existence due to an increase in j and drop in q at the center of the plasma.

Figure 6.23 displays the time evolution of the central T_e and pressure for the simulations with $q_0 = 0.94$ and $q_0 = 1.04$. T_e drops from about 1.2 keV to about 500 eV in the first 10 ms and then decreases in a much slower way, except for the fast drops corresponding to $1/1$ mode crashes. It can be seen that the pressure changes much less than T_e (see Figure 6.23). This is because the central cooling is mainly due to dilution, which is itself due to the perpendicular diffusion of the overdensity caused by the MGI. Indeed, a large

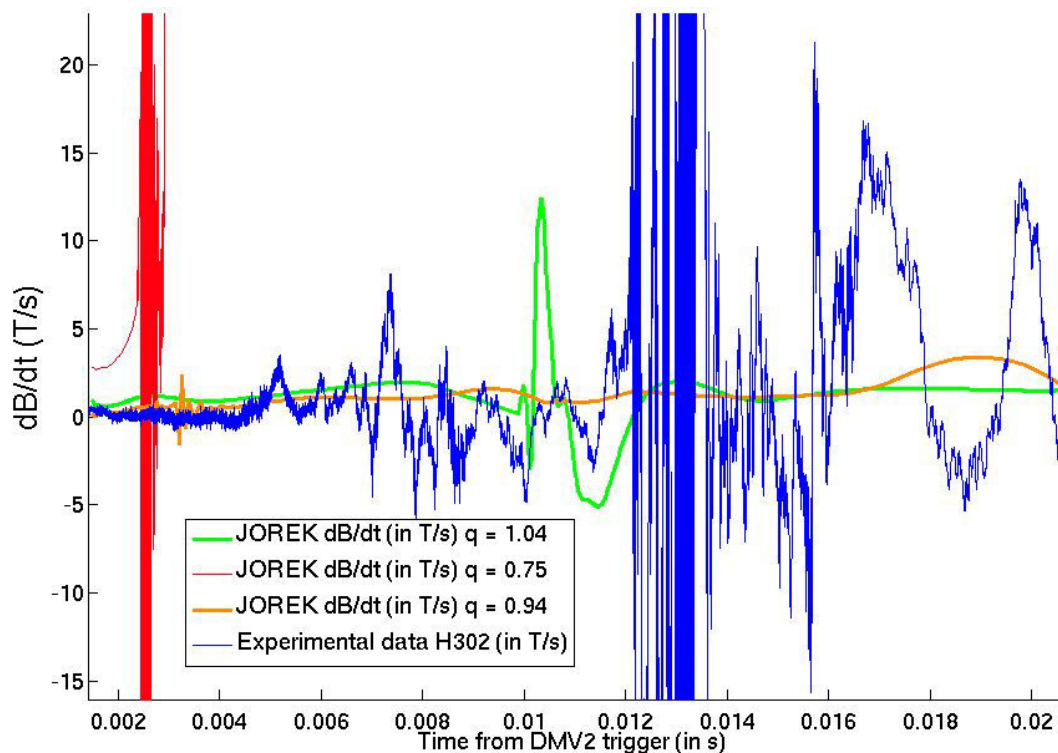


Figure 6.20: *Magnetic fluctuations: the red, orange and green curves are the JOREK output for the 3 simulations and in blue is the Mirnov coil (H302) experimental data. $t = 0$ s corresponds to the time of the DMV2 opening. The synthetic diagnostic is not fully realistic since the actual Mirnov coil (H302) is outside the JOREK computation domain. Also the ideal wall boundary conditions may reduce the simulated dB/dt , since the boundary of the JOREK domain is inside the actual wall.*

perpendicular diffusivity is used in these simulations: $D_{\perp,ST} = 28 \text{ m}^2/\text{s}$, hence the typical particle diffusion time across the plasma is on the order of 10 ms.

The fact that T_e does not go below a few hundreds of eV in the simulations shows that the TQ is not fully reproduced. This is not surprising since, as we saw above, the MHD activity is much weaker in the simulations than in the experiment. In particular, the stochastic region in the simulations is confined to the outer half of the plasma, while good flux surfaces remain in the inner half. Another possible cause for the incompleteness of the TQ in the simulations is a too low level of radiation, as we shall see in the next section.

Experimentally, no measurement of the central T_e is available (the Electron Cyclotron Emission diagnostic is in cut-off due to the high density) but the decrease of the SXR signal shown in Figure 6.7 may be considered as a sign of a decrease in core T_e , although this should be taken with caution because the link between the SXR signal and the core T_e is complicated and indirect. The experimental SXR decrease takes place on a timescale of about 10 ms, as in the simulations. The origin of this drop is unclear but dilution may also be involved. Since simulations and experiment approximately match in terms of interferometry signals, suggests that the experimental decrease in T_e may also be due, at

6.2. Toward code validation and quantitative comparison with experiment³

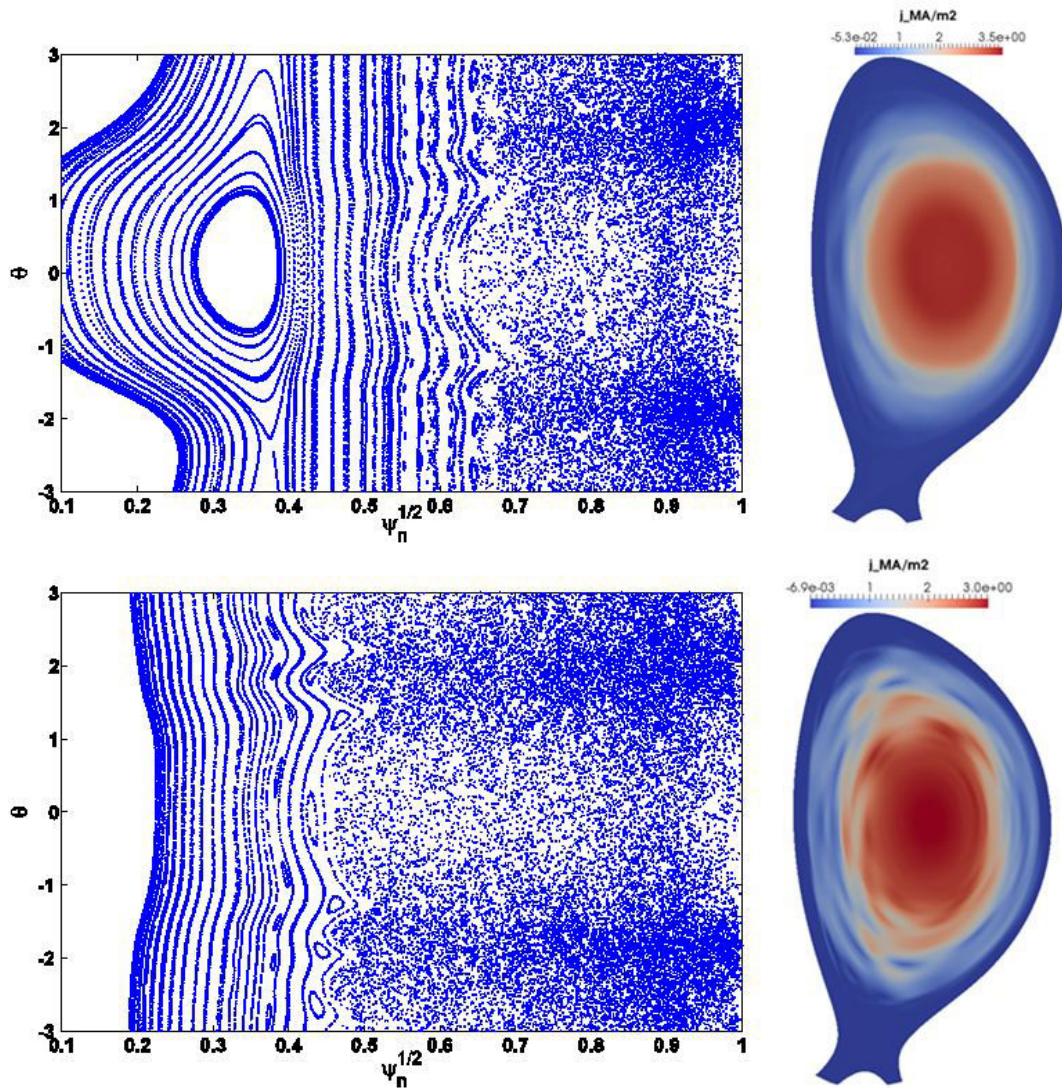


Figure 6.21: *Poincaré cross-section and current density at the peak of MHD activity for the simulations with $q_0 = 0.94$ (upper plots) at $t = 9.2$ ms and $q_0 = 1.04$ (lower plots) at $t = 8.9$ ms*

least partly, to dilution, although it should be kept in mind that interferometry does not directly give access to the local density at the plasma centre.

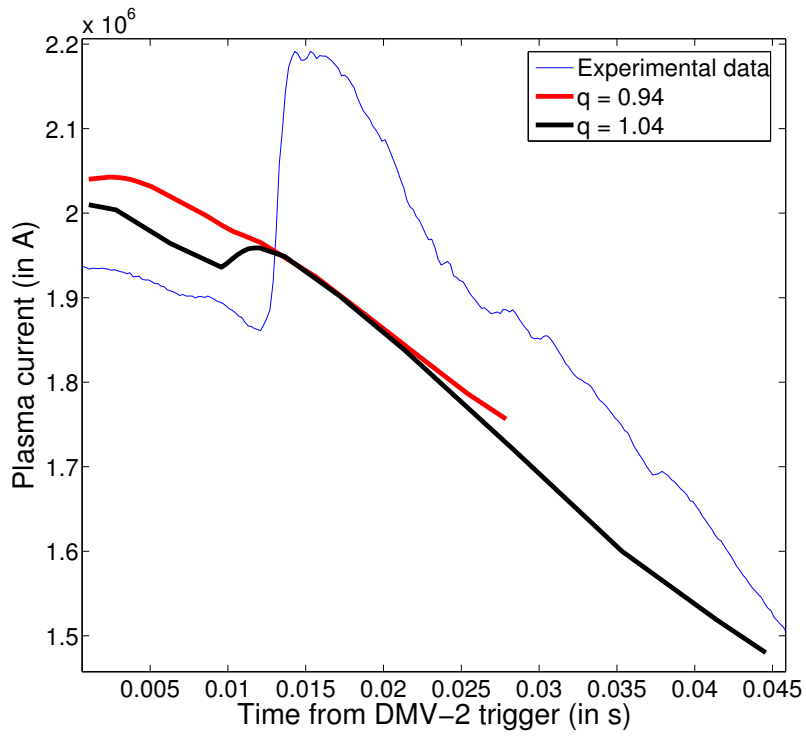


Figure 6.22: Total plasma current for $q = 0.94$ and $q = 1.04$ cases and comparison to the experiment

6.2. Toward code validation and quantitative comparison with experiment⁰⁵

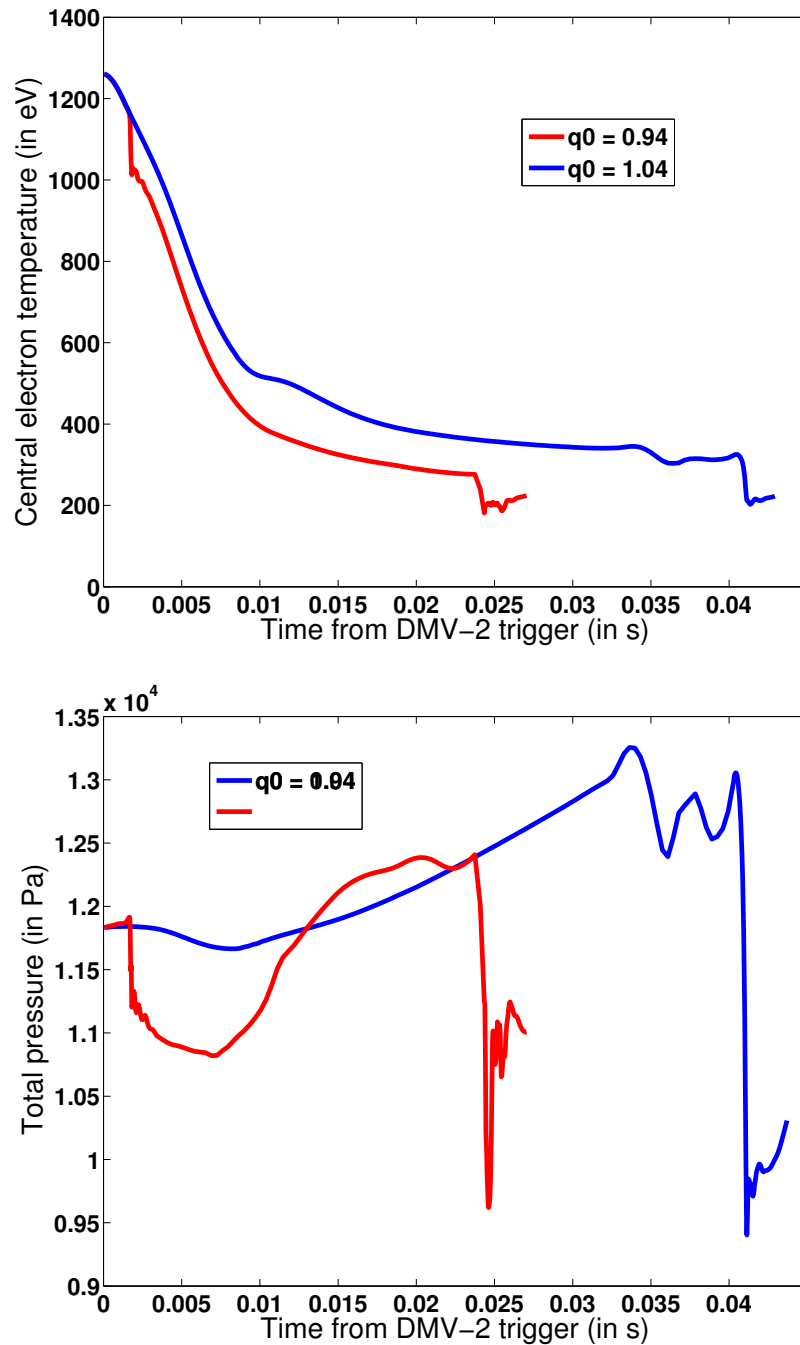


Figure 6.23: *Central electron temperature and central total pressure for $q = 0.94$ and $q = 1.04$ cases*

6.2.5 Radiation aspects

Another key aspect of MGI-triggered disruption physics is radiation. It is also a critical aspect of the design of the ITER DMS, since a too localized radiation could result in wall meltingⁱ. It is therefore important that simulations reproduce the measured radiation. The radiated power is measured at JET by two bolometer arrays, a vertical one located at the same toroidal angle as DMV2 and a horizontal one located 135° away from it toroidally. The position of the bolometers and their LoS are shown in Figures 6.13, 6.24 and 6.25. Figures 6.24 and 6.25 show the radiation measured by the vertical and horizontal bolometers, respectively, as a function of time and LoS poloidal angle. The first effects of the MGI are visible from $t = 7$ ms and a strong burst on virtually all LoS is visible at $t \simeq 15$ ms, corresponding to the spike in P_{rad} in Figure 6.7. The order of magnitude of the radiation measured by the bolometers is $1 \text{ MW} \cdot \text{m}^{-2}$ which, given that a typical chord length is 1 m, corresponds to a volumetric radiated power of $1 \text{ MW} \cdot \text{m}^{-3}$. It is interesting to speculate on the possible origin of this radiation. As shown in Figure 4.2, the bremsstrahlung (resp. D line) radiation rate function is of order $10^{-38} - 10^{-36} \text{ W} \cdot \text{m}^3$ (resp. $10^{-32} - 10^{-31} \text{ W} \cdot \text{m}^3$), meaning that in order to reach the observed level of radiated power, n_e (resp. $(n_e n_D)^{0.5}$) should be of order $10^{21} - 10^{22} \text{ m}^{-3}$ (resp. $1 - 3 \times 10^{19} \text{ m}^{-3}$). Given the observations presented in Section 6.2.3, it is unlikely that n_e rises enough for bremsstrahlung to make a significant contribution to the observed radiation. On the other hand, D line radiation cannot be excluded as a significant contributor in regions where $n_D > 10^{18} \text{ m}^{-3}$. Finally, the observed radiation may well come from impurities, an effect which is not included in the simulations.

Synthetic bolometers have been implemented in the JOREK code and the time evolution of the signal for each LoS is plotted in Figure 6.26 (for the simulation with $q_0 = 0.94$). Poloidal cross-sections of the bremsstrahlung and line radiated power in the toroidal plane of the bolometers are also plotted in Figure 6.27 to help understanding the simulation data. Experimentally, it can be noticed in Figures 6.24 and 6.25 that in the pre-TQ phase, patterns exist on the bolometry data. In particular, the horizontal bolometer (Figure 6.25) shows a clear peak near 212° and a smoother and smaller peak near 155°. The 212° (resp. 155°) LoS of the horizontal bolometer goes through the bottom (resp. top of the plasma) (see Figure 6.25). This observation may be compared to the simulated pattern of line radiation in the plane of the horizontal bolometer (bottom right plot in Figure 6.27), which also shows peaks in these regions (note that the line radiation peak at the outboard midplane is an artefact due to an insufficient toroidal localization of the neutral source), which are connected to the gas deposition region. The pre-TQ pattern measured by the vertical bolometer (Figure 6.24) is less clear but shows peaks near 262° and 282°. The 262° (resp. 282°) LoS goes through the center of the plasma and X-point region (resp. gas deposition region). In the simulations, a strong peak also exists near 282° which is dominated by line radiation in the gas deposition region where both neutral and ion densities are high (see bottom left plot in Figure 6.27). However, the peak near 262° is not present in the simulations. It therefore appears that simulations help interpret

ⁱLehnen, Aleynikova, et al. 2014.

6.2. Toward code validation and quantitative comparison with experiment^j

some, but not all, qualitative features of the measured pre-TQ radiation pattern.

Quantitatively speaking, there is a clear mismatch for the radiation measured in the plane of the horizontal bolometer (i.e. toroidally away from DMV2). Indeed, it can be seen in Figure 6.27 that simulated bremsstrahlung radiation in this plane is of order of a few $\text{kW} \cdot \text{m}^{-3}$ and that line radiation at the top and bottom of the plasma is even much smaller. This is by orders of magnitude smaller than measured levels (as seen comparing Figure 6.26 with Figures 6.25 and 6.24). We speculate that including a parallel convection term at the plasma velocity in the neutral transport equation (which may come from plasma-neutral friction by, e.g., charge exchange) would increase the line radiation in the top and bottom region and improve the match. This is planned for future work. At the location of the vertical bolometer (i.e. toroidally close to DMV2), the quantitative agreement is better in the sense that the simulated line radiation peak (see Figure 6.27), which is about $2 \text{ MW} \cdot \text{m}^{-3}$, has an order of magnitude compatible with the measured peak at 282° (see Figure 6.24).

Finally, the global radiation burst observed experimentally at $t \simeq 15 \text{ ms}$ on virtually all LoS (see Figures 6.24 and 6.25) is absent in the simulations.

P_{rad} , the total radiated power is one order of magnitude lower than in the experiment and the radiation burst observed in Figure 6.7 is not observed in the simulations.

These clear discrepancies may be due to an inappropriate gas transport model, but it seems more likely that they are due to the fact that impurities (either intrinsic or coming from the wall^j) are not included in the present model.

^jWard and J. A. Wesson 1992.

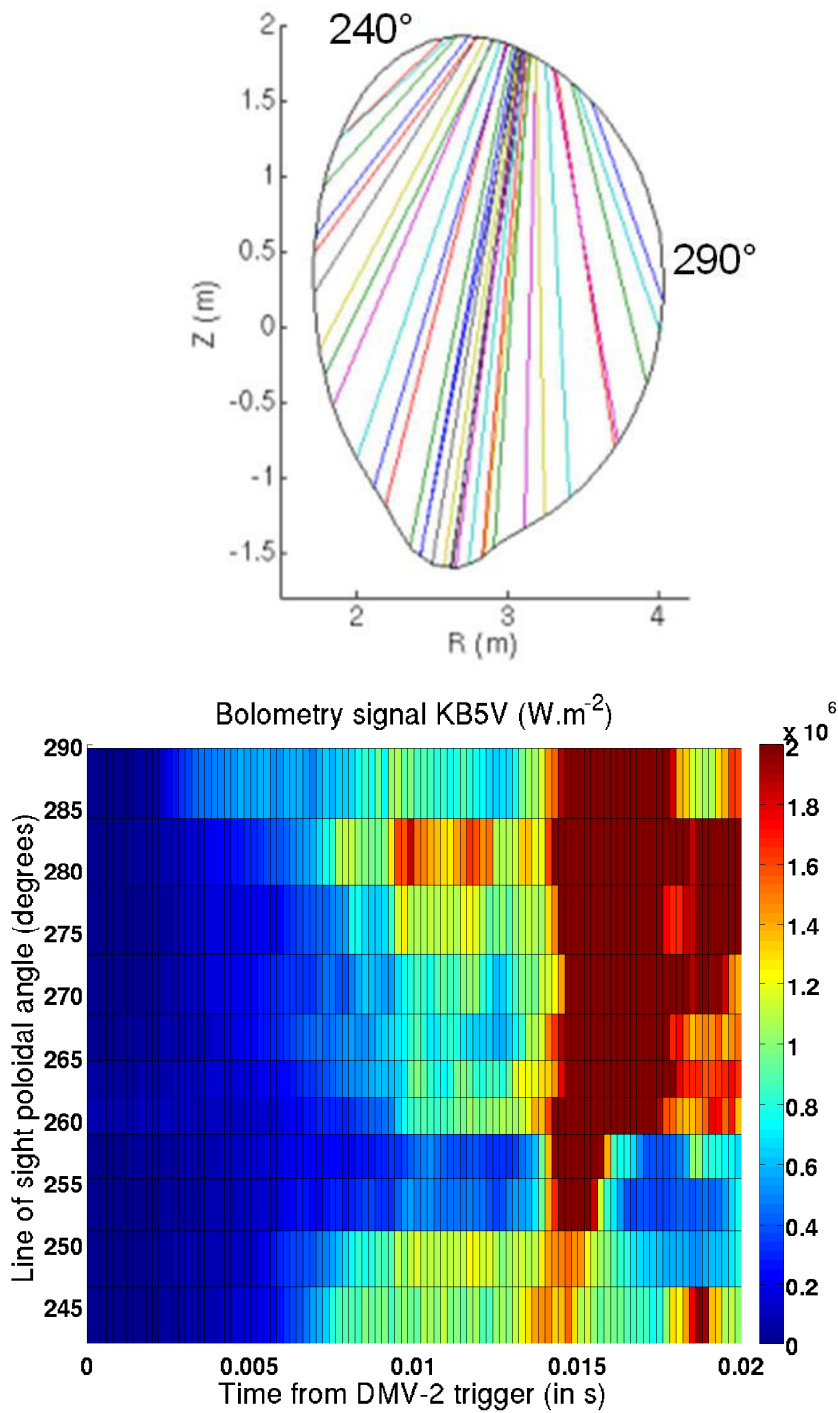


Figure 6.24: Vertical bolometer measurements

6.2. Toward code validation and quantitative comparison with experiment

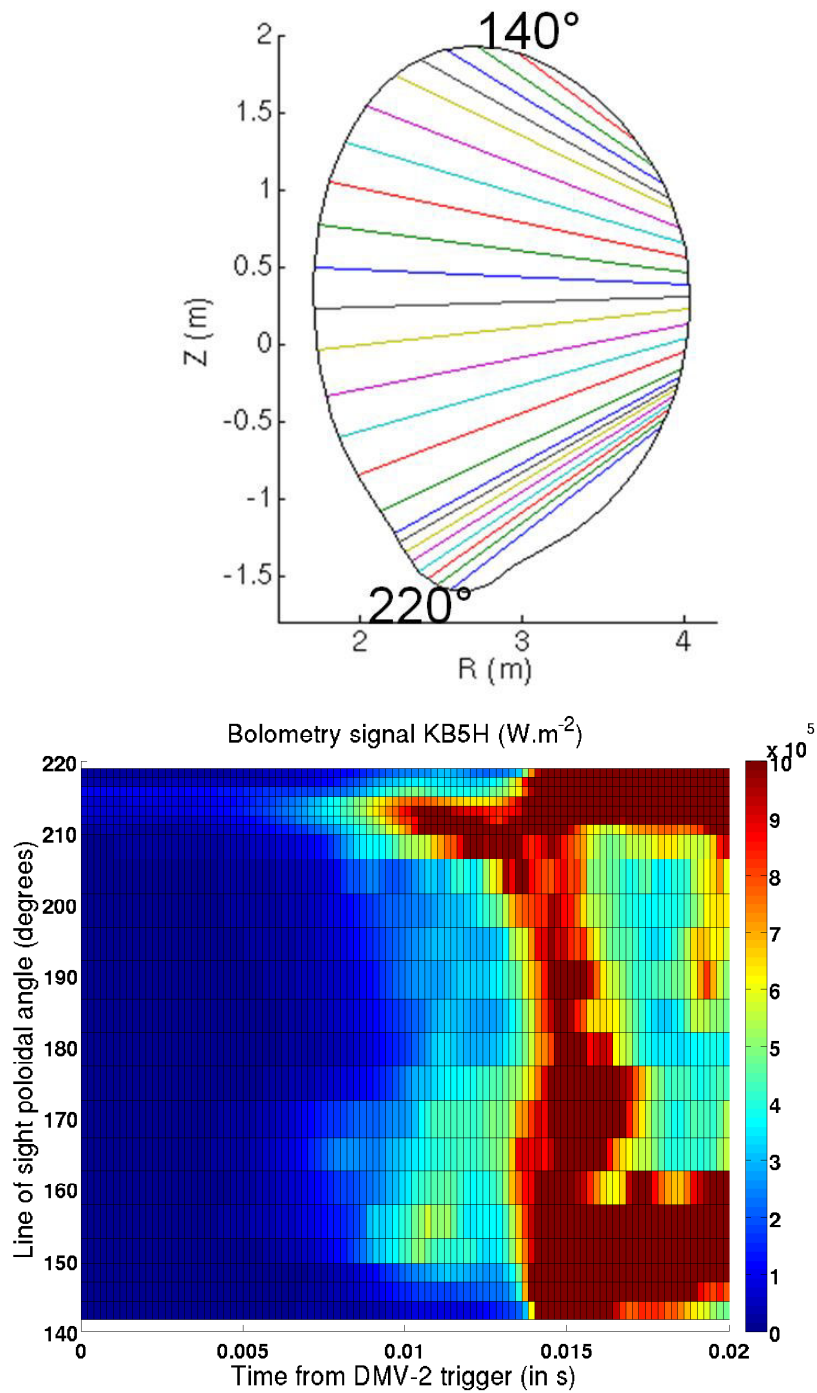


Figure 6.25: *Horizontal bolometer measurements*

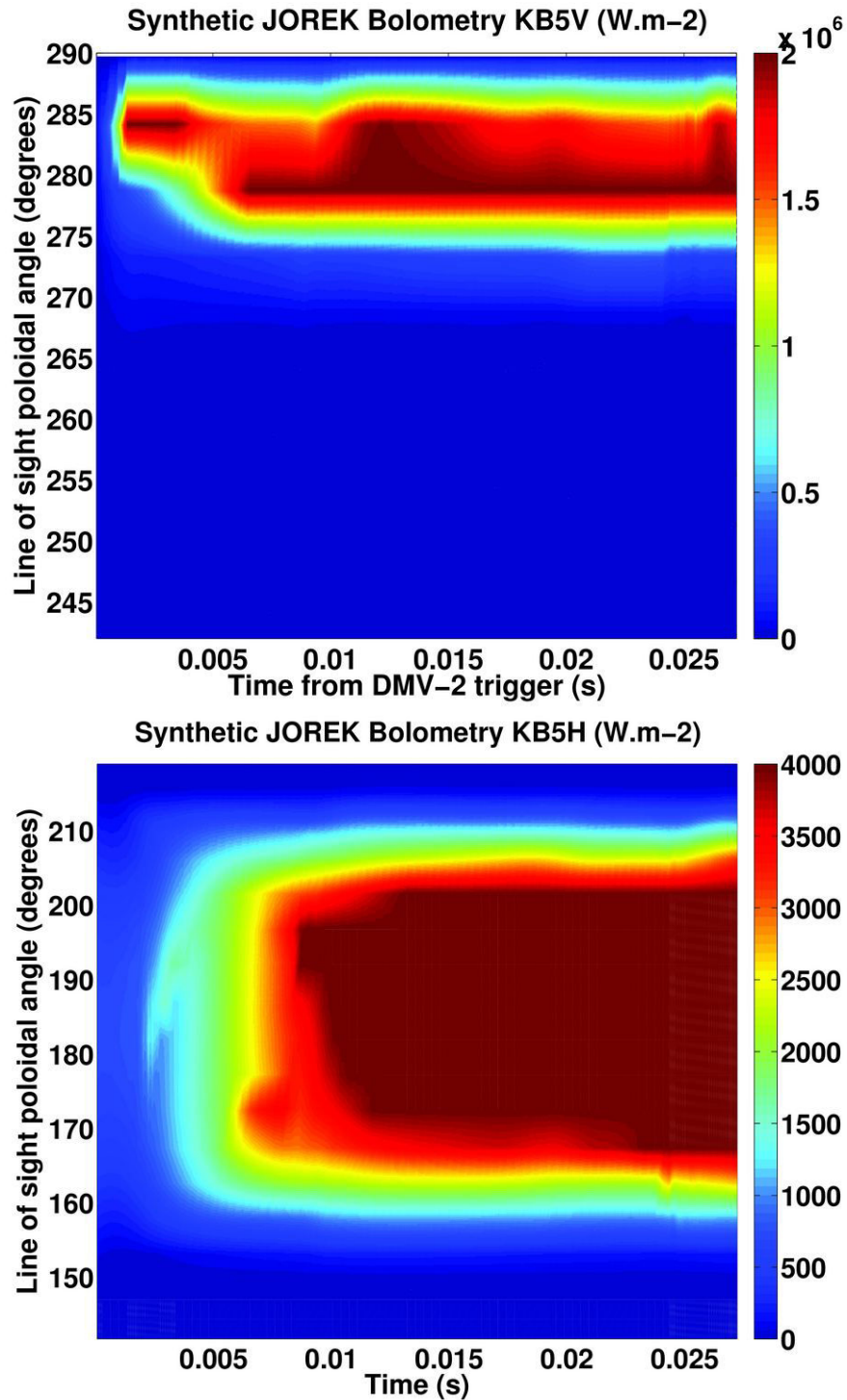


Figure 6.26: *Simulated bolometry signals: KB5V corresponds to the vertical bolometer and KB5H to the horizontal bolometer*

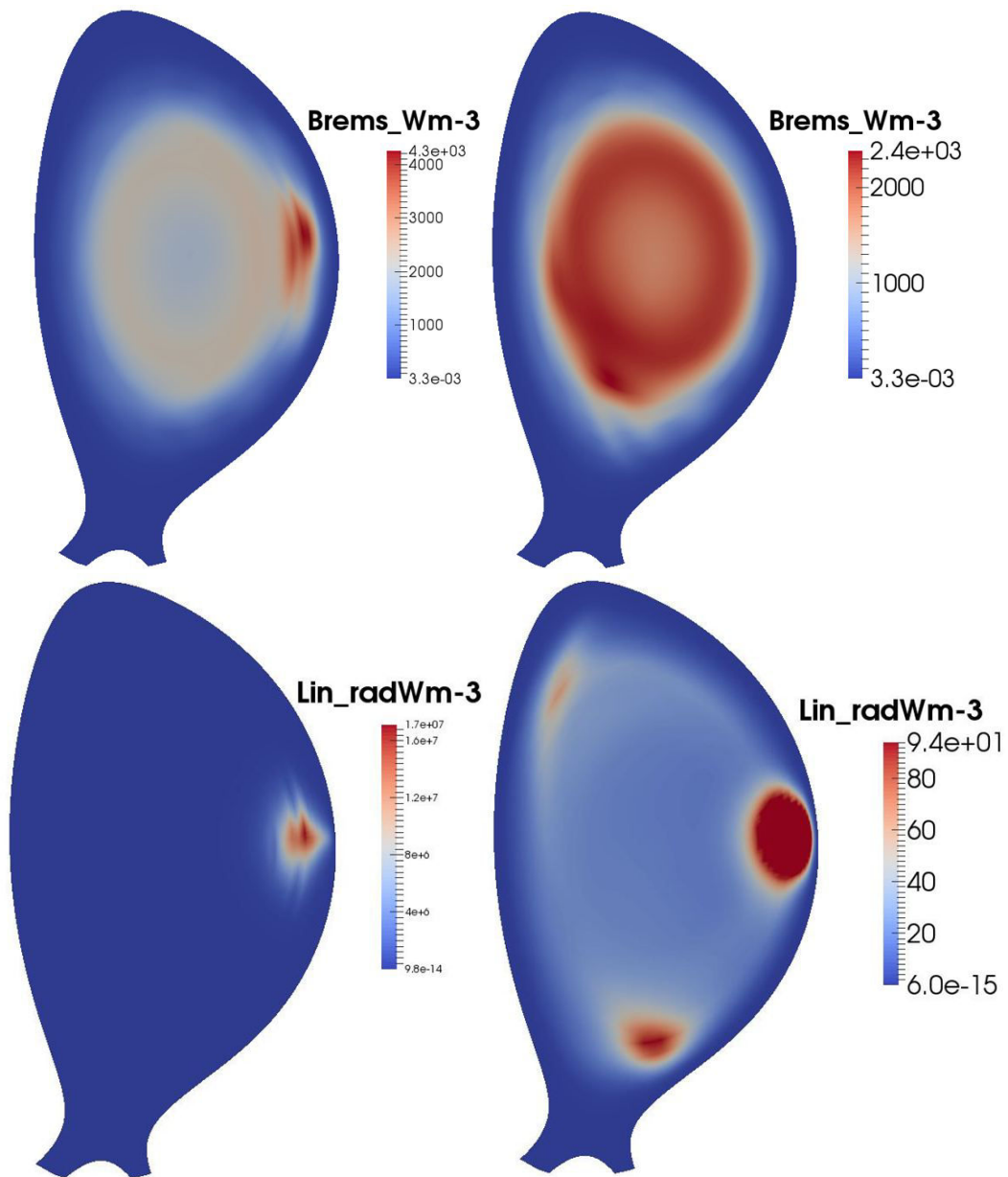


Figure 6.27: Poloidal cross-sections of the bremsstrahlung (top) and line (bottom) radiated power in the toroidal plane of the vertical (left) and horizontal (right) bolometers at $t = 9.35$ ms

6.2.6 Influence of input parameters on the simulations results

The previous sections presented the status of the work at a given point in time. However, given the discrepancies observed between the simulations and the experiment, work is being pursued. In particular, the effect of several input parameters is under investigation, as will be briefly described in this section.

Previous simulations have thus been repeated to test the influence of input parameters on the simulations results. It has to be mentioned that these parameters are quite sensitive and that we are close to the current limitations of the code.

Hyperresistivity As mentioned in the previous section, a large hyperresistivity η_{num} was used to avoid numerical instabilities at the center. It results in an effective resistivity much higher than the Spitzer resistivity ($\eta_{eff} \simeq 10^{-6}$). The simulation with $q_0 = 0.94$ presented above and in [Fil, Nardon, et al. 2015b] have thus been re-run with a lower hyperresistivity ($\eta_{eff} \simeq 10^{-7}$), all others parameters being identical. It results in a much stronger MHD activity than in previous simulations^k. Indeed, Figure 6.28 shows the evolution of the central electron temperature for this simulation but also the magnetic fluctuations measured by the synthetic Mirnov coil which are orders of magnitude higher than in previous simulations (see Figure 6.20) The crash of the internal kink mode is delayed and now occurs at 3.5 ms as can be seen on Figure 6.29 which compares the evolution of the central electron temperature for the two simulations (high and low η_{num}).

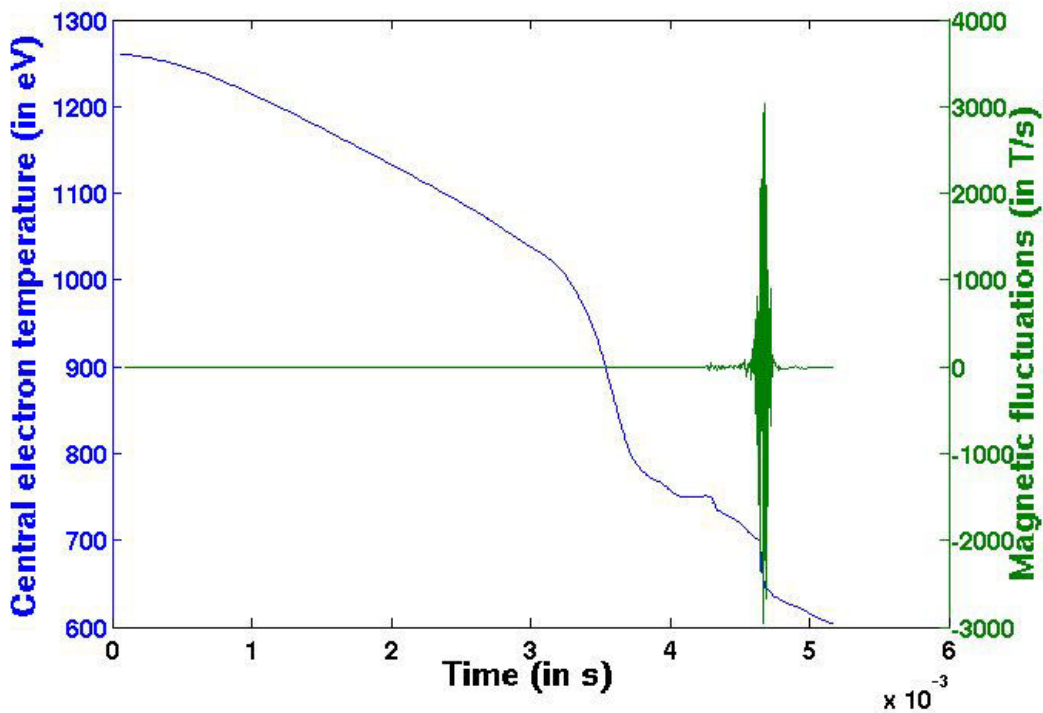


Figure 6.28: Evolution of the central electron temperature and of the magnetic fluctuations at the position of the synthetic Mirnov coil

^kFil, Nardon, et al. 2015a.

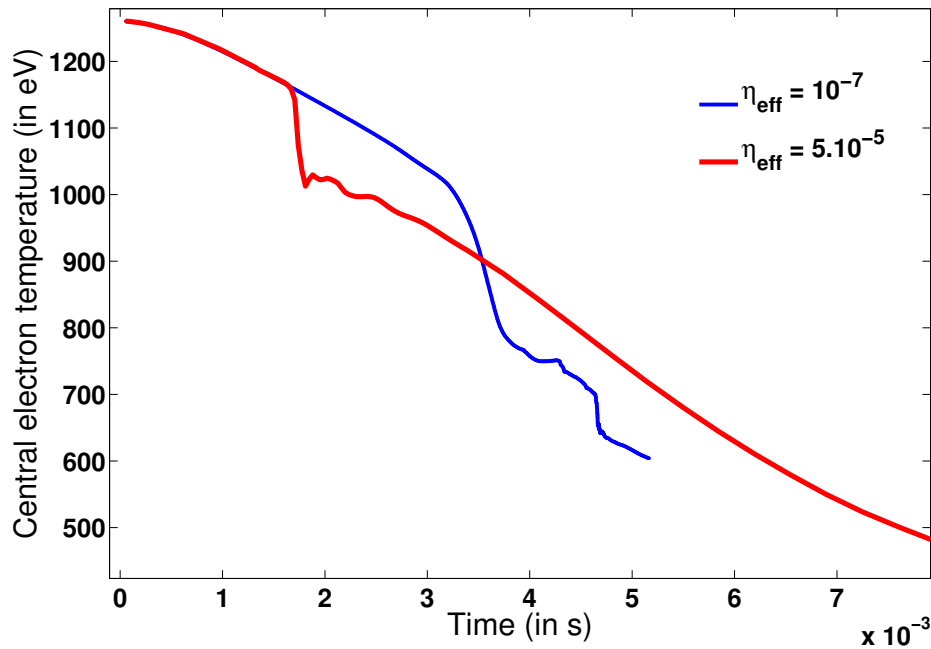


Figure 6.29: *Central electron temperature for the simulation of the previous section and the last simulation with a lower η_{num}*

Figures 6.30, 6.31 and 6.32 show the evolution of the toroidal current density, the electron temperature and the electron density before, during and after the peak of MHD activity. On each figure, the associated Poincare plot is included. One can see that the crash of the internal kink mode is now followed by the stochastization of field lines across the whole plasma.

The peak of MHD activity (Figure 6.28) is associated to a second drop of the central electron temperature. This phase is however very fast ($\simeq 5 \cdot 10^{-2}$ ms) and is insufficient to decrease drastically the electron temperature. We indeed quickly recover good flux surfaces at the center as can be seen on Figure 6.32.

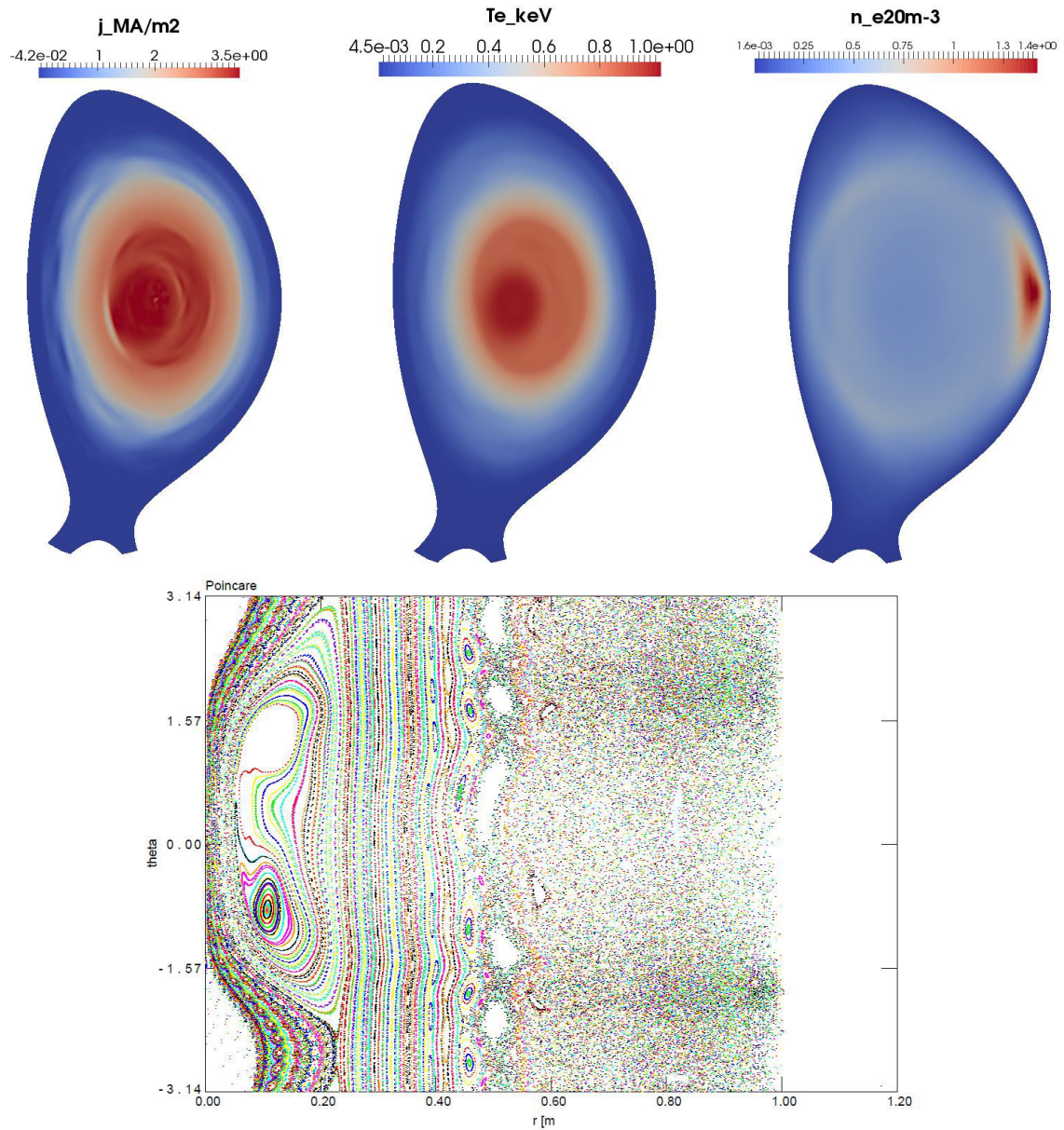


Figure 6.30: Poloidal cross-section of the toroidal current density (left), the electron temperature (middle) and the electron density (right) at $t = 3.28$ ms. Poincare plot (bottom) at the same time.

6.2. Toward code validation and quantitative comparison with experiments 105

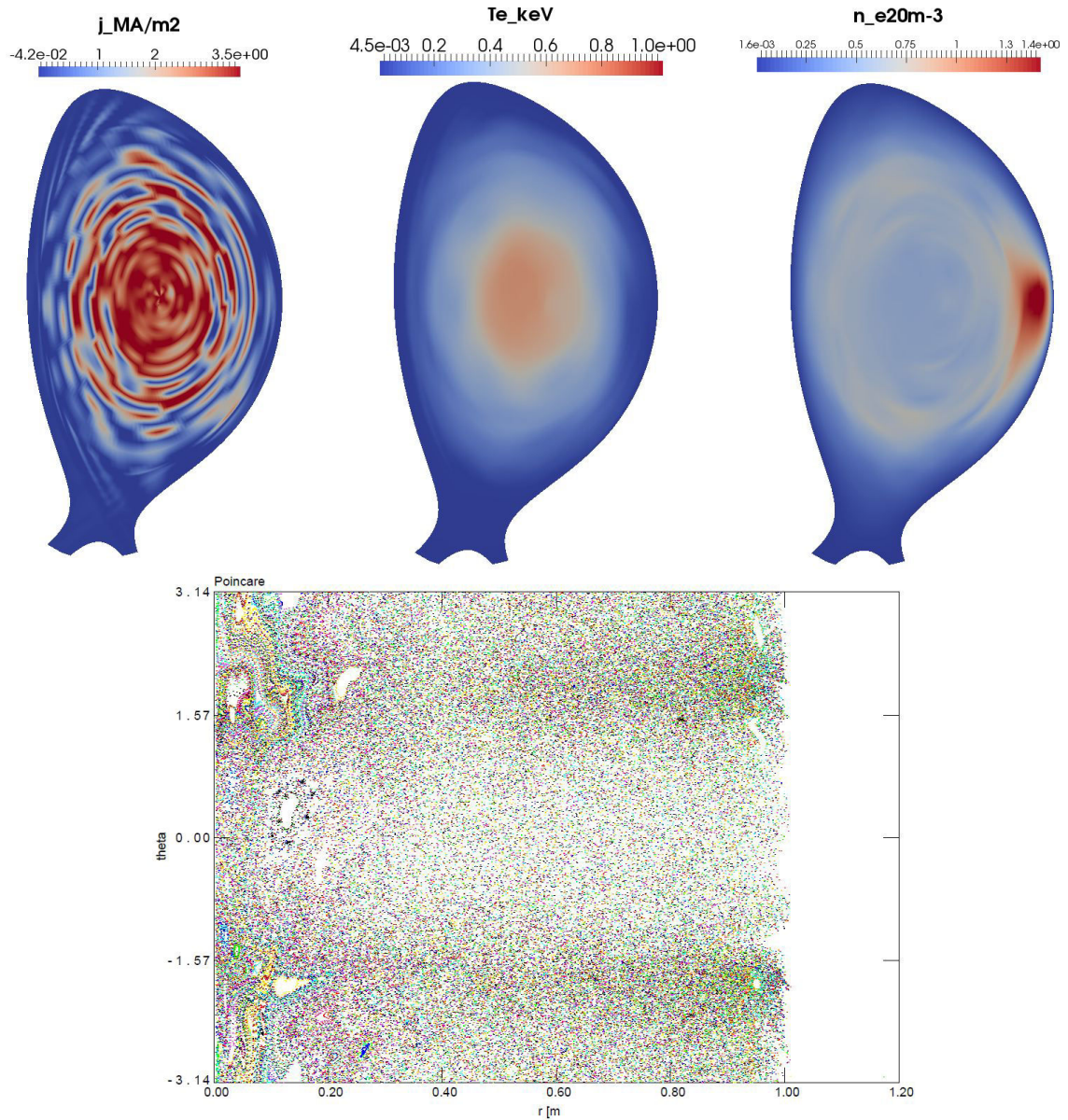


Figure 6.31: *Poloidal cross-section of the toroidal current density (left), the electron temperature (middle) and the electron density (right) at $t = 4.65$ ms. Poincaré plot (bottom) at the same time.*

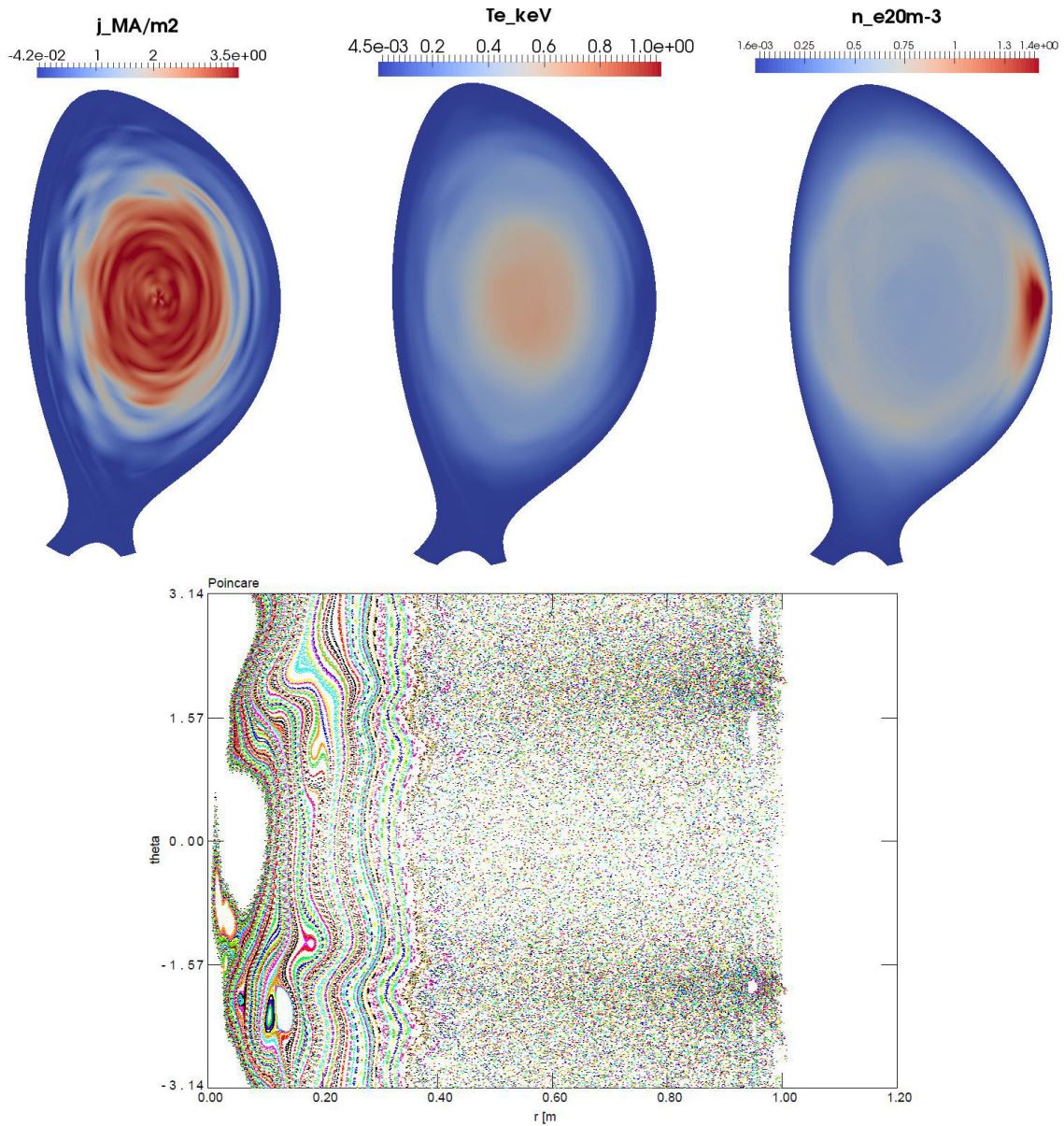


Figure 6.32: Poloidal cross-section of the toroidal current density (left), the electron temperature (middle) and the electron density (right) at $t = 4.75$ ms. Poincaré plot (bottom) at the same time.

6.2. Toward code validation and quantitative comparison with experiments 107

Background impurities In the simulation presented above, a background of impurities in the plasma was also included. According to JET spectrometers, traces of Argon (with a density possibly on the order of 0.1% of the plasma density) were detected in this experimental shot (still JET 86887) coming from the previous pulse in which an Ar MGI was triggered. In the simulation we put a constant density of impurities ($n_{imp} = 3 \cdot 10^{16} \text{ m}^{-3}$). This fact was taken into account by including in the simulation an additional term $-n_e n_{imp} L_{imp/Ar}$ in the energy equation 4.59 corresponding to an Ar density of $n_{imp} = 3 \cdot 10^{16} \text{ m}^{-3}$ (with a radiation rate $L_{imp/Ar}$ resembling that of Ar at coronal equilibrium):

$$L_{imp/Ar} = 2.4 \cdot 10^{-31} \times \exp \frac{(\ln T_e [ev] - \ln 20)^2}{0.8^2} \quad (6.7)$$

This formula for the radiation rate is plotted on Figure 6.33. Figure 6.34 displays the

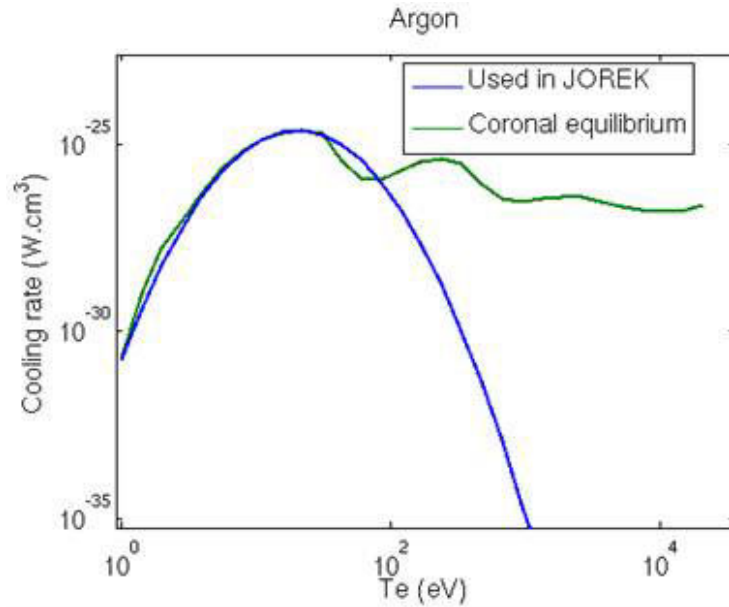


Figure 6.33: Radiation rate for Ar as a function of the electron temperature

poloidal cross-section of the power radiated by this impurity background. It dominates the bremsstrahlung and the line radiated power at the plasma edge, except at the injection location where the line radiation is still two orders of magnitude larger. Figures 6.35 and 6.36 display the simulated bolometry signals with and without the background of impurities. While the difference is minimal for the vertical bolometer the inclusion of impurities allows one to qualitatively recover the horizontal bolometer signal of the experiment (see Figure 6.25), at least for the pre-TQ phase. However, it is not sufficient to observe the post-MHD peak radiation burst. It can be explained by looking at the cooling rate function for the Ar impurity background (Figure 6.33). As the central temperature after the MHD burst is still above a few hundreds of eV, the radiation coming from the background impurities is still too low to decrease the central temperature down to experimental measurements.

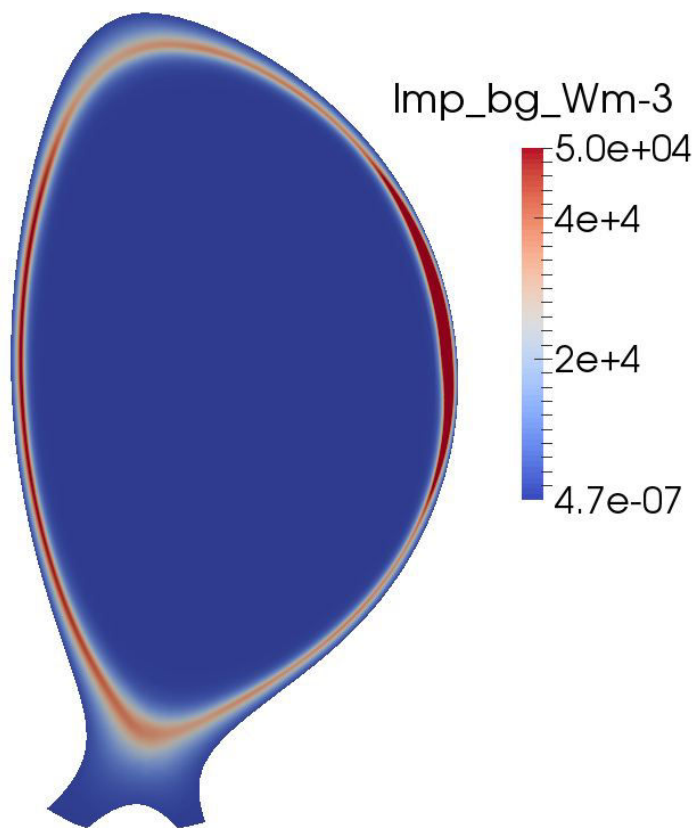


Figure 6.34: *Poloidal cross-sections of the radiated power of the impurity background in the toroidal plane of the vertical bolometer at $t = 1.5$ ms*

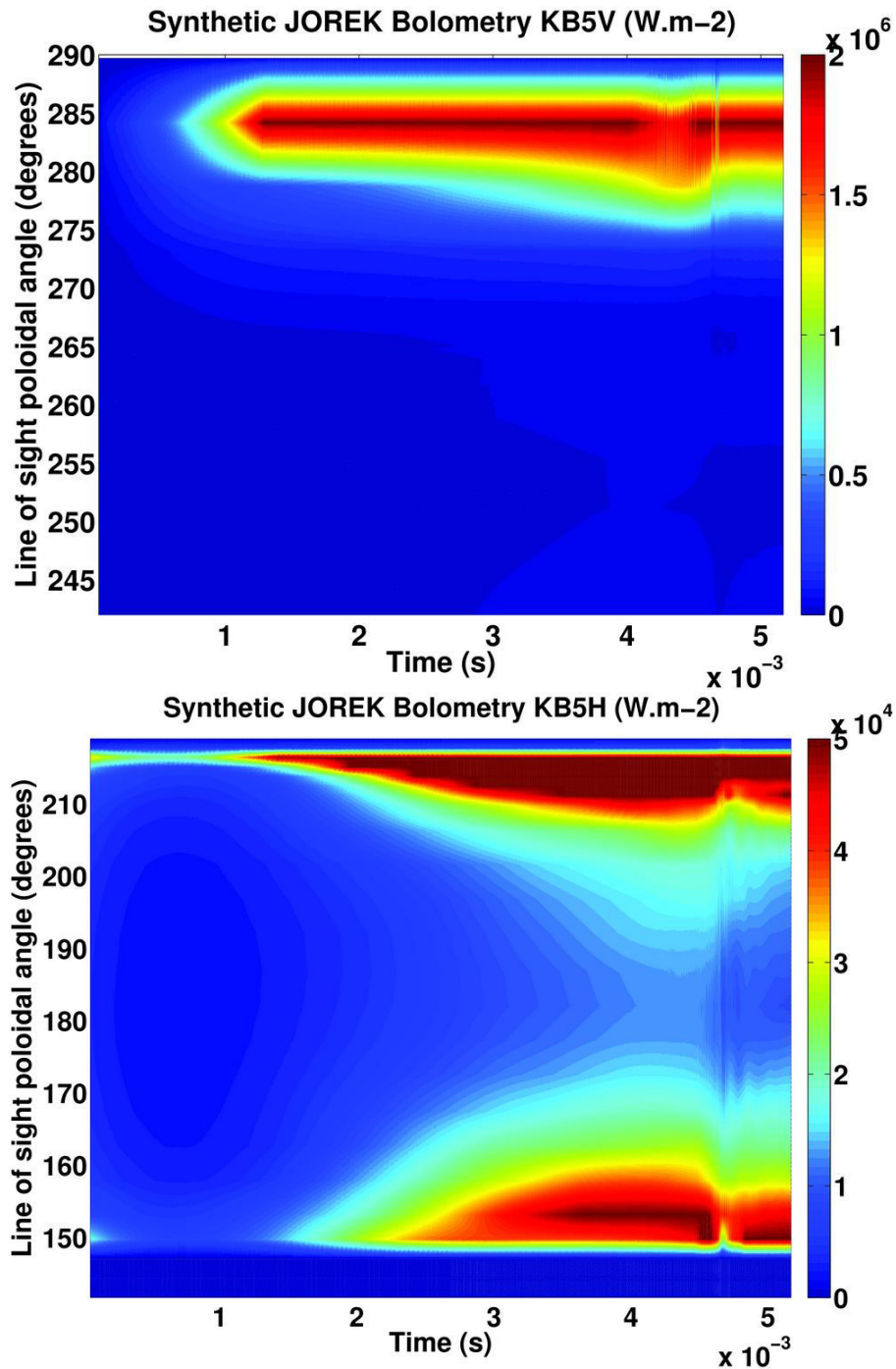


Figure 6.35: Simulated bolometry signals including the radiation from background impurities: KB5V corresponds to the vertical bolometer and KB5H to the horizontal bolometer

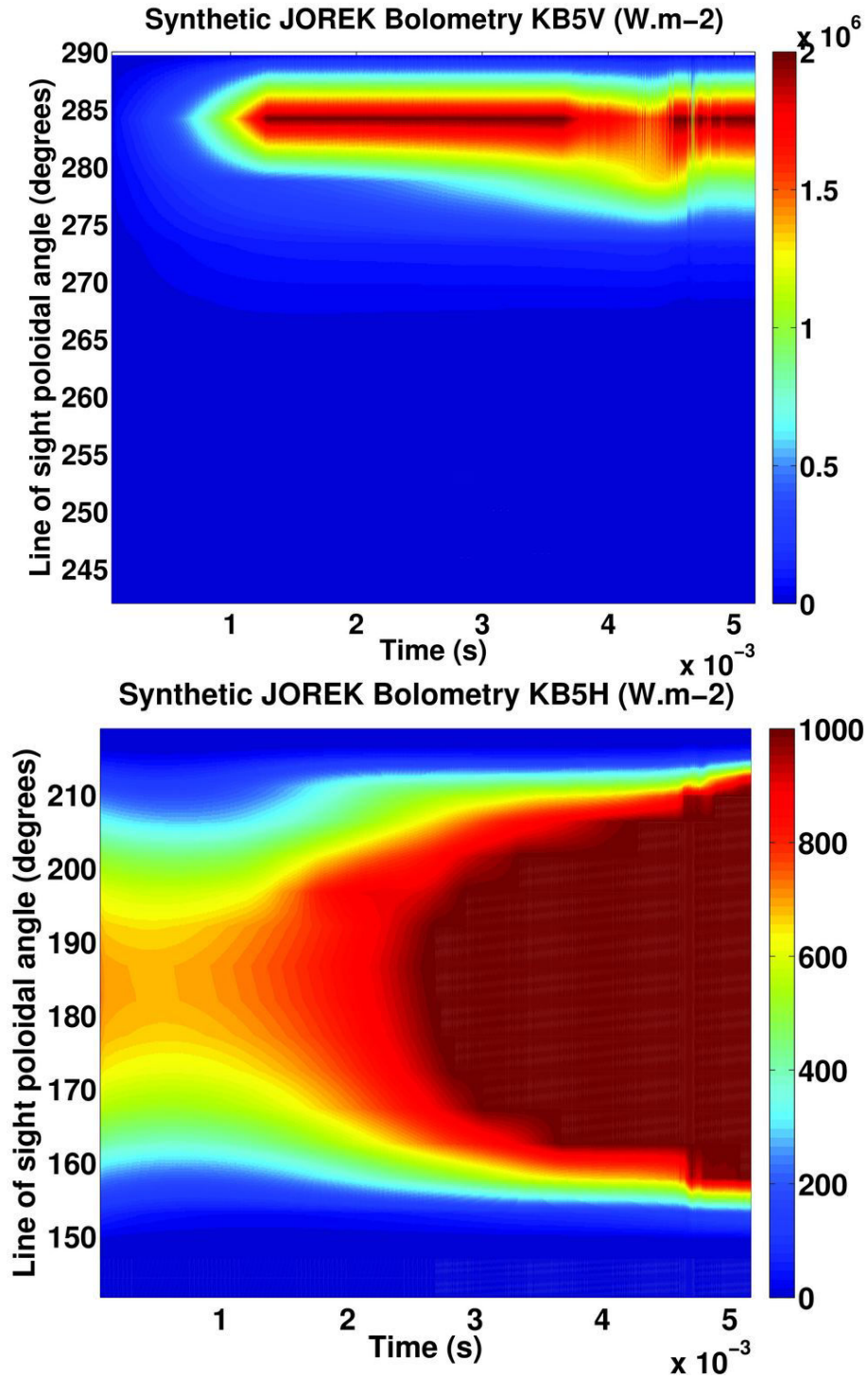


Figure 6.36: Simulated bolometry signals without the radiation from background impurities: KB5V corresponds to the vertical bolometer and KB5H to the horizontal bolometer

6.2. Toward code validation and quantitative comparison with experiments 11

Perpendicular ion diffusivity and parallel heat conductivity One explanation for this high central temperature is the value of the parallel heat conductivity which is still too low compared to the experimental value. Simulations aiming at using realistic values for the parallel heat conductivity, and the perpendicular ion diffusivity are currently running. Note that the simulations presented here are not finished yet and are very difficult to run because of numerical instabilities and memory consumption issues.

We can however already compare the increase of the edge density in the simulation presented in section 6.2.6 with a simulation having the same parameters except D_{perp} ($2.8 \text{ m}^2\text{s}^{-1}$ instead of $28 \text{ m}^2\text{s}^{-1}$) and $\kappa_{||}$ ($6.7 \times 10^{29} \text{ m}^{-1}\text{s}^{-1}$ instead of $6.7 \times 10^{28} \text{ m}^{-1}\text{s}^{-1}$). The comparison between the two simulations shows that the edge density is increasing faster in the latter simulation. Indeed, the increase of the synthetic interferometer signals is faster Figure 6.37 than previously (see Figure 6.14 for $P_{DMV} = 1 \text{ bar}$). Moreover, the central density is now almost constant in the center when it was increasing a lot before (see Figure 6.38). The peak of electron density (at the neutral injection location) is also 4 times higher. Figure 6.39 also shows that the internal kink mode is destabilized earlier than in the previous simulations (fast drop of the central electron temperature). The central cooling due to dilution is therefore reduced in these simulations.

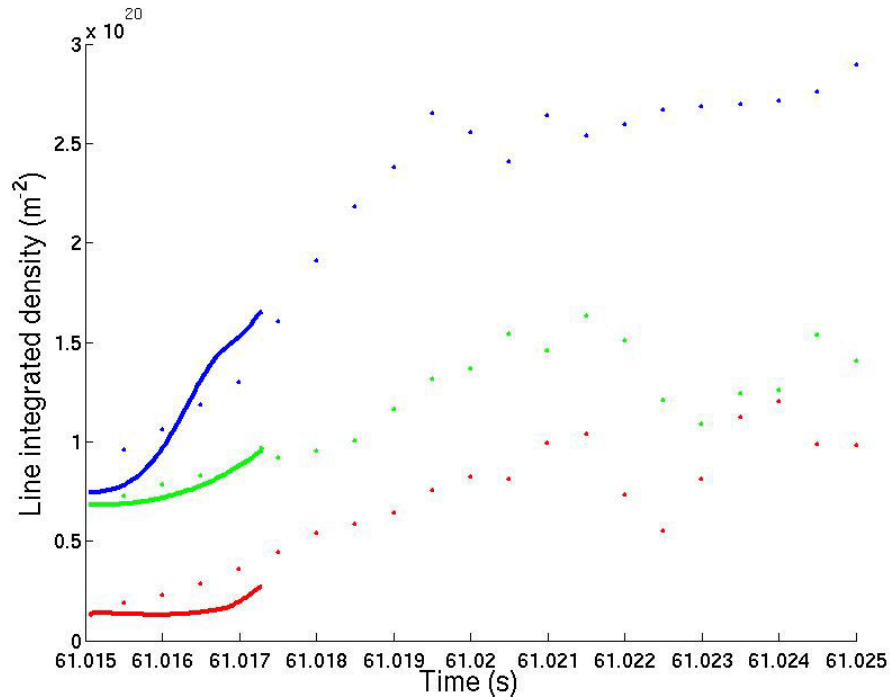


Figure 6.37: *Synthetic interferometry measurements for the simulation with realistic D_{perp} and $\kappa_{||}$ (lines) compared to the experimental data (dots).*

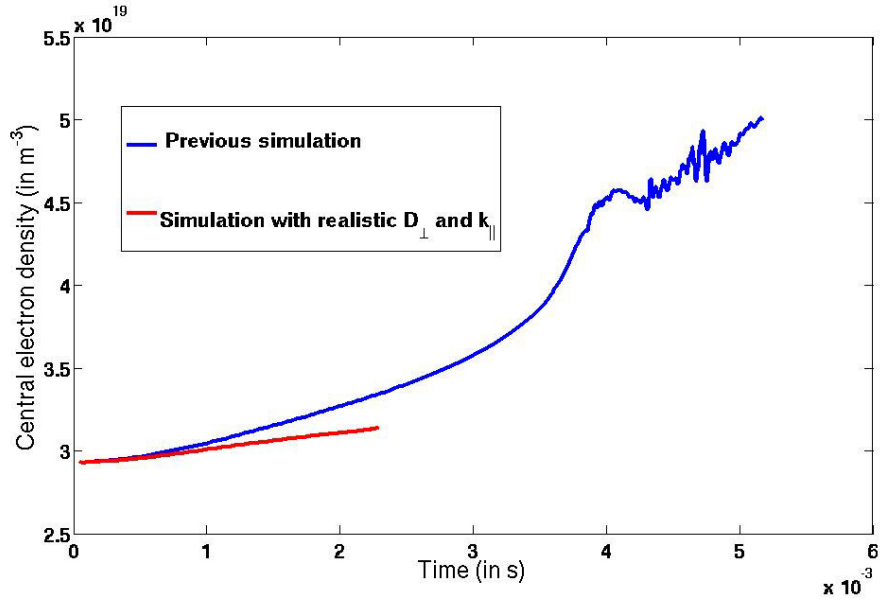


Figure 6.38: Evolution of the central electron density for the two simulations

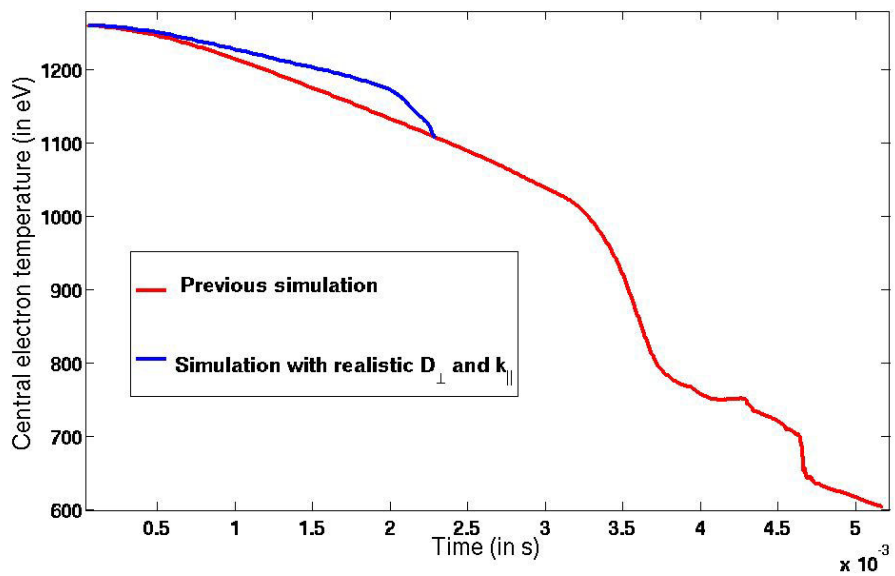


Figure 6.39: Evolution of the central electron temperature for the two simulations

Summary and outlook

Simulations of a D_2 MGI-triggered disruption in an Ohmic JET plasma have been performed with the JOREK and IMAGINE codes. The objective was to progress in the understanding of MGI-triggered disruptions, but also to validate the codes on a relatively simple case before applying them to more complicated cases (e.g. high-Z MGI) and eventually to ITER. A complex neutral-plasma model in slab geometry is solved by the IMAGINE code. The neutral transport is convective and the model includes several atomic processes between plasma ions, electrons and neutrals. Charge-exchange is found to play a major role in the gas penetration into the plasma. The fast energy transfer due to charge-exchange creates a shock wave and only a fraction of the neutral gas is transmitted and can cool the plasma. Future work will focus on validating this process by extensive comparison with experiment, for example by studying the experimentally observed dependencies of the pre-TQ time with the gas species, the pressure in the DMV or the plasma temperature. Comparison with other codes is also important, for example by simulating the same experimental shot and comparing the codes results (with ASTRA for example). An important foreseen application of IMAGINE would also be to do simulations of JET second MGI (in a post-TQ plasma) presented in section 3.2 and in Figure 3.4. Experimentally, the reasons for the failure of the runaway electron beam mitigation in these shots are still unclear and might be explained by such simulations. This would require further development of the code to be able to simulate high-Z MGI.

An equation for neutral density as well as appropriate atomic physics terms have also been added in the JOREK code. In the simulations, the MGI gives rise to an overdensity that rapidly propagates in the parallel direction. Simulations with $P_{DMV2} = 1$ or 2 bar match interferometry measurements better than with the experimental value of 5 bar, suggesting that not all of the gas enters the plasma in the experiment, as found with IMAGINE. The main focus of the study is on the MHD activity. In the first few milliseconds, the MGI causes the simultaneous growth of several magnetic island chains (mainly 2/1 and 3/2) and seeds the 1/1 internal kink mode, presumably via imposing a 3D structure rather than by creating unstable axisymmetric profiles. The O-points of all islands (including 1/1) are located in front of the gas deposition region, consistently with experimental observations. In a second phase, tearing modes keep growing but this time presumably due to an unstable current profile. A peak in MHD activity takes place near 10 ms, associated to a stochastic layer covering roughly the outer half of the plasma and to a peak in I_p and a burst of dB/dt on the synthetic Mirnov coil signal. These two typical signatures of the TQ are observed experimentally near the same time, which is encouraging, but with a magnitude larger by roughly one order of magnitude. Not surprisingly, the TQ is not

complete in the simulations: T_e does not go below a few hundred eV at the end of the simulation (most of the drop being actually due to dilution, owing to the fast diffusion of the over-density to the center due to the large diffusion coefficient used for numerical stability reasons). This incomplete TQ may be attributed to good flux surfaces remaining in the core but may also be related to missing radiation. Indeed, the level of radiation in the simulations is much smaller than the experimental one.

In view of these results, directions for progress can clearly be identified. In order to get a complete TQ in the simulations, a much stronger MHD activity is needed. Using a lower hyperresistivity (see section 6.2.6) increased the MHD activity by orders of magnitude but is still not sufficient to get a TQ. The creation of a strongly unstable current profile by the penetration of a cold front is likely to be the key. This effect has for example lead to the TQ in the JOREK MGI simulations presented in section 6.1. One difference with the present simulations was that the cold front was much sharper due to different atomic physics settings. Effects that could sharpen the cold front should therefore be sought. In section 6.2.6 the effect of a background of impurities have been tested and is improving the comparison simulation vs. experiment. It is also important to assess the influence of simulation parameters. More realistic D_{perp} and $\kappa_{||}$ have been used and improve the match on interferometry (particularly for edge densities) but the simulations still tend to produce numerical instabilities near the injection location and at the grid center. Another direction for progress is to improve the neutral transport model (which is currently purely diffusive), for example by implementing neutral convection. Ideally, one should implement additional equations for the neutrals velocity and pressure, as done in IMAGINE. A model for neutrals allowing high-Z MGI simulations is also foreseen, as well as the inclusion of eddy and halo currents by coupling JOREK with the STARWALL code. The development of a guiding center treatment of the runaway electrons in JOREK is also on-going. With such a tool, one could study the generation and the mitigation of RE beams in a realistic magnetic configuration (during the TQ and the CQ).

Bibliography

- [1] G. Arnoux et al. “Heat loads on plasma facing components during disruptions on JET”. In: *Nuclear Fusion* 49.8 (2009), p. 085038. URL: <http://stacks.iop.org/0029-5515/49/i=8/a=085038> (cit. on p. 18).
- [2] D. Biskamp. *Nonlinear Magnetohydrodynamics*. Cambridge, U.K.: Cambridge University Press, 2004 (cit. on pp. 89, 90).
- [3] Allen H. Boozer. “Theory of tokamak disruptions”. In: *Physics of Plasmas* 19.5 (2012), p. 058101. ISSN: 1070664X. DOI: 10.1063/1.3703327. URL: <http://scitation.aip.org/content/aip/journal/pop/19/5/10.1063/1.3703327> (cit. on p. 15).
- [4] S.A. Bozhenkov et al. “Fuelling efficiency of massive gas injection in TEXTOR: mass scaling and importance of gas flow dynamics”. In: *Nuclear Fusion* 51.8 (Aug. 2011), p. 083033. ISSN: 0029-5515. DOI: 10.1088/0029-5515/51/8/083033. URL: <http://stacks.iop.org/0029-5515/51/i=8/a=083033?key=crossref.03097b3c118e81e2f773e4b674f454ea> (cit. on pp. 61, 62, 81–83).
- [5] J. Bucalossi et al. “Assessment of massive gas injection as a disruption mitigation tool in Tore Supra”. In: *Journal of Nuclear Materials* 415.1 (Aug. 2011), S832–S835. ISSN: 00223115. DOI: 10.1016/j.jnucmat.2011.01.045. URL: <http://linkinghub.elsevier.com/retrieve/pii/S0022311511000778> (cit. on p. 34).
- [6] I. T. Chapman. “Controlling sawtooth oscillations in tokamak plasmas”. In: *Plasma Physics and Controlled Fusion* 53.1 (2011), p. 013001. URL: <http://stacks.iop.org/0741-3335/53/i=1/a=013001> (cit. on p. 27).
- [7] S. K. Combs and L. R. Baylor. “RD in support of the shattered pellet technique for disruption mitigation”. In: *VLT Conference* (2013). URL: http://vlt.ornl.gov/research/20130619_VLT_combs.pdf (cit. on p. 30).
- [8] N. Commaux et al. “Demonstration of rapid shutdown using large shattered deuterium pellet injection in DIII-D”. In: *Nuclear Fusion* 50.11 (2010), p. 112001. URL: <http://stacks.iop.org/0029-5515/50/i=11/a=112001> (cit. on p. 29).
- [9] O. Czarny and G. T. A. Huysmans. “Bézier surfaces and finite elements for MHD simulations”. In: *Journal of Computational Physics* 227.16 (Aug. 2008), pp. 7423–7445. ISSN: 00219991. DOI: 10.1016/j.jcp.2008.04.001. URL: <http://linkinghub.elsevier.com/retrieve/pii/S0021999108002118> (cit. on p. 56).

- [10] P.C. De Vries et al. “Survey of disruption causes at JET”. In: *Nuclear Fusion* 51.5 (2011), p. 053018. URL: <http://stacks.iop.org/0029-5515/51/i=5/a=053018> (cit. on pp. 24, 26).
- [11] T.E. Evans et al. “Measurements of non-axisymmetric halo currents with and without ‘killer’ pellets during disruptions in the DIII-D tokamak”. In: *Journal of Nuclear Materials* 241–243 (1997), pp. 606–611. ISSN: 0022-3115. DOI: [http://dx.doi.org/10.1016/S0022-3115\(97\)80108-0](http://dx.doi.org/10.1016/S0022-3115(97)80108-0). URL: <http://www.sciencedirect.com/science/article/pii/S0022311597801080> (cit. on p. 39).
- [12] F. Felici et al. “Integrated real-time control of MHD instabilities using multi-beam ECRH/ECCD systems on TCV”. In: *Nuclear Fusion* 52.7 (2012), p. 074001. URL: <http://stacks.iop.org/0029-5515/52/i=7/a=074001> (cit. on p. 27).
- [13] O. Fevrier et al. “First principle fluid modelling of magnetic island stabilization by ECCD”. In: *submitted to Plasma Physics and Controlled Fusion* (2015) (cit. on p. 27).
- [14] A. Fil et al. “Proceedings of the 41th European Physical Society Conference on Plasma Physics”. In: (2014). URL: <http://ocs.ciemat.es/EPS2014PAP/pdf/P1.045.pdf> (cit. on pp. 48, 90).
- [15] A. Fil et al. “Proceedings of the 42th European Physical Society Conference on Plasma Physics”. In: (2015). URL: <http://ocs.ciemat.es/EPS2015PAP/pdf/04.135.pdf> (cit. on p. 102).
- [16] A. Fil et al. “Three-dimensional non-linear magnetohydrodynamic modeling of massive gas injection triggered disruptions in JET”. In: *Physics of Plasmas* 22.6, 062509 (2015). DOI: <http://dx.doi.org/10.1063/1.4922846>. URL: <http://scitation.aip.org/content/aip/journal/pop/22/6/10.1063/1.4922846> (cit. on p. 102).
- [17] S. Futatani et al. “Non-linear MHD modelling of ELM triggering by pellet injection in DIII-D and implications for ITER”. In: *Nuclear Fusion* 54.7 (July 2014), p. 073008. ISSN: 0029-5515. DOI: [10.1088/0029-5515/54/7/073008](https://doi.org/10.1088/0029-5515/54/7/073008). URL: <http://stacks.iop.org/0029-5515/54/i=7/a=073008?key=crossref.d888459be4901fafd90e4c210b9f6fa1> (cit. on p. 82).
- [18] R. S. Granetz et al. “An ITPA joint experiment to study runaway electron generation and suppression”. In: *Physics of Plasmas* 21.7 (July 2014), p. 072506. ISSN: 1070-664X. DOI: [10.1063/1.4886802](https://doi.org/10.1063/1.4886802). URL: <http://scitation.aip.org/content/aip/journal/pop/21/7/10.1063/1.4886802> (cit. on p. 19).
- [19] M. Greenwald. “Density limits in toroidal plasmas”. In: *Plasma Physics and Controlled Fusion* 44.8 (2002), R27. URL: <http://stacks.iop.org/0741-3335/44/i=8/a=201> (cit. on pp. 23, 24).
- [20] C. Guillemaut et al. “Influence of atomic physics on EDGE2D-EIRENE simulations of JET divertor detachment with carbon and beryllium/tungsten plasma-facing components”. In: *Nuclear Fusion* 54.9 (2014), p. 093012. URL: <http://stacks.iop.org/0029-5515/54/i=9/a=093012> (cit. on p. 45).

- [21] A. Hassanein et al. “Can tokamaks PFC survive a single event of any plasma instabilities?” In: *Journal of Nuclear Materials* 438, Supplement (2013). Proceedings of the 20th International Conference on Plasma-Surface Interactions in Controlled Fusion Devices, S1266–S1270. ISSN: 0022-3115. DOI: <http://dx.doi.org/10.1016/j.jnucmat.2013.01.281>. URL: <http://www.sciencedirect.com/science/article/pii/S0022311513002894> (cit. on p. 18).
- [22] R.D. Hazeltine and J.D. Meiss. *Plasma Confinement*. Dover Books on Physics. Dover Publications, 2013. ISBN: 9780486151038. URL: <https://books.google.fr/books?id=LDPDAgAAQBAJ> (cit. on p. 42).
- [23] T.C Hender et al. “Chapter 3: MHD stability, operational limits and disruptions”. In: *Nuclear Fusion* 47.6 (June 2007), S128–S202. ISSN: 0029-5515. DOI: [10.1088/0029-5515/47/6/S03](https://doi.org/10.1088/0029-5515/47/6/S03). URL: <http://stacks.iop.org/0029-5515/47/i=6/a=S03?key=crossref.0b9322e42a59b955269531e35f39b3bb> (cit. on pp. 15, 17).
- [24] P. Hénon, P. Ramet, and J. Roman. “PASTIX: A High-performance Parallel Direct Solver for Sparse Symmetric Positive Definite Systems”. In: *Parallel Comput.* 28.2 (Feb. 2002), pp. 301–321. ISSN: 0167-8191. DOI: [10.1016/S0167-8191\(01\)00141-7](https://doi.org/10.1016/S0167-8191(01)00141-7). URL: [http://dx.doi.org/10.1016/S0167-8191\(01\)00141-7](http://dx.doi.org/10.1016/S0167-8191(01)00141-7) (cit. on p. 57).
- [25] M. Hoelzl et al. “Non-linear Simulations of MHD Instabilities in Tokamaks Including Eddy Current Effects and Perspectives for the Extension to Halo Currents”. In: (). arXiv: [arXiv:1408.6379v1](https://arxiv.org/abs/1408.6379v1) (cit. on p. 39).
- [26] M. Hoelzl et al. “Coupling JOEREK and STARWALL Codes for Non-linear Resistive-wall Simulations”. In: *Journal of Physics: Conference Series* 401.1 (2012). URL: <http://stacks.iop.org/1742-6596/401/i=1/a=012010> (cit. on p. 57).
- [27] E. M. Hollmann et al. “Status of research toward the ITER disruption mitigation system”. In: *Physics of Plasmas* 22.2 (Feb. 2015), p. 021802. ISSN: 1070-664X. DOI: [10.1063/1.4901251](https://doi.org/10.1063/1.4901251). URL: <http://scitation.aip.org/content/aip/journal/pop/22/2/10.1063/1.4901251> (cit. on p. 15).
- [28] E.M. Hollmann et al. “Control and dissipation of runaway electron beams created during rapid shutdown experiments in DIII-D”. In: *Nuclear Fusion* 53.8 (2013), p. 083004. URL: <http://stacks.iop.org/0029-5515/53/i=8/a=083004> (cit. on p. 29).
- [29] R. H. Huddlestone and S. L. Leonard. *Plasma diagnostic techniques - spectral intensities*. 1965 (cit. on p. 54).
- [30] D. A. Humphreys and A. G. Kellman. “Analytic modeling of axisymmetric disruption halo currents”. In: *Physics of Plasmas* 6.7 (1999), p. 2742. ISSN: 1070664X. DOI: [10.1063/1.873231](https://doi.org/10.1063/1.873231). URL: <http://scitation.aip.org/content/aip/journal/pop/6/7/10.1063/1.873231> (cit. on p. 20).

- [31] O. Hurricane et al. “Fuel gain exceeding unity in an inertially confined fusion implosion.” In: *Nature* 506.7488 (Feb. 2014), pp. 343–8. ISSN: 1476-4687. DOI: [10.1038/nature13008](https://doi.org/10.1038/nature13008). URL: <http://www.ncbi.nlm.nih.gov/pubmed/24522535> (cit. on p. 4).
- [32] G T A Huysmans et al. “Non-linear MHD simulations of edge localized modes (ELMs)”. In: *Plasma Physics and Controlled Fusion* 51.12 (2009), p. 124012. URL: <http://stacks.iop.org/0741-3335/51/i=12/a=124012> (cit. on p. 56).
- [33] V A Izzo. “MHD modeling in support of thermal quench and runaway electron mitigation for ITER”. In: July (2013) (cit. on pp. 34, 88).
- [34] Stefan Jachmich et al. “Implementation of a new Disruption Mitigation System into the control system of {JET}”. In: *Fusion Engineering and Design* (2015). ISSN: 0920-3796. DOI: <http://dx.doi.org/10.1016/j.fusengdes.2015.01.047>. URL: <http://www.sciencedirect.com/science/article/pii/S0920379615000745> (cit. on p. 32).
- [35] U. Kruezi. “Proceedings of the 36th European Physical Society Conference on Plasma Physics”. In: (2009). URL: <http://www.euro-fusionscipub.org/wp-content/uploads/2014/11/EFDC090655.pdf> (cit. on p. 31).
- [36] A. Kurganov and E. Tadmor. “New High-Resolution Central Schemes for Non-linear Conservation Laws and Convection–Diffusion Equations”. In: *Journal of Computational Physics* 160.1 (2000), pp. 241–282. ISSN: 0021-9991. DOI: <http://dx.doi.org/10.1006/jcph.2000.6459>. URL: <http://www.sciencedirect.com/science/article/pii/S0021999100964593> (cit. on p. 51).
- [37] I.S. Landman et al. “Modelling of massive gas injection for {ITER} disruption mitigation”. In: *Journal of Nuclear Materials* 438, Supplement (2013). Proceedings of the 20th International Conference on Plasma-Surface Interactions in Controlled Fusion Devices, S871–S874. ISSN: 0022-3115. DOI: <http://dx.doi.org/10.1016/j.jnucmat.2013.01.188>. URL: <http://www.sciencedirect.com/science/article/pii/S0022311513001967> (cit. on p. 33).
- [38] B. Van Leer. “MUSCL, a new approach to numerical gas dynamics”. In: *Computing in Plasmaphysics and Astrophysics. Proceedings of the Second European Conference on Computational Physics* (1976) (cit. on p. 49).
- [39] M. Lehnen et al. “Disruption mitigation by massive gas injection in JET”. In: *Nuclear Fusion* 51.12 (Dec. 2011), p. 123010. ISSN: 0029-5515. DOI: [10.1088/0029-5515/51/12/123010](https://doi.org/10.1088/0029-5515/51/12/123010). URL: <http://stacks.iop.org/0029-5515/51/i=12/a=123010?key=crossref.8ac5cb170ffd54f70dcbc1608ea62924> (cit. on p. 39).
- [40] M. Lehnen et al. “Disruptions in ITER and strategies for their control and mitigation”. In: *Journal of Nuclear Materials* (2014). ISSN: 0022-3115. DOI: <http://dx.doi.org/10.1016/j.jnucmat.2014.10.075>. URL: <http://www.sciencedirect.com/science/article/pii/S0022311514007594> (cit. on pp. 15, 18, 96).
- [41] M. Lehnen et al. “Radiation asymmetries during the thermal quench of massive gas injection disruptions in JET”. In: (2014), pp. 1–20 (cit. on pp. 22, 29, 34).

- [42] A. Loarte et al. “A new look at JET operation with Be as plasma facing material”. In: *Journal of Nuclear Materials* 337–339 (2005). PSI-16, pp. 816–820. ISSN: 0022-3115. DOI: <http://dx.doi.org/10.1016/j.jnucmat.2004.09.038>. URL: <http://www.sciencedirect.com/science/article/pii/S0022311504009110> (cit. on p. 18).
- [43] A. Loarte et al. “Chapter 4: Power and particle control”. In: *Nuclear Fusion* 47.6 (2007), S203. URL: <http://stacks.iop.org/0029-5515/47/i=6/a=S04> (cit. on p. 18).
- [44] Y. Marandet et al. “Influence of neutral particles on scrape-off layer turbulence with application to the interpretation of fast camera data”. In: *Journal of Nuclear Materials* 438, Supplement (2013). Proceedings of the 20th International Conference on Plasma-Surface Interactions in Controlled Fusion Devices, S518–S521. ISSN: 0022-3115. DOI: <http://dx.doi.org/10.1016/j.jnucmat.2013.01.107>. URL: <http://www.sciencedirect.com/science/article/pii/S0022311513001153> (cit. on p. 47).
- [45] E. T. Meier and U. Shumlak. “A general nonlinear fluid model for reacting plasma-neutral mixtures”. In: *Physics of Plasmas* 19.7, 072508 (2012). DOI: <http://dx.doi.org/10.1063/1.4736975>. URL: <http://scitation.aip.org/content/aip/journal/pop/19/7/10.1063/1.4736975> (cit. on p. 46).
- [46] S. Miyamoto et al. “Inter-code comparison benchmark between DINA and TSC for ITER disruption modelling”. In: *Nuclear Fusion* 54.8 (2014), p. 083002. URL: <http://stacks.iop.org/0029-5515/54/i=8/a=083002> (cit. on p. 39).
- [47] A. Murari et al. “Unbiased and non-supervised learning methods for disruption prediction at JET”. In: *Nuclear Fusion* 49.5 (2009), p. 055028. URL: <http://stacks.iop.org/0029-5515/49/i=5/a=055028> (cit. on p. 28).
- [48] T. Nicolas. “Sawtooth driven particle transport in tokamak plasmas”. Theses. Ecole Polytechnique X, Dec. 2013. URL: <https://pastel.archives-ouvertes.fr/pastel-00926428> (cit. on p. 89).
- [49] E. Nilsson et al. “Kinetic modelling of runaway electron avalanches in tokamak plasmas”. In: (Mar. 2015), p. 23. arXiv: 1503.06082. URL: <http://arxiv.org/abs/1503.06082> (cit. on p. 19).
- [50] S. Nowak et al. “Control of sawtooth periods by pulsed ECH/ECCD in the FTU tokamak”. In: *Nuclear Fusion* 54.3 (2014), p. 033003. URL: <http://stacks.iop.org/0029-5515/54/i=3/a=033003> (cit. on p. 27).
- [51] P. B. Parks and W. Wu. “Modelling penetration and plasma response of a dense neutral gas jet in a post-thermal quenched plasma”. In: *Nuclear Fusion* 54.2 (2014), p. 023002. URL: <http://stacks.iop.org/0029-5515/54/i=2/a=023002> (cit. on p. 64).

- [52] G. Pautasso et al. “Contribution of ASDEX Upgrade to disruption studies for ITER”. In: *Nuclear Fusion* 51.10 (Oct. 2011), p. 103009. ISSN: 0029-5515. DOI: [10.1088/0029-5515/51/10/103009](https://doi.org/10.1088/0029-5515/51/10/103009). URL: <http://stacks.iop.org/0029-5515/51/i=10/a=103009?key=crossref.8c309020ac8828cf85dcc50ab4d8411c> (cit. on p. 39).
- [53] C. Paz-Soldan et al. “Growth and decay of runaway electrons above the critical electric field under quiescent conditions”. In: *Physics of Plasmas* 21.2 (Feb. 2014), p. 022514. ISSN: 1070-664X. DOI: [10.1063/1.4866912](https://doi.org/10.1063/1.4866912). URL: <http://scitation.aip.org/content/aip/journal/pop/21/2/10.1063/1.4866912> (cit. on p. 19).
- [54] J. Rapp et al. “Integrated scenario with type-III ELMy H-mode edge: extrapolation to ITER”. In: *Nuclear Fusion* 49.9 (2009), p. 095012. URL: <http://stacks.iop.org/0029-5515/49/i=9/a=095012> (cit. on p. 27).
- [55] G.A. Rattá et al. “An advanced disruption predictor for JET tested in a simulated real-time environment”. In: *Nuclear Fusion* 50.2 (2010), p. 025005. URL: <http://stacks.iop.org/0029-5515/50/i=2/a=025005> (cit. on p. 28).
- [56] D. Reiter and M. Baelmans. “The EIRENE and B2-EIRENE Codes”. In: *Fusion Sci. Technol* (2005). URL: http://www.ans.org/pubs/journals/fst/a_698 (cit. on p. 47).
- [57] C Reux. “Etude d’une méthode d’amortissement des disruptions d’un plasma de tokamak”. 2010EPXX0077. PhD thesis. 2010, 1 vol. (222 p.) URL: <http://www.theses.fr/2010EPXX0077/document> (cit. on pp. 47, 71).
- [58] C. Reux and al. “Runaway electron beam generation and mitigation during disruptions at JET-ILW”. In: *submitted to Nuclear Fusion* (2015). URL: <http://www.euro-fusionscipub.org/wp-content/uploads/2015/05/WPJET1PR1408.pdf> (cit. on pp. 35–38).
- [59] C. Reux et al. “Experimental study of disruption mitigation using massive injection of noble gases on Tore Supra”. In: *Nuclear Fusion* 50.9 (Sept. 2010), p. 095006. ISSN: 0029-5515. DOI: [10.1088/0029-5515/50/9/095006](https://doi.org/10.1088/0029-5515/50/9/095006). URL: <http://stacks.iop.org/0029-5515/50/i=9/a=095006?key=crossref.6b22e9d5d6088f0494bd5019d75a97cd> (cit. on p. 34).
- [60] V. Riccardo et al. “JET disruption studies in support of ITER”. In: *Plasma Physics and Controlled Fusion* 52.12 (2010), p. 124018. URL: <http://stacks.iop.org/0741-3335/52/i=12/a=124018> (cit. on p. 39).
- [61] V. Rozhansky et al. “Penetration of supersonic gas jets into a tokamak”. In: *Nuclear Fusion* 46.2 (Feb. 2006), pp. 367–382. ISSN: 0029-5515. DOI: [10.1088/0029-5515/46/2/019](https://doi.org/10.1088/0029-5515/46/2/019). URL: <http://stacks.iop.org/0029-5515/46/i=2/a=019?key=crossref.f8e7fa178c6476ce00e41325cfd34a9b> (cit. on p. 64).

- [62] Y. Saad and M. H. Schultz. “GMRES: A Generalized Minimal Residual Algorithm for Solving Nonsymmetric Linear Systems”. In: *SIAM J. Sci. Stat. Comput.* 7.3 (July 1986), pp. 856–869. ISSN: 0196-5204. DOI: [10.1137/0907058](https://doi.org/10.1137/0907058). URL: <http://dx.doi.org/10.1137/0907058> (cit. on p. 57).
- [63] F. Saint-Laurent et al. “FIRE, a novel concept of massive gas injection for disruption mitigation in ITER: Validation on Tore Supra”. In: *Fusion Engineering and Design* 89.12 (2014), pp. 3022–3038. ISSN: 0920-3796. DOI: <http://dx.doi.org/10.1016/j.fusengdes.2014.09.007>. URL: <http://www.sciencedirect.com/science/article/pii/S0920379614005729> (cit. on p. 30).
- [64] F. C. Schuller. “Disruptions in tokamaks”. In: *Plasma Physics and Controlled Fusion* 37.11A (1995), A135. URL: <http://stacks.iop.org/0741-3335/37/i=11A/a=009> (cit. on pp. 15, 26).
- [65] J.R. Serrano et al. “Analysis of shock capturing methods for chemical species transport in unsteady compressible flow”. In: *Mathematical and Computer Modelling* 57.7–8 (2013). Public Key Services and Infrastructures EUROPKI-2010-Mathematical Modelling in Engineering; Human Behaviour 2011, pp. 1751–1759. ISSN: 0895-7177. DOI: <http://dx.doi.org/10.1016/j.mcm.2011.11.026>. URL: <http://www.sciencedirect.com/science/article/pii/S0895717711007114> (cit. on p. 50).
- [66] T. Sizyuk and A. Hassanein. “Scaling mechanisms of vapour/plasma shielding from laser-produced plasmas to magnetic fusion regimes”. In: *Nuclear Fusion* 54.2 (2014), p. 023004. URL: <http://stacks.iop.org/0029-5515/54/i=2/a=023004> (cit. on p. 18).
- [67] J.A. Snipes, Y. Gribov, and A. Winter. “Physics requirements for the ITER plasma control system”. In: *Fusion Engineering and Design* 85.3–4 (2010). Proceedings of the 7th IAEA Technical Meeting on Control, Data Acquisition, and Remote Participation for Fusion Research, pp. 461–465. ISSN: 0920-3796. DOI: <http://dx.doi.org/10.1016/j.fusengdes.2010.01.019>. URL: <http://www.sciencedirect.com/science/article/pii/S0920379610000207> (cit. on p. 27).
- [68] A. Stahl et al. “Effective Critical Electric Field for Runaway-Electron Generation”. In: *Phys. Rev. Lett.* 114 (11 Mar. 2015), p. 115002. DOI: [10.1103/PhysRevLett.114.115002](https://doi.org/10.1103/PhysRevLett.114.115002). URL: <http://link.aps.org/doi/10.1103/PhysRevLett.114.115002> (cit. on p. 19).
- [69] H. R. Strauss. “Reduced MHD in nearly potential magnetic fields”. In: *Journal of Plasma Physics* 57 (01 Jan. 1997), pp. 83–87. ISSN: 1469-7807. DOI: [10.1017/S0022377896005296](https://doi.org/10.1017/S0022377896005296). URL: http://journals.cambridge.org/article_S0022377896005296 (cit. on p. 52).
- [70] H. P. Summers. “Atomic Data and Analysis Structure”. In: (). URL: <http://adas.ac.uk> (cit. on pp. 46, 55).

- [71] P. Tamain et al. “Thermal interaction of plasma with Gas Puffing”. In: *Journal of Nuclear Materials* 363-365 (June 2007), pp. 844–848. ISSN: 00223115. DOI: [10.1016/j.jnucmat.2007.01.235](https://doi.org/10.1016/j.jnucmat.2007.01.235). URL: <http://linkinghub.elsevier.com/retrieve/pii/S0022311507001651> (cit. on p. 47).
- [72] P. Tamain et al. “Interaction of plasma transport and turbulence on particle fuelling”. In: *Journal of Nuclear Materials* 438, Supplement (2013). Proceedings of the 20th International Conference on Plasma-Surface Interactions in Controlled Fusion Devices, S148–S154. ISSN: 0022-3115. DOI: <http://dx.doi.org/10.1016/j.jnucmat.2013.01.023>. URL: <http://www.sciencedirect.com/science/article/pii/S0022311513000317> (cit. on p. 47).
- [73] A J Thornton et al. “Characterization of disruption mitigation via massive gas injection on MAST”. In: *Plasma Physics and Controlled Fusion* 54.12 (2012), p. 125007. URL: <http://stacks.iop.org/0741-3335/54/i=12/a=125007> (cit. on p. 35).
- [74] F. A. G. Volpe et al. “Advanced techniques for neoclassical tearing mode control in DIII-D”. In: *Physics of Plasmas* 16.10 (2009), p. 102502. ISSN: 1070664X. DOI: [10.1063/1.3232325](https://doi.org/10.1063/1.3232325). URL: <http://scitation.aip.org/content/aip/journal/pop/16/10/10.1063/1.3232325> (cit. on p. 27).
- [75] G. S. Voronov. “A practical fit formula for ionization rate coefficients of atoms and ions by electron impact : $Z= 1-28$ ”. In: *Atomic Data and Nuclear Data Tables* 65.1 (1997), pp. 1–35 (cit. on p. 54).
- [76] P. C. de Vries et al. “The impact of the ITER-like wall at JET on disruptions”. In: *Plasma Physics and Controlled Fusion* 54.12 (Dec. 2012), p. 124032. ISSN: 0741-3335. DOI: [10.1088/0741-3335/54/12/124032](https://doi.org/10.1088/0741-3335/54/12/124032). URL: <http://iopscience.iop.org/0741-3335/54/12/124032> (cit. on pp. 35, 39).
- [77] F. Wagner et al. “Regime of Improved Confinement and High Beta in Neutral-Beam-Heated Divertor Discharges of the ASDEX Tokamak”. In: *Phys. Rev. Lett.* 49 (19 Nov. 1982), pp. 1408–1412. DOI: [10.1103/PhysRevLett.49.1408](https://doi.org/10.1103/PhysRevLett.49.1408). URL: <http://link.aps.org/doi/10.1103/PhysRevLett.49.1408> (cit. on p. 8).
- [78] D. J. Ward and J. A. Wesson. “Impurity influx model of fast tokamak disruptions”. In: *Nuclear Fusion* 32.7 (1992), p. 1117. URL: <http://stacks.iop.org/0029-5515/32/i=7/a=I03> (cit. on p. 97).
- [79] J. Wesson. *Tokamaks*. 2004 (cit. on pp. 16, 45, 55, 80).
- [80] L. Zeng et al. “Experimental Observation of a Magnetic-Turbulence Threshold for Runaway-Electron Generation in the TEXTOR Tokamak”. In: *Physical Review Letters* 110.23 (June 2013), p. 235003. ISSN: 0031-9007. DOI: [10.1103/PhysRevLett.110.235003](https://doi.org/10.1103/PhysRevLett.110.235003). URL: <http://link.aps.org/doi/10.1103/PhysRevLett.110.235003> (cit. on p. 35).
- [81] H. Zohm et al. “Control of NTMs by ECCD on ASDEX Upgrade in view of ITER application”. In: *Plasma Physics and Controlled Fusion* 49.12B (2007), B341. URL: <http://stacks.iop.org/0741-3335/49/i=12B/a=S31> (cit. on p. 27).

Symbols, variables and acronyms

Symbols and variables

- Q : amplification factor
- τ_E : energy confinement time
- \mathbf{B} : magnetic field
- \mathbf{E} : electric field
- ψ : poloidal magnetic flux
- ψ_N or ψ_{norm} : normalized poloidal magnetic flux, label of the flux surfaces
- F_0 : toroidal component of the B multiplied by the major radius, assumed to be constant
- q : safety factor characterizing the helicity of the flux surfaces
- q_{95} : safety factor at the edge (for $\psi_N = 95\%$)
- R_0 : major radius of the tokamak
- a : minor radius of the tokamak
- R : horizontal coordinate along the major radius
- Z : vertical coordinate
- r : coordinate along the minor radius
- θ : angle in the poloidal direction
- φ : angle in the toroidal direction
- m : poloidal mode number (Fourier harmonic)
- n : toroidal mode number (Fourier harmonic)
- t : time

- n : particle density ; n_e : electron density, n_i : ion density
- n_n : neutral density
- ρ : mass density
- T : temperature
- P : scalar pressure
- P_0 : Neutral pressure
- V_0 : Neutral velocity
- $\bar{\Pi}$: pressure tensor
- \mathbf{v} : fluid velocity
- \mathbf{v}_{\parallel} : parallel velocity
- \mathbf{v}^* : diamagnetic velocity
- \mathbf{v}_E : electric drift
- c_s : sound speed
- \mathbf{J} : plasma current
- j : toroidal current
- u : electric potential (scalar)
- \mathbf{A} : vector potential
- W : toroidal vorticity
- τ_{IC} : diamagnetic parameter: inverse of the normalized ion cyclotron frequency
- η : plasma resistivity
- $\mu_{\parallel}, \mu_{\perp}$: plasma parallel and perpendicular viscosity
- $\kappa_{\parallel}, \kappa_{\perp}$: parallel and perpendicular heat diffusivity
- D_{\parallel}, D_{\perp} : parallel and perpendicular particle diffusivity
- S_n : neutral source
- f : probability distribution function
- ν_e^* : electron collisionality
- $\lambda_{e,e}$: electron-electron collision mean free path

- $v_{th,s}$: thermal velocity
- τ_e : electron collision time
- λ_d : Debye length
- m_e, m_i : electron and ion mass
- q_e, q_i : electron and ion charge
- e : Coulomb charge
- μ_0 : magnetic permeability
- ε_0 : vacuum permittivity
- c : light speed
- γ : ratio of the specific heats

Acronyms

- **AUG**: Asdex Upgrade: tokamak located in Garching (Germany)
- **CQ**: Current Quench
- **DEMO**: Prototype for future fusion reactors (generation after ITER)
- **DIII-D**: Doublet III – D : tokamak in San Diego (USA)
- **ELM**: Edge Localized Modes
- **HFS**: High Field Side
- **ITER**: International Thermonuclear Experimental Reactor, also meaning the way in latin: tokamak currently in construction in Cadarache, France
- **JET**: Joint European Torus: European tokamak, located in Culham (UK)
- **JOREK**: reduced MHD code in toroidal geometry, named after the bear in Philip Pullman's *His Dark Materials*
- **LFS**: Low Field Side
- **MGI**: Massive Gas Injection
- **MHD**: Magnetohydrodynamics
- **RMP**: Resonant Magnetic Perturbation
- **SOL**: Scrape-Off Layer
- **TQ**: Thermal Quench

APPENDIX

C Normalization of energy equation for model555

We want the equation in JOEREK variables to look like this :

$$\frac{\partial \tilde{\rho} \tilde{T}}{\partial \tilde{t}} = \dots - \tilde{\xi}_{ion} \tilde{\rho} \tilde{\rho}_n \tilde{S}_i(\tilde{T}) - \tilde{\rho} \tilde{\rho}_n \tilde{L}(\tilde{T}) \quad (8)$$

How should $\tilde{\xi}_{ion}$, \tilde{S}_i and \tilde{L} be defined for it to be the case?

The energy equation (sum for ions and electrons) in SI units writes (Considering $\rho = nm_i$ and $v \approx v_i$):

$$\frac{3}{2} \frac{\partial P}{\partial t} + \frac{3}{2} v \cdot \nabla P + \frac{5}{2} P (\nabla \cdot v) = -\nabla \cdot q + \frac{3}{2} \frac{j \cdot \nabla P_e}{en} + \sum Q \quad (9)$$

With $P = \rho T$, $P = P_e + P_i$, $T = T_e + T_i$ and $\sum Q = Q_{Heating} + Q_{viscosity} + Q_{ionization} + Q_{radiation}$

So, noting $\gamma = \frac{5}{3}$ the adiabaticity index for a monoatomic gas:

$$\frac{\partial P}{\partial t} = -v \cdot \nabla P - \gamma P (\nabla \cdot v) - \frac{2}{3} \nabla \cdot q + \frac{j \cdot \nabla P_e}{en} + \frac{2}{3} \sum Q \quad (10)$$

If we assume that $q = -(\kappa_{\perp} \nabla_{\perp} T + \kappa_{\parallel} \nabla_{\parallel} T)$ and expressing all variables in JOEREK variables, we get:

$$\begin{aligned} \frac{1}{\mu_0 \sqrt{\mu_0 \rho_0}} \frac{\partial \tilde{P}}{\partial \tilde{t}} &= \frac{1}{\mu_0 \sqrt{\mu_0 \rho_0}} (-\tilde{v} \cdot \nabla \tilde{P} - \gamma \tilde{P} (\nabla \cdot \tilde{v})) + \frac{2}{3} \frac{n_0}{\sqrt{\mu_0 \rho_0}} \frac{1}{\mu_0 n_0} \nabla \cdot (\tilde{\kappa}_{\perp} \nabla_{\perp} \tilde{T} + \tilde{\kappa}_{\parallel} \nabla_{\parallel} \tilde{T}) \\ &+ \left(-\frac{1}{R\mu_0}\right) \frac{1}{\mu_0 (1 + \frac{T_i}{T_e}) n_0} \frac{\tilde{j} \cdot \nabla \tilde{P}}{e\tilde{\rho}} + \frac{2}{3} \sum Q \end{aligned}$$

$$\text{knowing that } P_e = \frac{P}{1 + \frac{T_i}{T_e}} = \frac{\tilde{P}}{\mu_0 (1 + \frac{T_i}{T_e})}$$

Let's write the equation as a function of the total isotropic pressure P. It is straightforward for the first two terms on the rhs, and for the term in $j \nabla P$ we get:

$$\mu_0 \sqrt{\mu_0 \rho_0} \frac{1}{R\mu_0} \frac{1}{\mu_0 (1 + \frac{T_i}{T_e}) n_0} \frac{\tilde{j} \cdot \nabla \tilde{P}}{e\tilde{\rho}} \quad (11)$$

With $n_0 = \frac{\rho_0}{m_i}$, we obtain:

$$\frac{\sqrt{\mu_0 \rho_0}}{R\mu_0 \rho_0} \frac{m_i}{1 + \frac{T_i}{T_e}} \frac{\tilde{j} \cdot \nabla \tilde{P}}{e\tilde{\rho}} = \frac{1}{R} \frac{m_i}{e\sqrt{\mu_0 \rho_0} (1 + \frac{T_i}{T_e})} \frac{\tilde{j} \cdot \nabla \tilde{P}}{\tilde{\rho}} \quad (12)$$

knowing that

$$\tau_{IC} = \frac{m_i}{F_0 e \sqrt{\mu_0 \rho_0} (1 + \frac{T_i}{T_e})} \quad (13)$$

we can write:

$$\frac{\partial \tilde{P}}{\partial \tilde{t}} = -\tilde{v} \cdot \nabla \tilde{P} - \gamma \tilde{P} (\nabla \cdot \tilde{v}) + \frac{2}{3} \nabla \cdot (\tilde{\kappa}_\perp \nabla_\perp \tilde{T} + \tilde{\kappa}_\parallel \nabla_\parallel \tilde{T}) - \frac{\tau_{IC} F_0 \tilde{j} \cdot \nabla \tilde{P}}{R \tilde{\rho}} + \sum \tilde{Q} \quad (14)$$

where

$$\sum \tilde{Q} = \frac{2}{3} \mu_0 \sqrt{\mu_0 \rho_0} \sum Q = K \sum Q \quad (15)$$

with $K = \frac{2}{3} \mu_0 \sqrt{\mu_0 \rho_0}$

For the Ohmic heating, we have:

$$Q_{Joule} = \eta_{Spitzer} j^2 = \sqrt{\frac{\mu_0}{\rho_0}} \frac{1}{R^2 \mu_0^2} \tilde{\eta}_{Spitzer} \tilde{j}^2 \quad (16)$$

Thus

$$K Q_{Joule} = \frac{2}{3} \mu_0 \sqrt{\mu_0 \rho_0} \sqrt{\frac{\mu_0}{\rho_0}} \frac{1}{R^2 \mu_0^2} \tilde{\eta}_{Spitzer} \tilde{j}^2 = \frac{2}{3 R^2} \tilde{\eta}_{Spitzer} \tilde{j}^2 \quad (17)$$

And for ionization and radiation we have:

$$Q_{ionization} + Q_{radiation} = -n_e n_n S_i(T_e) E_{ion} - n_e n_n L_{rays}(T_e) - n_e n_i L_{cont}(T_e) \quad (18)$$

where $L_{rays}(T_e)$ is the radiated line power for neutral deuterium and $L_{cont}(T_e)$ is the sum of the radiated power from Bremsstrahlung and recombination radiation for ionized deuterium.

Expressing n_e and n_n as $n_e = \frac{\rho}{m_D} = \frac{\rho_0 \tilde{\rho}}{m_D}$ (we suppose a pure D plasma) and $n_n = \frac{\rho_n}{m_n} = \frac{\rho_{n0} \tilde{\rho}}{m_n}$ we get:

$$K Q_{ionization} = -\frac{2}{3} \mu_0 \sqrt{\mu_0 \rho_0} E_{ion} \frac{\rho}{m_D} \frac{\rho_n}{m_n} S_i(T_e) \quad (19)$$

$$K Q_{ionization} = -\frac{2}{3} \mu_0 \sqrt{\mu_0 \rho_0} \frac{\rho_0 \rho_{n0}}{m_D m_n} E_{ion} \tilde{\rho} \tilde{\rho}_n S_i(T_e) \quad (20)$$

We then impose the definition of $\tilde{S}_i(\tilde{T})$:

$$\tilde{S}_i(\tilde{T}) = \sqrt{\mu_0 \rho_0} n_0 S_i(T_e) \quad (21)$$

So, knowing that $\rho_0 = m_D n_0$:

$$K Q_{ionization} = -\frac{2}{3} \mu_0 \frac{\rho_{n0}}{m_n} E_{ion} \tilde{\rho} \tilde{\rho}_n \tilde{S}_i(\tilde{T}) \quad (22)$$

Finally, if we choose $\rho_{n0} = n_0 m_n$ then:

$$\tilde{\xi}_{ion} = \frac{2}{3}\mu_0 n_0 E_{ion} \quad (23)$$

and

$$KQ_{ionization} = -\tilde{\xi}_{ion}\tilde{\rho}\tilde{\rho}_n\tilde{S}_i(\tilde{T}) \quad (24)$$

Moreover,

$$KQ_{radiation} = -\frac{2}{3}\mu_0\sqrt{\mu_0\rho_0}(n_e n_n L_{rays}(T_e) + n_e n_i L_{cont}(T_e)) \quad (25)$$

$$= -\frac{2}{3}\mu_0\sqrt{\mu_0\rho_0}n_0^2(\tilde{\rho}\tilde{\rho}_n L_{rays}(T_e) + \tilde{\rho}\tilde{\rho} L_{cont}(T_e)) = -\tilde{\rho}\tilde{\rho}_n\tilde{L}_{rays}(\tilde{T}) - \tilde{\rho}\tilde{\rho}\tilde{L}_{cont}(\tilde{T}) \quad (26)$$

So

$$\tilde{L}_{rays/cont}(\tilde{T}) = \frac{2}{3}\mu_0\sqrt{\mu_0\rho_0}n_0^2 L_{rays/cont}(T_e) = \frac{2}{3}\mu_0\sqrt{\mu_0\rho_0}n_0^2 L_{rays/cont}\left(\frac{T}{2}\right) \quad (27)$$

Finally:

$$\sum \tilde{Q} = K(Q_{Joule} + Q_{ioni} + Q_{rad}) = \frac{2}{3R^2}\tilde{\eta}\tilde{j}^2 - \tilde{\xi}_{ion}\tilde{\rho}\tilde{\rho}_n\tilde{S}_i(\tilde{T}) - \tilde{\rho}\tilde{\rho}_n\tilde{L}_{rays}(\tilde{T}) - \tilde{\rho}^2\tilde{L}_{cont}(\tilde{T}) \quad (28)$$

And we obtain (all in JOEREK variables, without tilde for simplicity):

$$\frac{\partial P}{\partial t} = -v \cdot \nabla P - \gamma P (\nabla \cdot v) + \frac{2}{3} \nabla \cdot (\kappa_{\perp} \nabla_{\perp} T + \kappa_{\parallel} \nabla_{\parallel} T) - \frac{\tau_{IC} F_0 j \cdot \nabla P}{R \rho} + \frac{2}{3R^2} \eta_{Spitzer} j^2 \quad (29)$$

$$- \xi_{ion} \rho \rho_n S_i(T) - \rho \rho_n L_{rays}(T) - \rho^2 L_{cont}(T) \quad (30)$$

In the code, this equation is expressed with $P = \rho T$ (in JOEREK units).

Moreover, the factor $\frac{2}{3}$ is included in the value of κ_{\perp} and κ_{\parallel}

So:

$$\frac{\partial \rho T}{\partial t} = -v \cdot \nabla(\rho T) - \gamma(\rho T)(\nabla \cdot v) + \nabla \cdot (\kappa_{\perp} \nabla_{\perp} T + \kappa_{\parallel} \nabla_{\parallel} T) - \frac{\tau_{IC} F_0 j \cdot \nabla(\rho T)}{R \rho} \quad (31)$$

$$+ \frac{2}{3R^2} \eta_{Spitzer} j^2 - \xi_{ion} \rho \rho_n S_i(T) - \rho \rho_n L_{rays}(T) - \rho^2 L_{cont}(T) \quad (32)$$

For example:

$$\tilde{\xi}_{ion} = \frac{2}{3}\mu_0 n_0 E_{ion}[J] = \frac{2}{3}\mu_0 n_0 e E_{ion}[eV] \quad (33)$$

And $\tilde{\xi}_{ion} = n_0 \xi_{ion_{namelist}}$
 So $E_{ion} = 13.6eV$, $\xi_{ion_{namelist}} = 1.810^{-24}$
 Or $\xi_{ion_{namelist}} = 10^{-22}$, $E_{ion} = 750eV$

D Normalization of ion density equation

$$\frac{\partial n_e}{\partial t} = \dots + n_e n_n S_i(T) \quad (34)$$

$$\frac{\partial \rho}{\partial t} = \dots + m_i n_e n_n S_i(T) = \rho n_n S_i(T) = \rho \rho_n \left(\frac{S_i}{m_n} \right) \quad (35)$$

$$\frac{1}{\sqrt{\mu_0 \rho_0}} \frac{\partial \tilde{\rho}}{\partial \tilde{t}} = \dots + \tilde{\rho} \rho_n \left(\frac{S_i}{m_n} \right) \quad (36)$$

$$\frac{\partial \tilde{\rho}}{\partial \tilde{t}} = \dots + \sqrt{\mu_0 \rho_0} \tilde{\rho} \tilde{\rho}_n \rho_{n0} \left(\frac{S_i}{m_n} \right) \quad (37)$$

with $\rho_{n0} = m_n n_0$

$$\frac{\partial \tilde{\rho}}{\partial \tilde{t}} = \dots + \sqrt{\mu_0 \rho_0} n_0 \tilde{\rho} \tilde{\rho}_n S_i = \dots + \tilde{\rho} \tilde{\rho}_n \tilde{S}_i(\tilde{T}) \quad (38)$$

with

$$\tilde{S}_i(\tilde{T}) = \sqrt{\mu_0 \rho_0} n_0 S_i(T) \quad (39)$$

Finally, we get the following equations:

$$\frac{\partial \rho}{\partial t} = -\nabla \cdot (\rho v) + \nabla \cdot (D_{\perp} \nabla_{\perp} \rho + D_{\parallel} \nabla_{\parallel} \rho) + \rho \rho_n S_i(T) - \rho^2 S_r(T) \quad (40)$$

With:

$$v = v_{\parallel} B + v_E + v_i^* = v_{\parallel} B + R^2 \nabla \phi \times \nabla u + \tau_{IC} \frac{R^2}{\rho} (\nabla \phi \times \nabla P) \quad (41)$$

$$\frac{\partial \rho_n}{\partial t} = \nabla \cdot (D_n : \nabla \rho_n) - \rho \rho_n S_i(T) + \rho^2 S_r(T) + S_n \quad (42)$$

E Weak form and JOREK added terms in model555

We have the following energy equation:

$$\frac{\partial P}{\partial t} = \dots + \frac{2}{3R^2} \eta j^2 - \rho \rho_n L(T) - \xi_{ion} \rho \rho_n S_i(T) \quad (43)$$

We get the weak form of this equation by multiplying it by the test function T^* then integrating it on the calculated volume

$$\int T^* \frac{\partial \rho T}{\partial t} dV = \int T^* \left(\frac{2}{3R^2} \eta j^2 - \rho \rho_n L(T) - \xi_{ion} \rho \rho_n S_i(T) \right) dV \quad (44)$$

Let's express these terms according to the Crank-Nicholson scheme:

$$T^* \delta T_0 - \frac{1}{2} \delta t \left(\frac{\partial A}{\partial \xi} \right)_0 \cdot \delta \xi = \delta t A_{0,T} \quad (45)$$

where ξ is the vector composed of the 8 JOEREK variables. Here A is the rhs of the equation (30)

$$A = T^* \frac{2}{3R^2} \eta j^2 - T^* \rho \rho_n L(T) - T^* \xi_{ion} \rho \rho_n S_i(T) \quad (46)$$

We linearize for each variable:

$$\left(\frac{\partial A}{\partial \rho} \right)_0 \delta \rho = -T^* \rho_{n0} L(T_0) \delta \rho - T^* \xi_{ion} \rho_{n0} S_i(T_0) \delta \rho \quad (47)$$

$$\left(\frac{\partial A}{\partial T} \right)_0 \delta T = T^* \frac{2}{3R^2} \left(\frac{\partial \eta}{\partial T} \right)_0 j_0^2 \delta T - T^* \rho_0 \rho_{n0} \left(\frac{\partial L(T)}{\partial T} \right)_0 \delta T - T^* \xi_{ion} \rho_0 \rho_{n0} \left(\frac{\partial S_i(T)}{\partial T} \right)_0 \delta T \quad (48)$$

$$\left(\frac{\partial A}{\partial \rho_n} \right)_0 \delta \rho_n = -T^* \rho_0 L(T_0) \delta \rho_n - T^* \xi_{ion} \rho_0 S_i(T_0) \delta \rho_n \quad (49)$$

$$\left(\frac{\partial A}{\partial j} \right)_0 \delta j = T^* \frac{4}{3R^2} \eta(T_0) j_0 \delta j \quad (50)$$

Consequently, we must add in JOEREK the following terms:

$$rhs(6) = \dots + (T^* \frac{2}{3R^2} \eta(T_0) j_0^2 - T^* \rho_0 \rho_{n0} L(T_0) - T^* \xi_{ion} \rho_0 \rho_{n0} S_i(T_0)) R J_2 \delta t \quad (51)$$

F Density source term

We apply the operator $-\nabla \phi \cdot \nabla \times (R^2 \dots$ to this term (here we neglect the contribution in the diamagnetic velocity). We use the vector identities $\nabla \cdot (a \times b) = b \cdot (\nabla \times a) - a \cdot (\nabla \times b)$ and $a \times (b \times c) = b(a \cdot c) - c(a \cdot b)$. With $v = v_E = R^2 \nabla \phi \times \nabla u$

$$\begin{aligned} -\nabla \phi \cdot \nabla \times (R^2 \mathbf{v} S_\rho) &= -R^2 \mathbf{v} S_\rho (\nabla \times \nabla \phi) + \nabla \cdot (\nabla \phi \times (S_\rho R^2 \mathbf{v})) \\ &= -\nabla \cdot (S_\rho R^2 \mathbf{v} \times \nabla \phi) \\ &= -\nabla \cdot [S_\rho R^4 (\nabla \phi \times \nabla u) \times \nabla \phi] \\ &= -\nabla \cdot [S_\rho R^2 \nabla_\perp u]. \end{aligned} \quad (52)$$

Because $(\nabla\phi \times \nabla u) \times \nabla\phi = \nabla u/R^2 - (\nabla\phi \cdot \nabla u)\nabla\phi = \nabla_{\perp}u$
 In weak form this term yields (integration by parts) :

$$\begin{aligned}
 - \int dV u^* \nabla\phi \cdot \nabla \times (R^2 \mathbf{v} S_{\rho}) &= - \int dV u^* \nabla \cdot [S_{\rho} R^2 \nabla_{\perp} u] \\
 &= + \int dV S_{\rho} R^2 (\nabla_{\perp} u^* \cdot \nabla_{\perp} u) - \int_{\Gamma} u^* (S_{\rho} R^2 \nabla_{\perp} u \cdot \nu^*) d\Gamma \\
 &= + \int dV S_{\rho} R^2 (\nabla_{\perp} u^* \cdot \nabla_{\perp} u)
 \end{aligned} \tag{53}$$

Because the test fonction u^* is set to zero at the JOREK boundary domain.